UNIVERSIDADE FEDERAL DE MINAS GERAIS

PROGRAMA DE PÓS-GRADUAÇÃO EM ENGENHARIA ELÉTRICA

TESE DE DOUTORADO

STUDY OF THE DISCONTINUOUS GALERKIN TIME-DOMAIN METHOD APPLIED TO ELECTROMAGNETIC PROBLEMS INVOLVING DISPERSIVE METERIALS

Tiago Vilela Lima Amorim

7 de maio de 2025

GAPTEM – Grupo de Antenas, Propagação e Teoria Eletromagnética

Departamento de Engenharia Eletrônica
Escola de Engenharia
Universidade Federal de Minas Gerais

Tiago Vilela Lima Amorim

Study of the Discontinuous Galerkin Time-Domain Method Applied to Electromagnetic Problems Involving Dispersive Materials

Final thesis presented to the Graduate Program in Electrical Engineering of the Federal University of Minas Gerais in partial fulfillment of the requirements for the degree of Doctor in Electrical Engineering.

Supervisor: Prof. Dr. Fernando José da Silva Moreira

Co-supervisor: Prof. Dr. Elson José da Silva

Belo Horizonte

2025

Amorim, Tiago Vilela Lima.
A524s Study of The Discontinuous Galerkin Time-Domain Method applied to electromagnetic problems involving dispersive materials [recurso eletrônico] / Tiago Vilela Lima Amorim. - 2025.
1 recurso online (124 f. : il., color.) : pdf.

Orientador: Fernando José da Silva Moreira.
Coorientador: Elson José da Silva.

Tese (doutorado) - Universidade Federal de Minas Gerais, Escola de Engenharia.

Apêndices: f. 110-124

.

Bibliografia: f. 103-109.
Exigências do sistema: Adobe Acrobat Reader.

1. Engenharia elétrica - Teses. 2. Eletromagnetismo - Teses. 3. Galerkin, Métodos de - Teses. 4 Dispersão - Teses. I. Moreira, Fernando José da Silva. II. Silva, Elson José da. III. Universidade Federal de Minas Gerais. Escola de Engenharia. IV. Título.

CDU: 621.3(043)

Ficha catalográfica elaborada pela Bibliotecária Ângela Cristina Silva CRB/6 2361
Biblioteca Prof. Mário Werneck, Escola de Engenharia da UFMG

UNIVERSIDADE FEDERAL DE MINAS GERAIS

"Study of the Discontinuous Galerkin Time-Domain Method Applied to Electromagnetic Problems Involving Dispersive Materials"

Tiago Vilela Lima Amorim

Tese de Doutorado submetida à Banca Examinadora designada pelo Colegiado do Programa de Pós-Graduação em Engenharia Elétrica da Escola de Engenharia da Universidade Federal de Minas Gerais, como requisito para obtenção do grau de Doutor em Engenharia Elétrica.

Aprovada em 07 de maio de 2025.

Por:

Prof. Dr. Fernando José da Silva Moreira
DELT (UFMG) - Orientador

Prof. Dr. Elson José da Silva
DEE (UFMG) - Coorientador

Prof. Dr. Cássio Gonçalves do Rego
DELT (UFMG)

Prof. Dr. Renato Cardoso Mesquita
DEE (UFMG)

Prof. Dr. Guilherme Simon da Rosa
Dept. Engª Eletrônica e de Telecomunicações (UNESP)

Prof. Dr. Fernando Lisboa Teixeira
Dept. Electrical and Computer Engineering (The Ohio State University)

Documento assinado eletronicamente por **Fernando Jose da Silva Moreira**, **Professor do Magistério Superior**, em 07/05/2025, às 16:53, conforme horário oficial de Brasília, com fundamento no art. 5º do Decreto nº 10.543, de 13 de novembro de 2020.

Documento assinado eletronicamente por **Renato Cardoso Mesquita**, **Professor do Magistério Superior**, em 08/05/2025, às 21:12, conforme horário oficial de Brasília, com fundamento no art. 5º do Decreto nº 10.543, de 13 de novembro de 2020.

Documento assinado eletronicamente por **Fernando Lisboa Teixeira**, **Usuário Externo**, em 09/05/2025, às 12:21, conforme horário oficial de Brasília, com fundamento no art. 5º do Decreto nº 10.543, de 13 de novembro de 2020.

Documento assinado eletronicamente por **Guilherme Simon da Rosa**, **Usuário Externo**, em 15/05/2025, às 08:56, conforme horário oficial de Brasília, com fundamento no art. 5º do Decreto nº 10.543, de 13 de novembro de 2020.

Documento assinado eletronicamente por **Elson Jose da Silva**, **Professor do Magistério Superior**, em 20/05/2025, às 15:13, conforme horário oficial de Brasília, com fundamento no art. 5º do Decreto nº 10.543, de 13 de novembro de 2020.

Documento assinado eletronicamente por **Cassio Goncalves do Rego**, **Professor do Magistério Superior**, em 20/05/2025, às 15:26, conforme horário oficial de Brasília, com fundamento no art. 5º do Decreto nº 10.543, de 13 de novembro de 2020.

A autenticidade deste documento pode ser conferida no site https://sei.ufmg.br/sei/controlador_externo.php?acao=documento_conferir&id_orgao_acesso_externo=0, informando o código verificador **4177724** e o código CRC **7C73B0F3**.

Referência: Processo nº 23072.227329/2025-34 SEI nº 4177724

To my future self.

Acknowledgements

I am deeply grateful to my thesis supervisor, Prof. Dr. Fernando José da Silva Moreira, and co-supervisor, Prof. Dr. Elson José da Silva, for their invaluable guidance and support throughout my graduate studies. Their expertise and feedback were crucial in shaping this work. I also want to thank Prof. Dr. Fernando Lisboa Teixeira for his ongoing collaboration, which began during my research at the Ohio State University under the *Programa de Doutorado-sanduíche no Exterior* (PDSE) and has been instrumental in the development of this research.

I am thankful to CAPES for their financial support, without which this research would not have been possible. And lastly, I appreciate the unwavering support of my family, friends, and colleagues during this journey.

“The beauty of electromagnetism lies in its fundamental simplicity, yet the complexity of its consequences.“ — Richard P. Feynman

Resumo

O método de Galerkin Descontínuo no domínio do tempo (DGTD, do inglês *Discontinuous Galerkin Time-Domain*) é uma técnica promissora para resolver problemas eletromagnéticos, particularmente em espalhamento de ondas eletromagnéticas. Esta abordagem discretiza o domínio em elementos não sobrepostos. Dentro de cada elemento, a solução utiliza funções de base polinomiais de alta ordem, contínuas internamente, mas descontínuas nas fronteiras dos elementos. O sistema resultante de equações diferenciais ordinárias semi-discretas é avançado no tempo usando um esquema explícito passo a passo. Uma característica chave deste processo é que cada passo de tempo envolve a resolução de problemas apenas locais dentro de cada elemento, contribuindo significativamente para a eficiência do método. Esta metodologia oferece várias vantagens distintas, incluindo a sua flexibilidade inerente para lidar com geometrias complexas e a sua adaptabilidade direta a malhas não uniformes com refinamento local. A alta precisão é alcançada através do uso de funções de base de alta ordem. Além disso, o método de Galerkin descontínuo é computacionalmente eficiente, exigindo frequentemente menos memória em comparação com outras técnicas de discretização, como os métodos de elementos finitos tradicionais. A eficácia do método DGTD foi validada numa vasta gama de aplicações, abrangendo análise de espalhamento por objetos simples e complexos, estudos de propagação de ondas e modelagem de antenas. A estrutura também se mostrou adaptável, incorporando com sucesso várias condições de contorno essenciais, como camadas perfeitamente casadas (PMLs, do inglês *Perfectly Matched Layers*) e outros tratamentos de contorno absorventes para truncamento do domínio. Esta pesquisa concentra-se especificamente em avançar a aplicação do método de DGTD para a análise de meios complexos, com ênfase principal em materiais dependentes da frequência (dispersivos) e em PMLs. Ambos são incorporados à formulação DGTD por meio do uso de equações diferenciais auxiliares. O objetivo central é ampliar a utilidade do método DGTD em simulações eletromagnéticas que envolvem esses tipos de materiais desafiadores. A principal contribuição desta tese reside na extensão das PMLs uniaxiais convencionais para novas PMLs uniaxiais dispersivas. Nessa formulação avançada, tanto a dispersão do material quanto a dependência em frequência no interior da própria PML são representadas utilizando o modelo de polos e resíduos complexos conjugados. Essa abordagem de modelagem unificada e modular — potencialmente apoiada em técnicas eficientes de extração de parâmetros, como o ajuste vetorial — facilita a integração e permite simulações DGTD mais precisas e robustas de interações de ondas em meios complexos, anisotrópicos e dispersivos.

Palavras-chave: eletromagnetismo; material dispersivo; Galerkin descontínuo.

Abstract

The discontinuous Galerkin time-domain (DGTD) method is a promising technique for solving electromagnetic problems, particularly electromagnetic wave scattering. This approach discretizes the domain into non-overlapping elements. Within each element, the solution uses high-order polynomial basis functions, continuous internally but discontinuous across element boundaries. The resulting system of semi-discrete ordinary differential equations is advanced in time using an explicit step-by-step scheme. A key feature of this process is that each time step involves solving only local problems within each element, contributing significantly to the method's efficiency. This methodology offers several distinct advantages, including its inherent flexibility for handling complex geometries and its straightforward adaptability to non-uniform grids with local refinement. High accuracy is achieved through the use of high-order basis functions. Furthermore, the discontinuous Galerkin method is computationally efficient, often requiring less memory compared to other discretization techniques like traditional finite element methods. The efficacy of the DGTD method has been validated across a wide range of applications, encompassing scattering analysis for both simple and complex objects, wave propagation studies, and antenna modeling. The framework has also proven adaptable, successfully incorporating various essential boundary conditions, such as perfectly matched layers (PMLs) and other absorbing boundary treatments for domain truncation. This research specifically focuses on advancing the application of the DGTD method to the analysis of complex media, with a primary emphasis on frequency-dependent (dispersive) materials and PMLs. Both of these are incorporated into the DGTD formulation through the use of auxiliary differential equations. The main goal is to enhance the DGTD method's utility for electromagnetic simulations involving these challenging material types. The central contribution of this thesis lies in the extension of conventional uniaxial PMLs to novel dispersive uniaxial PMLs. In this advanced formulation, both the material dispersion and the frequency dependence within the PML itself are represented using the complex conjugate pole-residue model. This unified and modular modeling approach, potentially leveraging efficient parameter extraction techniques like vector fitting, facilitates easier integration and enables more accurate and robust DGTD of wave interactions in complex, anisotropic, dispersive environments.

Keywords: electromagnetism; dispersive material; discontinuous Galerkin.

List of Figures

List of Tables

List of Algorithms

List of Abbreviations and Acronyms

ABC Absorbing Boundary Condition 20, 56, 57

ADE Auxiliary Differential Equation 20–23, 60, 63, 65–68, 78, 85, 86, 99, 101, 102

CCPR Complex-Conjugate Pole-Residue 22, 23, 28, 30, 31, 63, 64, 76–78, 85–87, 97, 98

CEM Computational Electrodynamics 19, 20

CFL Courant-Friedrichs-Lewy 46, 49, 86

CFS Complex-Frequency Shifted 21

CPU Central Processing Unit 46

DG Discontinuous Galerkin 60

DGTD Discontinuous Galerkin time-domain 19–24, 32, 33, 46, 47, 49, 51, 56, 60, 63, 64, 76–79, 82, 84–86, 88, 97–102, 110, 112, 113, 115

DOF Degree of Freedom 88

ESDIRK Explicit Singly Diagonally Implicit Runge-Kutta 123

FDTD Finite-Difference Time-Domain 19, 20, 61, 63

FEM Finite-Element Method 19, 20, 63

FVM Finite-Volume Method 19, 20, 112, 115

GPU Graphics Processing Unit 21

IMEX implicit-explicit 21, 23, 24, 85, 86, 88, 89, 91, 94–97, 99–102, 123

ODE Ordinary Differential Equation 55, 85, 86, 88, 92, 99

PDE Partial Differential Equation 55

PEC Perfect Electric Conductor 56, 57, 90, 97, 116–118, 120

PMC Perfect Magnetic Conductor 56, 57

PML Perfect Matched Layer 10, 20–24, 56–58, 60, 63, 65–68, 71, 72, 74, 76–78, 80–82, 85–88, 97, 99–102

RHS Right-Hand Side 68

RK Runge-Kutta 23, 47–49, 85, 86, 88, 92, 123

SBC Scattering Boundary Condition 63

SFR Scattered-Field Region 61, 62, 81

TE Transverse Electric 116, 120

TF/SF Total-Field/Scattered-Field 60–62, 64, 75, 81, 99

TFR Total-Field Region 61, 62

TM Transverse Magnetic 91, 97, 116, 120

Contents

CHAPTER 1

Introduction

1.1 Introduction

The unyielding march of technological progress necessitates ever more sophisticated computational tools capable of unraveling the intricate interactions between electromagnetic waves and the physical world. Computational Electrodynamics (CEM) stands at the forefront of this pursuit, providing indispensable insights that drive innovation across a diverse spectrum of fields, from antenna design and radar systems to medical imaging, nanophotonics, high-speed electronics, and beyond [1, 2, 3, 4]. As operating frequencies climb ever higher and geometrical complexities escalate, conventional numerical methods frequently encounter limitations in their ability to effectively balance the competing demands of accuracy, computational efficiency, and geometric flexibility [5]. This inherent challenge has stimulated the exploration of alternative methodologies, resulting in the development of the Discontinuous Galerkin time-domain (DGTD) method as a powerful and exceptionally versatile approach for simulating electromagnetic wave propagation phenomena [6].

The DGTD method distinguishes itself through a compelling synthesis of three prominent numerical techniques: the Finite-Difference Time-Domain (FDTD) method [5], the Finite-Volume Method (FVM) [7], and the Finite-Element Method (FEM) [8]. By inheriting and amplifying the strengths of each, DGTD offers a unique set of advantages. From the FVM, it borrows the concept of numerical fluxes across element interfaces. This crucial feature enables the accurate representation of discontinuities in electromagnetic fields, ensuring the conservation of physical quantities such as energy and momentum. This capability proves particularly valuable when simulating wave propagation across material interfaces, handling abrupt changes in electromagnetic properties, and modeling complex geometrical features. Simultaneously, it embraces the FEM's ability to utilize high-order basis functions within each element, enabling accurate

spatial discretization over unstructured meshes. This allows for a highly accurate representation of the spatial variation of electromagnetic fields, enabling the attainment of high-fidelity solutions even with relatively coarse meshes. From the FDTD method, DGTD inherits its explicit time-marching scheme, allowing for efficient time-domain simulations without the need for global matrix inversion and maintaining temporal locality. This synergistic combination of FVM, FEM, and FDTD principles not only reduces computational burden but also provides geometric flexibility, numerical stability, and scalability. As a result, the DGTD method emerges as an exceptionally promising candidate for simulating wave propagation in complex structures and heterogeneous media, pushing the boundaries of CEM.

Realistic electromagnetic simulations often involve two major challenges: accurately representing materials whose properties vary with frequency, and effectively truncating unbounded spatial domains without introducing reflections. Addressing both dispersion and domain truncation is essential for capturing wave–matter interactions in advanced applications. These challenges motivate the development of efficient time-domain methods that support frequency-dependent materials and robust absorbing boundaries, setting the stage for the discussions that follow.

One of the central challenges is *dispersion*—the phenomenon where material properties like permittivity and permeability vary with frequency. Dispersion plays a crucial role in determining how electromagnetic waves interact with matter and is fundamental in a wide range of applications, from metamaterials and photonic crystals to plasmonic structures and even biological tissues [9, 10, 11, 12]. Accurately modeling this frequency dependence within numerical simulations is essential for realistic predictions and insightful analyses.

In time-domain methods such as the FDTD method, modeling dispersive materials poses particular difficulties. The constitutive relations, which link electric and magnetic fields to material properties, become convolutions in the time domain due to frequency dependence. Direct evaluation of these convolutions is computationally expensive. To overcome this, several techniques have been developed within the FDTD framework, including the recursive convolution method, Z-transform techniques, and the Auxiliary Differential Equation (ADE) method [13, 14, 15], all aiming to make these convolutions more tractable for numerical implementation.

Another key aspect of realistic simulations is the treatment of open-domain problems, where waves should exit the computational domain without artificial reflections. Absorbing Boundary Conditions (ABCs) are essential tools for this purpose. Early approaches, such as the Silver–Müller boundary condition, impose approximate radiation conditions but often perform poorly for oblique or evanescent waves. A more effective solution is the PML [16], which surrounds the computational domain with an artificial absorbing layer that attenuates outgoing waves across a wide range of incidence angles and frequencies. Despite its robustness, ongoing research seeks to improve PML performance, especially for evanescent and grazing-incidence waves [5].

Within this context, the DGTD method has emerged as a powerful and versatile framework for simulating open-domain electromagnetic problems. It naturally accommodates complex geometries and is well suited for time-domain simulations involving dispersive materials. In particular, it supports the ADE approach for modeling frequency-dependent media and has been shown to effectively integrate uniaxial PML formulations [17].

Furthermore, the versatility of DGTD extends beyond its ability to handle dispersive materials. The method readily accommodates non-conformal meshes and curved elements, allowing for accurate representation of intricate geometrical details and complex material interfaces [6]. Moreover, DGTD's inherent localized nature makes it exceptionally well-suited for parallel computing, enabling the efficient simulation of large-scale problems by distributing the computational load across multiple processors or Graphics Processing Unit (GPU)'s [18]. Advanced techniques such as hp-adaptivity, which dynamically adjusts the polynomial order (p) and element size (h) based on the local solution characteristics, further enhance the efficiency and accuracy of DGTD simulations [19]. Local time stepping schemes, which permit different time steps to be used in different regions of the computational domain, offer additional computational savings by adapting to local variations in mesh resolution and material properties [20]. In addition, the use of implicit-explicit (IMEX) time integration schemes provides a robust and efficient strategy for handling the stiff source terms that often arise in the modeling of complex dispersive or multiscale phenomena, by treating non-stiff terms explicitly while addressing stiff components implicitly, thus ensuring stability without compromising performance [21].

1.2 Motivation

Accurate and efficient simulation of electromagnetic wave propagation is essential for a wide range of applications, including antenna design, radar systems, medical imaging, and nanophotonics. As devices become more sophisticated and operate at higher frequencies, numerical methods must be capable of handling complex geometries, frequency-dependent material properties, and unbounded spatial domains. Among existing approaches, the DGTD method offers a compelling combination of geometric flexibility, high-order accuracy, and parallel scalability. Despite these advantages, accurately modeling wave interactions with dispersive materials in open domains continues to present challenges within the DGTD framework.

Incorporating dispersive PMLs often relies on the Complex-Frequency Shifted (CFS) formulation, which requires modifications to numerical fluxes at element interfaces. While this strategy improves absorption, it introduces implementation complexity and may hinder computational performance, particularly in high-order settings. Additionally, the seamless integration of general dispersive materials into a modular and efficient DGTD formulation remains an open problem.

To overcome these limitations, a modular DGTD framework is developed that supports general dispersive materials directly terminated by a tailored uniaxial PML. Building on the formulation introduced in [22], the proposed approach maintains a fully local structure, avoiding any modification to numerical fluxes. This design simplifies implementation and enhances parallel efficiency, especially in wideband scenarios [23, 24, 25].

The method incorporates the Complex-Conjugate Pole-Residue (CCPR) model [26] to represent general dispersion, enabling direct use of materials characterized via vector fitting techniques [27]. The ADE formulation provides a modular mechanism for representing both dispersive materials and the uniaxial PML. This structure supports selective activation of extensions only in relevant regions, optimizing resource utilization. The uniaxial PML [16] is adapted to match the surrounding dispersive media [28], ensuring efficient absorption of outgoing waves.

1.3 Objectives and Contributions

The primary objective of this work is to develop a modular and efficient DGTD framework capable of accurately modeling electromagnetic wave propagation in general dispersive media bounded by a tailored PML. This formulation aims to address key limitations of existing approaches by enabling direct truncation of dispersive materials without requiring additional free space or complex flux modifications.

The main contributions of this work are summarized as follows:

- A generalized DGTD formulation is presented that supports a broad class of dielectric dispersive materials modeled using the CCPR approach. This enables direct integration of frequency-dependent materials characterized via vector fitting.
- A dispersive uniaxial PML is incorporated in a modular fashion through the ADE method, allowing seamless termination of dispersive regions without modifying numerical fluxes at element interfaces.
- The proposed method maintains a fully local structure. This design choice enhances computational efficiency and scalability, particularly in high-order and wideband simulations.
- A unified framework is established in which both material dispersion and absorbing boundaries are treated through region-specific auxiliary equations. This plug-and-play architecture enables selective activation of model components, optimizing memory usage and processing costs.
- Numerical results are provided for canonical two-dimensional and three-dimensional scattering problems to validate the proposed approach. Comparisons with analytical solutions demonstrate the accuracy and effectiveness of the formulation.

- The outcomes of this research have been disseminated through peer-reviewed journals [29, 30], as well as presented at national [31] and international [32] conferences.

1.4 Text Structure

The notation and mathematical framework adopted throughout this thesis are introduced in Chapter 2, which outlines Maxwell's equations as they are applied in the subsequent developments. Rather than focusing on detailed derivations, this chapter emphasizes the formal definition and use of these equations within the context of the work.

Building on this foundation, Chapter 3 presents the core concepts of the DGTD method. It introduces the underlying theoretical principles, including element construction, spatial discretization, and time integration strategies, forming the basis for the numerical approach adopted.

The application of DGTD to computational electromagnetics is detailed in Chapter 4, which bridges the previous chapters and illustrates the practical implementation of the method. This includes the treatment of sources, enforcement of boundary conditions, and other relevant modeling aspects.

The extension of DGTD to handle general dielectric dispersive materials, modeled using the CCPR approach, is presented in Chapter 5. This chapter introduces a key contribution: a modular formulation incorporating dispersive PMLs via the ADE framework, allowing direct truncation of dispersive domains without extra free space. The advantages of this unified, plug-and-play approach for handling material dispersion and domain truncation are highlighted, and the implementation is validated against analytical solutions for canonical problems.

Further advancements are presented in Chapter 6, where the modular DGTD framework is extended to simulate doubly dispersive media (exhibiting both electric and magnetic dispersion) and to incorporate curvilinear elements for accurate geometric modeling. The chapter details the extension of the uniaxial PML to handle these general doubly dispersive materials, thereby enhancing the method's capability to tackle a wider range of complex electromagnetic problems involving intricate materials and shapes. The robustness of the extended algorithm is demonstrated through validation examples.

Recognizing the computational challenges posed by numerical stiffness, particularly in simulations involving the auxiliary equations for dispersive media and PMLs, Chapter 7 explores advanced time integration strategies. This chapter details the application of IMEX Runge-Kutta (RK) schemes to the semi-discrete DGTD system derived in previous chapters. By treating the stiff components implicitly and non-stiff components explicitly, this approach aims to achieve stable and efficient simulations for doubly dispersive problems, overcoming the strict time-step limitations of purely explicit methods.

Finally, Chapter 8 summarizes the main contributions of this thesis, reviews the key

findings regarding the developed modular DGTD framework for dispersive and doubly dispersive media with associated PMLs and IMEX schemes, and discusses potential avenues for future research.

CHAPTER 2

Electromagnetic Foundation

The present chapter establishes the fundamental electromagnetic field concepts that underlie this study. Additionally, it presents the notation, definitions, and nomenclature employed throughout this thesis.

2.1 Notation and Assumptions

In this thesis, variables with three components in a coordinate system are denoted using bold fonts in equations, while scalar variables are represented using non-bold fonts. For example, the position in the Cartesian coordinate system is denoted by $\boldsymbol{x}$, whereas time is represented by t. The vector fields are denoted using uppercase and mathematical font as $\boldsymbol{\mathcal{E}}$ for time-domain relationships and only uppercase as $\boldsymbol{E}$ for frequency-domain relationships. Furthermore, a general vector with an arbitrary number of elements is indicated using variables with vector notation as $\vec{v}$, while matrices are represented by non-bold uppercase letters such as A. Unless otherwise specified, it is assumed that all vectors are in column format. A comprehensive overview of the notation employed can be found in Table 1.

2.2 Maxwell's Equations

Considering an open surface S bounded by a closed contour C. The first two Maxwell's equations can be written as

$$\oint_C \boldsymbol{\mathcal{E}}(\boldsymbol{x},t)\cdot d\boldsymbol{l} = -\frac{d}{dt}\iint_S \boldsymbol{\mathcal{B}}(\boldsymbol{x},t)\cdot d\boldsymbol{s}, \tag{2.1}$$

$$\oint_C \boldsymbol{\mathcal{H}}(\boldsymbol{x},t)\cdot d\boldsymbol{l} = \frac{d}{dt}\oiint_S \boldsymbol{\mathcal{D}}(\boldsymbol{x},t)\cdot d\boldsymbol{s} + \iint_S \boldsymbol{\mathcal{J}}_{\text{total}}(\boldsymbol{x},t)\cdot d\boldsymbol{s}, \tag{2.2}$$

Table 1 – Variable notation in the thesis

Variable Type	Notation	Example
Scalar variable	t	5 seconds
Coordinate point	$\boldsymbol{x}$	(x_0, y_0, z_0)
Coordinate vector	$\boldsymbol{v}$	$[v_x, v_y, v_z]^\intercal$
Coordinate vector (unit length)	$\hat{\boldsymbol{v}}$	$\|[v_x, v_y, v_z]^\intercal\| = 1$
Time-domain vector field	$\boldsymbol{\mathcal{E}}$	$[\mathcal{E}_x(t), \mathcal{E}_y(t), \mathcal{E}_z(t)]^\intercal$
Frequency-domain vector field	$\boldsymbol{E}$	$[E_x(\omega), E_y(\omega), E_z(\omega)]^\intercal$
Arbitrary length vector	$\vec{v}$	$\vec{v} = [v_1, v_2, \ldots, v_n]^\intercal$
Coordinate vector of arbitrary length vectors	$\vec{\boldsymbol{v}}$	$\vec{\boldsymbol{v}} = [\vec{v}_x, \vec{v}_y, \vec{v}_z]^\intercal$
Matrix (non-bold uppercase)	A	$\begin{bmatrix} a_{11} & a_{12} \\ a_{21} & a_{22} \end{bmatrix}$
Rank-2 Tensor (e.g., permittivity)	$\bar{\bar{\epsilon}}$	$\begin{bmatrix} \epsilon_{xx} & \epsilon_{xy} & \epsilon_{xz} \\ \epsilon_{yx} & \epsilon_{yy} & \epsilon_{yz} \\ \epsilon_{zx} & \epsilon_{zy} & \epsilon_{zz} \end{bmatrix}$

and considering a volume V bounded by a closed surface S, the remaining two equations can be written as

$$\oiint_S \boldsymbol{\mathcal{B}}(\boldsymbol{x}, t) \cdot d\boldsymbol{s} = 0, \tag{2.3}$$

$$\oiint_S \boldsymbol{\mathcal{D}}(\boldsymbol{x}, t) \cdot d\boldsymbol{s} = \iiint_V q_v(\boldsymbol{x}, t) dv, \tag{2.4}$$

where $\boldsymbol{\mathcal{E}}$ is the electric intensity (volt per meter), $\boldsymbol{\mathcal{B}}$ is the magnetic flux density (weber per square meter), $\boldsymbol{\mathcal{H}}$ is the magnetic intensity (ampere per meter), $\boldsymbol{\mathcal{D}}$ is the electric flux density (coulomb per square meter), $\boldsymbol{\mathcal{J}}_{\text{total}}$ is the electric current density (ampere per square meter), and q_v is the electric charge density (coulomb per cubic meter) [33]. The position $\boldsymbol{x}$ and time variable t indicate that the associated fields may have spatial and temporal dependencies.

If the fields are assumed to be well-behaved, continuous and with continuous derivatives, the above quantities cah also be expressed as [33]

$$\nabla \times \boldsymbol{\mathcal{E}}(\boldsymbol{x}, t) = -\frac{\partial}{\partial t} \boldsymbol{\mathcal{B}}(\boldsymbol{x}, t), \tag{2.5}$$

$$\nabla \times \boldsymbol{\mathcal{H}}(\boldsymbol{x}, t) = \frac{\partial}{\partial t} \boldsymbol{\mathcal{D}}(\boldsymbol{x}, t) + \boldsymbol{\mathcal{J}}_{\text{total}}(\boldsymbol{x}, t), \tag{2.6}$$

$$\nabla \cdot \boldsymbol{\mathcal{B}}(\boldsymbol{x}, t) = 0, \tag{2.7}$$

$$\nabla \cdot \boldsymbol{\mathcal{D}}(\boldsymbol{x}, t) = q_v(\boldsymbol{x}, t). \tag{2.8}$$

2.3 Constitutive Relations

The constitutive relations are forms of expressing the quantities $\boldsymbol{\mathcal{B}}$, $\boldsymbol{\mathcal{D}}$ and $\boldsymbol{\mathcal{J}}$ as functions of the electromagnetic fields $\boldsymbol{\mathcal{E}}$ and $\boldsymbol{\mathcal{H}}$. Considering vacuum, these can be written as

$$\boldsymbol{\mathcal{D}}(\boldsymbol{x},t) = \epsilon_0\, \boldsymbol{\mathcal{E}}(\boldsymbol{x},t), \tag{2.9}$$

$$\boldsymbol{\mathcal{B}}(\boldsymbol{x},t) = \mu_0\, \boldsymbol{\mathcal{H}}(\boldsymbol{x},t), \tag{2.10}$$

$$\boldsymbol{\mathcal{J}}(\boldsymbol{x},t) = 0, \tag{2.11}$$

where ϵ_0 is the permittivity of free space (farad per meter), and μ_0 is the permeability of free space (henry per meter). The numerical values of these quantities are [33]

$$\epsilon_0 \approx 8.854 \times 10^{-12}\ \text{F/m} \approx \frac{1}{36\pi} \times 10^{-9}\ \text{F/m}, \tag{2.12}$$

$$\mu_0 = 4\pi \times 10^{-7}\ \text{H/m}. \tag{2.13}$$

In a simple medium, the constitutive relations may become simple proportionalities. Thus

$$\boldsymbol{\mathcal{D}}(\boldsymbol{x},t) = \epsilon\, \boldsymbol{\mathcal{E}}(\boldsymbol{x},t), \tag{2.14}$$

$$\boldsymbol{\mathcal{B}}(\boldsymbol{x},t) = \mu\, \boldsymbol{\mathcal{H}}(\boldsymbol{x},t), \tag{2.15}$$

$$\boldsymbol{\mathcal{J}}(\boldsymbol{x},t) = \sigma\, \boldsymbol{\mathcal{E}}(\boldsymbol{x},t) \tag{2.16}$$

where, as in the vacuum case, ϵ is the permittivity of the medium, μ is the permeability of the medium and σ is the conductivity of the medium. These parameters can be expressed as proportionalities of the vacuum permittivity and permeability, denoted by $\epsilon_r\epsilon_0$ and $\mu_r\mu_0$, respectively, where the subscript r indicates the relative dimensionless variable.

In an anisotropic medium, Equations (2.14) and (2.15) become

$$\boldsymbol{\mathcal{D}}(\boldsymbol{x},t) = \bar{\bar{\epsilon}}\, \boldsymbol{\mathcal{E}}(\boldsymbol{x},t), \tag{2.17}$$

$$\boldsymbol{\mathcal{B}}(\boldsymbol{x},t) = \bar{\bar{\mu}}\, \boldsymbol{\mathcal{H}}(\boldsymbol{x},t), \tag{2.18}$$

where $\bar{\bar{\epsilon}}$ and $\bar{\bar{\mu}}$ are the permittivity and permeability tensors, respectively.

2.4 Dispersive Materials

To account for electric and magnetic dipoles induced in the media, considering isotropic media for simplicity without loss of generality, Equations (2.14) and (2.15) can be extended to

$$\boldsymbol{\mathcal{D}}(\boldsymbol{x},t) = \epsilon_\infty\epsilon_0\, \boldsymbol{\mathcal{E}}(\boldsymbol{x},t) + \boldsymbol{\mathcal{P}}(\boldsymbol{x},t), \tag{2.19}$$

$$\boldsymbol{\mathcal{B}}(\boldsymbol{x},t) = \mu_\infty \mu_0 \, \boldsymbol{\mathcal{H}}(\boldsymbol{x},t) + \mu_0 \, \boldsymbol{\mathcal{M}}(\boldsymbol{x},t), \tag{2.20}$$

where $\boldsymbol{\mathcal{P}}$ is the polarization vector (coulomb per square meter) and $\boldsymbol{\mathcal{M}}$ is the magnetization vector (ampere per meter). The subscript ∞ indicates the relative quantity at high frequencies.

In the frequency domain considering a linear and isotropic medium, the electric and magnetic fields can be associated with the polarization vectors through the utilization of either an electric susceptibility χ_e or a magnetic susceptibility χ_m [34]

$$\boldsymbol{P}(\boldsymbol{x},\omega) = \epsilon_0 \chi_e(\omega) \boldsymbol{E}(\boldsymbol{x},\omega), \tag{2.21}$$

$$\boldsymbol{M}(\boldsymbol{x},\omega) = \chi_m(\omega) \boldsymbol{H}(\boldsymbol{x},\omega). \tag{2.22}$$

Hence, the constitutive relations Equations (2.14) and (2.15) can be reformulated in the frequency domain as follows

$$\boldsymbol{D}(\boldsymbol{x},\omega) = \epsilon_\infty \epsilon_0 \boldsymbol{E}(\boldsymbol{x},\omega) + \epsilon_0 \chi_e(\omega) \boldsymbol{E}(\boldsymbol{x},\omega), \tag{2.23}$$

$$\boldsymbol{B}(\boldsymbol{x},\omega) = \mu_\infty \mu_0 \boldsymbol{H}(\boldsymbol{x},\omega) + \mu_0 \chi_m(\omega) \boldsymbol{H}(\boldsymbol{x},\omega). \tag{2.24}$$

Considering that the permittivity can be defined as

$$\epsilon(\omega) = \epsilon_0 \epsilon_r(\omega) = \epsilon_0 \left[\epsilon_\infty + \chi_e(\omega)\right], \tag{2.25}$$

where ϵ_r is the relative permittivity. Assuming that the fields are considered to be zero at $t = 0$, the inverse Fourier transform of Equation (2.23) yields

$$\boldsymbol{\mathcal{D}}(\boldsymbol{x},t) = \epsilon_\infty \epsilon_0 \boldsymbol{\mathcal{E}}(\boldsymbol{x},t) + \epsilon_0 \int_0^t \chi_e(t-\tau) \boldsymbol{\mathcal{E}}(\boldsymbol{x},\tau) d\tau, \tag{2.26}$$

where

$$\chi_e(t) = \frac{1}{2\pi} \int_{-\infty}^{\infty} \chi_e(\omega) e^{j\omega t} d\omega. \tag{2.27}$$

The same analysis can be performed for the magnetic field considering

$$\mu(\omega) = \mu_0 \mu_r(\omega) = \mu_0 \left[\mu_\infty + \chi_m(\omega)\right], \tag{2.28}$$

leading to

$$\boldsymbol{\mathcal{B}}(\boldsymbol{x},t) = \mu_\infty \mu_0 \boldsymbol{\mathcal{H}}(\boldsymbol{x},t) + \mu_0 \int_0^t \chi_m(t-\tau) \boldsymbol{\mathcal{H}}(\boldsymbol{x},\tau) d\tau, \tag{2.29}$$

where

$$\chi_m(t) = \frac{1}{2\pi} \int_{-\infty}^{\infty} \chi_m(\omega) e^{j\omega t} d\omega. \tag{2.30}$$

Dispersion in dielectric materials is commonly modeled using the electric parameters ϵ_∞ and χ_e. Linear and isotropic dielectric dispersion models, including the Debye, Lorentz, and Drude media are among the most important classes of such models [5]. In the following subsections, these models will be discussed as well as a more general model known as CCPR. While not explicitly mentioned, it should be noted that doubly dispersive materials can also be modeled by considering magnetic quantities such as μ_∞ and χ_m.

2.4.1 Debye Media

Debye media exhibit a frequency-domain complex-valued susceptibility function denoted by $\chi_e(\omega)$. This function is characterized by one or more real poles that are located at distinct frequencies. Specifically, for a Debye medium with a single pole, the susceptibility function can be expressed as [35]

$$\chi_e(\omega) = \frac{\epsilon_s - \epsilon_\infty}{1 + j\omega\tau} = \frac{\Delta\epsilon}{1 + j\omega\tau}, \tag{2.31}$$

where ϵ_s is the static, also known as zero-frequency, relative permittivity, ϵ_∞ is the relative permittivity at infinite frequency, $\Delta\epsilon$ is the change in relative permittivity due to the Debye pole, and τ is the pole relaxation time.

For a Debye medium with P poles, the relative permittivity can be expressed as

$$\epsilon_r(\omega) = \epsilon_\infty + \sum_{p=1}^{P} \frac{\Delta\epsilon_p}{1 + j\omega\tau_p}, \tag{2.32}$$

where $\Delta\epsilon_p$ and τ_p are parameters that describe the frequency-dependent permittivity behavior of each Debye pole.

2.4.2 Lorentz Media

The Lorentz medium is defined by a susceptibility function $\chi_e(\omega)$ in the frequency domain, which is a complex-valued function. This function is characterized by having one or more pairs of complex-conjugate poles. In the case of a Lorentz medium with a single pole pair, the susceptibility function is given by [36]

$$\chi_e(\omega) = \frac{\Delta\epsilon\,\omega_l^2}{\omega_l^2 + 2j\omega\delta_l - \omega^2}, \tag{2.33}$$

where $\Delta\epsilon = \epsilon_s - \epsilon_\infty$ is the change in relative permittivity due to the Lorentz pole pair, ω_l is the frequency of the Lorentz pole pair (the undamped resonant frequency of the medium), and δ_l is the damping coefficient.

For a Lorentz medium with P poles, the relative permittivity can be expressed as

$$\epsilon_r(\omega) = \epsilon_\infty + \sum_{p=1}^{P} \frac{\Delta\epsilon_p\omega_p^2}{\omega_p^2 + 2j\omega\delta_p - \omega^2}, \tag{2.34}$$

where $\Delta\epsilon_p$, ω_p and δ_p are parameters that describe the frequency-dependent permittivity behavior of each Lorentz pole.

2.4.3 Drude Media

In the study of electromagnetic wave interactions with metals at optical wavelengths, it is often necessary to adopt a dispersive formulation to accurately capture the underlying physics

of internal electron motion. At the macroscopic scale, the Drude model has emerged as a popular choice for such modeling purposes. Its complex-valued susceptibility function $\chi_e(\omega)$ considering a single pole can be expressed as [36]

$$\chi_e(\omega) = -\frac{\omega_d^2}{\omega^2 + j\omega\gamma_d}, \tag{2.35}$$

where ω_d is the Drude pole frequency and γ_d is the inverse of the relaxation time.

For a Drude medium having P poles, the extended relative permittivity is

$$\epsilon_r(\omega) = \epsilon_\infty - \sum_{p=1}^{P} \frac{\omega_p^2}{\omega^2 + j\omega\gamma_p}, \tag{2.36}$$

where ω_p and γ_p are parameters that describe the frequency-dependent permittivity behavior of each Drude pole.

2.4.4 Complex-Conjugate Pole-Residue Model for General Media

One effective method for developing a more comprehensive and accurate model for dispersive media is through the use of the CCPR model. This model provides a flexible approach for representing the frequency-dependent permittivity of a wide variety of materials. The CCPR model achieves this by separating the permittivity into two components, expressed as

$$\epsilon(\omega) = \epsilon_0\epsilon_\infty + \epsilon_0\chi_e(\omega), \tag{2.37}$$

where the first term $\epsilon_0\epsilon_\infty$ represents the high-frequency permittivity of the medium, and the second term, $\epsilon_0\chi_e(\omega)$, accounts for the dispersive effects. The frequency-dependent susceptibility $\chi_e(\omega)$ is further expressed as

$$\chi_e(\omega) = \sum_{r=1}^{R} \left(\frac{c_r}{j\omega + \alpha_r} + \frac{c_r^*}{j\omega + \alpha_r^*} \right), \tag{2.38}$$

with R representing the number of conjugate poles used in the model. The parameters c_r and α_r correspond to each individual pole and residue pair, respectively. These parameters capture the resonant and damping behaviors that characterize the dispersive nature of the material.

The CCPR model is particularly versatile, as it can represent several well-known dispersive media models as specific cases. For example, a purely conductive medium can be modeled using a single pole-residue pair, where the parameters are chosen such that $\alpha_0 = 0$ and $c_0 = \sigma/(2\epsilon_0)$, with σ representing the material's conductivity. Similarly, the poles of Debye's model, which describes relaxation processes in dielectrics, are obtained with $c_r = \Delta\epsilon_r/2\tau_r$ and $\alpha_r = 1/\tau_r$, where $\Delta\epsilon_r$ and τ_r are the material's permittivity change and relaxation time, respectively. For Lorentz media, which describe resonance phenomena, the poles can be expressed as $c_r = j\Delta\epsilon_r\omega_r^2/(2\sqrt{\omega_r^2 - \delta_r^2})$ and $\alpha_r = -\delta_r - j\sqrt{\omega_r^2 - \delta_r^2}$, where ω_r is the resonant frequency

and δ_r is the damping factor [17]. Table 2 provides a summary of the coefficients for different well-known dispersive media models, showing how they are parameterized in the CCPR model.

Table 2 – Summary of coefficients for different dispersive media models

Media Model	**Parameter**	**Coefficient** c_r	**Pole** α_r
Conductive Media	σ: conductivity	$\frac{\sigma}{2\epsilon_0}$	0
Debye Model	$\Delta\epsilon_r$: permittivity change, τ_r: relaxation time	$\frac{\Delta\epsilon_r}{2\tau_r}$	$\frac{1}{\tau_r}$
Lorentz Media	$\Delta\epsilon_r$: permittivity change, ω_r: resonant frequency, δ_r: damping factor	$j\frac{\Delta\epsilon_r\omega_r^2}{2\sqrt{\omega_r^2-\delta_r^2}}$	$-\delta_r - j\sqrt{\omega_r^2-\delta_r^2}$

An important advantage of the CCPR model is its ability to fit real material data. By employing vector-fitting algorithms, one can determine the values of c_r and α_r directly from experimentally measured permittivity data for a specific material. This fitting process enables the CCPR model to capture the intricate dispersive behavior of complex materials with high accuracy. It should be noted that the optimal number of pole-residue pairs, R, required for an accurate approximation depends on the characteristics of the material's permittivity function $\epsilon(\omega)$. The more complex the material's dispersive behavior, the higher the number of poles R that may be needed to achieve a satisfactory representation.

CHAPTER 3

Mathematical Foundation

This chapter presents a comprehensive discussion of the classical framework of the nodal DGTD [6]. The discussion encompasses both weak and strong forms of the conservation law, employing the Galerkin approach. Moreover, it elucidates the procedure for constructing nodal high-order elements in one, two, and three dimensions. Furthermore, it illustrates how the resulting semi-discrete equations can be integrated over time.

3.1 Notation and Assumptions

The present formulation focuses on problems posed on the physical domain Ω, with a boundary represented by $\partial\Omega$. It is assumed that this domain can be effectively approximated by a computational domain Ω_h, comprising K non-overlapping, geometry-conforming elements represented as Ω_h^k. It should be noted that while the shape of these elements may vary, the analysis presented herein solely examines d-dimensional simplices.

Henceforth, the following definitions shall be employed throughout this thesis. In these definitions, u is the unknown solution function to be approximated, and v is a test function used in the variational formulation of the problem.

$$(u,v)_{\Omega_h^k} = \int_{\Omega_h^k} uv \, d\Omega, \quad \|u\|^2_{\Omega_h^k} = (u,u)_{\Omega_h^k},$$

as well as the global broken inner product and norm

$$(u,v)_{\Omega_h} = \sum_{k=1}^{K} (u,v)_{\Omega_h^k}, \quad \|u\|^2_{\Omega_h} = (u,u)_{\Omega_h},$$

where Ω_h refers to Ω being approximated by the union of Ω_h^k, that is

$$\Omega \approx \Omega_h = \bigcup_{k=1}^{K} \Omega_h^k. \tag{3.1}$$

A visual representation of this approximation is given in Figure 1, illustrating how the physical domain Ω is discretized into the computational domain Ω_h, which is composed of K non-overlapping elements Ω_h^k.

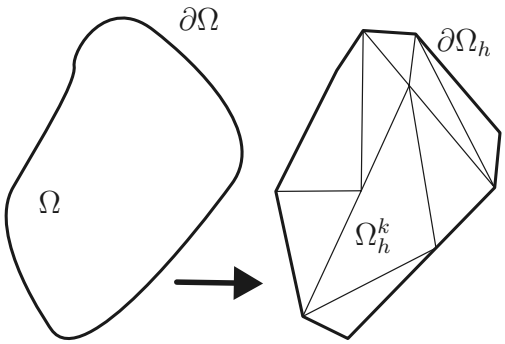

Figure 1 – Approximation of the physical domain by the computational domain.

3.2 Solving Conservation Laws

As the DGTD method has found widespread application in the solution of conservation laws, it is essential to consider its formulation in this context. In light of this, this section concentrates on the derivation of the DGTD method concerning a general conservation law of the form

$$\frac{\partial u(\boldsymbol{x},t)}{\partial t} + \nabla \cdot \boldsymbol{f}\left(u(\boldsymbol{x},t),\boldsymbol{x},t\right) = 0, \tag{3.2}$$

where the solution $u(\boldsymbol{x},t)$ is a fundamental quantity that represents the conserved property in the system under consideration. The flux $\boldsymbol{f}(u(\boldsymbol{x},t),\boldsymbol{x},t)$ represents the flow of $u(\boldsymbol{x},t)$ in space and time, and $\boldsymbol{x}$ and t denote the spatial position and time, respectively. It is noteworthy that $u(\boldsymbol{x},t)$ is kept as a scalar for simplicity in the conservation law formulation without loss of generality.

In numerical simulations of physical systems, it is often necessary to approximate the physical solution $u(\boldsymbol{x},t)$ by a numerical solution $u_h(\boldsymbol{x},t)$. This numerical solution is typically constructed as the sum of local numerical solutions $u_h^k(\boldsymbol{x},t)$ that are associated with each of the K elements Ω_h^k. The numerical solution $u_h(\boldsymbol{x},t)$ is chosen to reside in a vector space $\mathcal{V}_h$ that is spanned by a set of basis functions defined within each element Ω_h^k. Each local numerical solution $u_h^k(\boldsymbol{x},t)$ is then constructed as a linear combination of N_p basis functions. That is

$$u(\boldsymbol{x},t) \approx u_h(\boldsymbol{x},t) = \bigoplus_{k=1}^{K} u_h^k(\boldsymbol{x},t) \in \mathcal{V}_h = \bigoplus_{k=1}^{K} \{\psi_n(\boldsymbol{x})\}_{n=1}^{N_p} \quad \boldsymbol{x} \in \Omega_h^k, \tag{3.3}$$

where $\psi_n(\boldsymbol{x})$ such that $\boldsymbol{x} \in \Omega_h^k$ is the nth basis function associated with the kth element Ω_h^k. The aforementioned expression is commonly referred to as the modal form [6].

The local numerical solution can also be expressed in terms of nodal values, as in

$$u_h^k(\boldsymbol{x}, t) = \sum_{i=1}^{N_p} u_h^k(\boldsymbol{x}_i, t) l_i^k(\boldsymbol{x}) \quad \boldsymbol{x} \in \Omega_h^k,$$

where $l_i^k(\boldsymbol{x})$ is the ith Lagrange polynomial associated with the kth element Ω_h^k. It should be noted that the expression discussed above is commonly known as the nodal form [6].

This chapter will primarily analyze the nodal form for solving mathematical problems, despite the fact that both forms yield the same solution. The nodal form is chosen due to its simpler computational implementation [6]. Moreover, to simplify the notation, hereafter, the approximate local flux $\boldsymbol{f}_h^k(u_h(\boldsymbol{x}, t), \boldsymbol{x}, t)$ and approximate local solution $u_h^k(\boldsymbol{x}, t)$ will be denoted as $\boldsymbol{f}_h^k$ and u_h^k, respectively. It is important to observe that $\boldsymbol{x}$ is still regarded as being within the local approximated domain Ω_h^k.

In the Galerkin approach, where both the solution and test functions belong to the same vector space, it is required to ensure that the residual $R_h^k(\boldsymbol{x}, t) = \dfrac{\partial u_h^k}{\partial t} + \nabla \cdot \boldsymbol{f}_h^k$ is orthogonal to a test function like $v_h^k(\boldsymbol{x}, t) \in \mathcal{V}_h$. This implies that

$$\int_{\Omega_h^k} \left(\frac{\partial u_h^k}{\partial t} + \nabla \cdot \boldsymbol{f}_h^k \right) l_i^k(\boldsymbol{x}) \, d\Omega = 0 \quad i = 1, 2, \ldots, N_p. \tag{3.4}$$

The vector identity $\nabla \cdot (\phi \boldsymbol{A}) = \phi \nabla \cdot \boldsymbol{A} + \boldsymbol{A} \cdot \nabla \phi$ can then be applied as

$$\nabla \cdot \boldsymbol{f}_h^k l_i^k(\boldsymbol{x}) = \nabla \cdot \left(\boldsymbol{f}_h^k l_i^k(\boldsymbol{x}) \right) - \boldsymbol{f}_h^k(u_h, \boldsymbol{x}, t) \cdot \nabla l_i^k(\boldsymbol{x}). \tag{3.5}$$

Therefore, replacing Equation (3.5) in Equation (3.4), leads to

$$\int_{\Omega_h^k} \left(\frac{\partial u_h^k}{\partial t} l_i^k(\boldsymbol{x}) - \boldsymbol{f}_h^k \cdot \nabla l_i^k(\boldsymbol{x}) \right) d\Omega = - \int_{\Omega_h^k} \nabla \cdot \left(\boldsymbol{f}_h^k l_i^k(\boldsymbol{x}) \right) d\Omega \quad i = 1, 2, \ldots, N_p. \tag{3.6}$$

Applying the divergence theorem to the above equation leads to the weak form [6]

$$\int_{\Omega_h^k} \left(\frac{\partial u_h^k}{\partial t} l_i^k(\boldsymbol{x}) - \boldsymbol{f}_h^k \cdot \nabla l_i^k(\boldsymbol{x}) \right) d\Omega = - \int_{\partial \Omega_h^k} \hat{n} \cdot \boldsymbol{f}_h^{*k} l_i^k(\boldsymbol{x}) \, d\Omega \quad i = 1, 2, \ldots, N_p. \tag{3.7}$$

where $\boldsymbol{f}^*$ is the numerical flux yet to be ascertained.

Reapplying Equation (3.5) to Equation (3.7), leads to

$$\int_{\Omega_h^k} \left[\frac{\partial u_h^k}{\partial t} l_i^k(\boldsymbol{x}) + \left(\nabla \cdot \boldsymbol{f}_h^k \right) l_i^k(\boldsymbol{x}) - \nabla \cdot \left(\boldsymbol{f}_h^k l_i^k(\boldsymbol{x}) \right) \right] d\Omega = - \int_{\partial \Omega_h^k} \hat{n} \cdot \boldsymbol{f}_h^{*k} l_i^k(\boldsymbol{x}) \, d\Omega \quad i = 1, 2, \ldots, N_p. \tag{3.8}$$

Finally, applying the divergence theorem to the previous equation leads to the strong form [6]

$$\int_{\Omega_h^k} \left(\frac{\partial u_h^k}{\partial t} + \nabla \cdot \boldsymbol{f}_h^k \right) l_i^k(\boldsymbol{x}) \, d\Omega = \int_{\partial \Omega_h^k} \hat{n} \cdot \left(\boldsymbol{f}_h^k - \boldsymbol{f}_h^{*k} \right) l_i^k(\boldsymbol{x}) \, d\Omega \quad i = 1, 2, \ldots, N_p. \tag{3.9}$$

3.3 The Nodal Element

The following subsections provide a mathematical framework that addresses the construction of the nodal element in one, two, and three dimensions.

3.3.1 One Dimension

This section discusses the construction of a one-dimensional high-order nodal element.

3.3.1.1 Modes and Nodes

Assuming that the solution for each element can be expressed as

$$u_h^k(x,t) = \sum_{i=1}^{N_p} u_h^k(x_i,t) l_i^k(x) = \sum_{n=1}^{N_p} \hat{u}_n^k(t)\psi_n(x) \quad x \in \Omega_h^k, \tag{3.10}$$

where the Lagrange polynomial is denoted as $l_i^k(x)$, the interpolation locations are represented by x_i, and the set of polynomials $\{\psi_n(x)\}_{n=1}^{N_p}$ serves as a genuine one-dimensional polynomial basis of order N. In the case of a one-dimensional simplex, the number of basis functions N_p is related to the element order N through the equation $N_p = N + 1$.

3.3.1.2 Reference Element Mapping

Introducing a mapping Ψ connecting the global segment with vertices v_1 and v_2 such that $x \in \Omega_h^k$, with the reference segment where $r \in I$ such that $-1 \leq r \leq 1$ as seen in Figure 2.

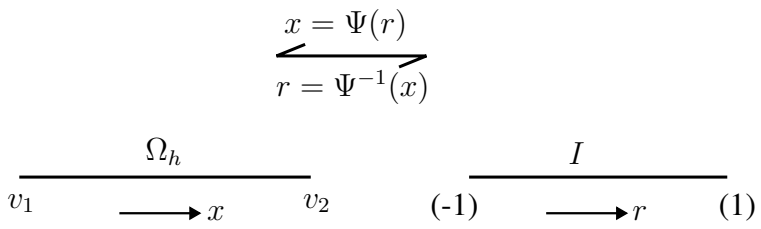

Figure 2 – Notation for the mapping between two one-dimensional simplices.

The direct mapping is given by

$$x = \frac{-r+1}{2} v_1 + \frac{r+1}{2} v_2 = \Psi(r). \tag{3.11}$$

Given the linearity in r, the transformation is affine and the Jacobian is constant. It can be shown that

$$\frac{dx}{dr} = \frac{v_2 - v_1}{2}, \tag{3.12}$$

leading to

$$\frac{dr}{dx} = \frac{1}{J}, \tag{3.13}$$

where the Jacobian is given by

$$J = \frac{dx}{dr}. \tag{3.14}$$

3.3.1.3 Choosing the Basis Functions and Interpolating Positions

Since there is a direct correspondence between the global and reference elements, it is possible to conduct further analysis solely focusing on the reference element. As a result, the solution can be represented in the reference domain as

$$u(r,t) = \sum_{n=1}^{N_p} \hat{u}_n(t)\psi_n(r) = \sum_{i=1}^{N_p} u(r_i,t)l_i(r), \tag{3.15}$$

where modal coefficients $\hat{u}_n(t)$ and nodal coefficients $u(r_i,t)$ can be connected through the Vandermonde matrix V such that $V\hat{\boldsymbol{u}} = \boldsymbol{u}$ where $\hat{\boldsymbol{u}} = \left[\hat{u}_1(t),\ldots,\hat{u}_{N_p}(t)\right]^\intercal$, $\boldsymbol{u} = \left[u(r_1,t),\ldots,u(r_{N_p},t)\right]^\intercal$ and the elements of V are $V_{ij} = \psi_j(r_i)$.

As observed, the utilization of high-order nodal basis functions presents two challenges. The first challenge involves selecting a suitable set of basis functions, denoted as ψ_n, which will span the vector space that contains the solution. The second challenge involves finding good positions for the nodal values r_i to minimize interpolation error.

Both of these challenges are relatively straightforward when considering the one-dimensional case. The commonly employed basis functions are orthonormal polynomials derived from Legendre polynomials, resulting in

$$\psi_n(r) = \sqrt{\frac{2n-1}{2}}P_{n-1}(r), \tag{3.16}$$

where $P_n(r)$ are the classic Legendre polynomials of order n which can be computed through recurrence.

The second concern pertains to the identification of suitable positions for the nodal values. This objective can be accomplished by determining the positions that minimize the Lebesgue constant, which is defined as follows

$$\Lambda = \max_r \sum_{i=1}^{N_p} |l_i(r)|. \tag{3.17}$$

Fortunately, it is well-established that the Legendre-Gauss-Lobatto quadrature points offer near-minimal Lebesgue constant values for the one-dimensional simplex [6]. Hence, by the careful selection of the orthonormal Legendre basis and usage of Legendre-Gauss-Lobatto nodal quadrature points, it is possible to guarantee that the Vandermonde matrix V possesses good conditioning and that the resultant interpolation is well-behaved.

3.3.1.4 Elementwise Operations

The global mass matrix M^k and reference mass matrix M can be defined as

$$M_{ij}^k = \int_{\Omega_h^k} l_i^k(x) l_j^k(x)\, d\Omega = J^k \int_I l_i(r) l_j(r) dr = J^k M_{ij} \tag{3.18}$$

where J^k is constant for the one-dimensional simplex. Given that V is constructed using an orthonormal basis, it follows that $M^k = J^k (VV^\intercal)^{-1}$.

Likewise, the global stiffness matrix S^k and reference stiffness matrix S can be defined as

$$S_{ij}^k = \int_{\Omega_h^k} l_i^k(x) \frac{dl_j^k(x)}{dx}\, d\Omega = \int_I l_i(r) \frac{dl_j(r)}{dr} dr = S_{ij}. \tag{3.19}$$

Defining the differentiation matrix D_r such that

$$\frac{\partial u}{\partial r} \approx \sum_{j=1}^{N_p} \left.\frac{\partial l_j(r)}{\partial r}\right|_{r=r_i} u(r_j, t) = (D_r \mathbf{u})_i, \tag{3.20}$$

it follows that

$$D_r V = V_r, \tag{3.21}$$

where

$$V_{r,(i,j)} = \left.\frac{\partial \psi_j(r)}{\partial r}\right|_{r=r_i}. \tag{3.22}$$

Therefore, the corresponding reference stiffness matrix is given by

$$S = M D_r. \tag{3.23}$$

Finally, the right-hand side of the scheme requires the computation of the surface integral

$$\int_{\partial\Omega_h^k} \hat{n} \cdot \boldsymbol{g}_h l_i^k(\boldsymbol{x})\, d\Omega = \sum_{j=1}^{N_{fp}} \hat{n} \cdot \boldsymbol{g}_j \int_{\partial\Omega_h^k} l_j^k(\boldsymbol{x}) l_i^k(\boldsymbol{x})\, d\Omega \tag{3.24}$$

where $N_{fp} = 2$ represents the number of nodes on the vertices of the element and $\boldsymbol{g}_h$ denotes the flux or jump in flux. This calculation is straightforward as there are only two vertices involved. In order to generalize this notation to the one-dimensional case, it is necessary to define the values of $\hat{n}$, which take on a value of $+1$ at the right vertex of the element and -1 at the left vertex of the element.

3.3.2 Two Dimensions

This section discusses the construction of a two-dimensional high-order nodal element.

3.3.2.1 Modes and Nodes

Assuming that the solution for each element can be expressed as

$$u_h^k(\boldsymbol{x},t) = \sum_{i=1}^{N_p} u_h^k(\boldsymbol{x}_i,t) l_i^k(\boldsymbol{x}) = \sum_{n=1}^{N_p} \hat{u}_n^k(t)\psi_n(\boldsymbol{x}) \quad \boldsymbol{x} \in \Omega_h^k, \tag{3.25}$$

where the multidimensional Lagrange polynomial is denoted as $l_i^k(\boldsymbol{x})$, the interpolation locations are represented by $\boldsymbol{x}_i$, and the set of polynomials $\{\psi_n(\boldsymbol{x})\}_{n=1}^{N_p}$ serves as a genuine two-dimensional polynomial basis of order N. In the case of a two-dimensional simplex, the number of basis functions N_p is related to the element order N through the equation $N_p = (N+1)(N+2)/2$.

3.3.2.2 Reference Element Mapping

Introducing a mapping Ψ connecting the global triangle with vertices $\boldsymbol{v}_1$, $\boldsymbol{v}_2$ and $\boldsymbol{v}_3$ such that $\boldsymbol{x} \in \Omega_h^k$, with the reference triangle where $\boldsymbol{r} \in I$ such that $\boldsymbol{r} = (r,s)|(r,s) \geq -1; r+s \leq 0$ as seen in Figure 3.

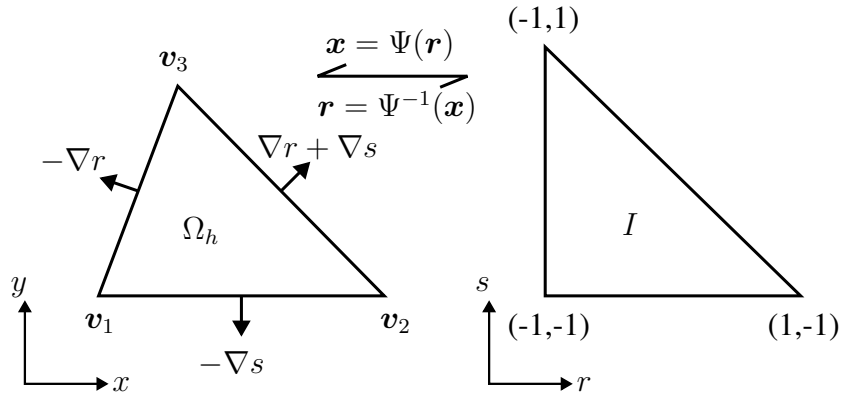

Figure 3 – Notation for the mapping between two two-dimensional simplices.

Defining the barycentric coordinates $(\lambda_1, \lambda_2, \lambda_3)$ with the following properties: $0 \leq \lambda_i \leq 1$ and $\lambda_1 + \lambda_2 + \lambda_3 = 1$. The direct mapping can be obtained as

$$\boldsymbol{x} = \lambda_1 \boldsymbol{v}_1 + \lambda_2 \boldsymbol{v}_2 + \lambda_3 \boldsymbol{v}_3 = \Psi(\boldsymbol{r}), \tag{3.26}$$

where

$$\lambda_1 = -\frac{r+s}{2} \quad \lambda_2 = \frac{r+1}{2} \quad \lambda_3 = \frac{s+1}{2}.$$

Given that the mapping is linear in $\boldsymbol{r}$, both triangles are connected through an affine mapping resulting in a constant transformation Jacobian. It can be shown that

$$\frac{\partial \boldsymbol{x}}{\partial r} = \frac{\boldsymbol{v}_2 - \boldsymbol{v}_1}{2} \qquad \frac{\partial \boldsymbol{x}}{\partial s} = \frac{\boldsymbol{v}_3 - \boldsymbol{v}_1}{2}, \tag{3.27}$$

leading to

$$\frac{\partial r}{\partial x} = \frac{1}{J}\frac{\partial y}{\partial s} \quad \frac{\partial r}{\partial y} = -\frac{1}{J}\frac{\partial x}{\partial s} \quad \frac{\partial s}{\partial x} = -\frac{1}{J}\frac{\partial y}{\partial r} \quad \frac{\partial s}{\partial y} = \frac{1}{J}\frac{\partial x}{\partial r} \tag{3.28}$$

where the Jacobian is given by

$$J = \frac{\partial x}{\partial r}\frac{\partial y}{\partial s} - \frac{\partial x}{\partial s}\frac{\partial y}{\partial r}. \tag{3.29}$$

3.3.2.3 Choosing the Basis Functions and Interpolating Positions

Given the presence of a mapping that allows for the transition between reference and global elements, all subsequent analysis can be conducted on the reference element. This allows for a more efficient implementation. As a result, the solution can be represented as

$$u(\boldsymbol{r}, t) = \sum_{n=1}^{N_p} \hat{u}_n(t)\psi_n(\boldsymbol{r}) = \sum_{i=1}^{N_p} u(\boldsymbol{r}_i, t) l_i(\boldsymbol{r}), \tag{3.30}$$

and modal coefficients $\hat{u}_n(t)$ and nodal coefficients $u(\boldsymbol{r}_i, t)$ can be connected through the Vandermonde matrix V such that $V\hat{\boldsymbol{u}} = \boldsymbol{u}$ where $\hat{\boldsymbol{u}} = \left[\hat{u}_1(t), \ldots, \hat{u}_{N_p}(t)\right]^\intercal$, $\boldsymbol{u} = \left[u(\boldsymbol{r}_1, t), \ldots, u(\boldsymbol{r}_{N_p}, t)\right]^\intercal$ and the coefficients of V are $V_{ij} = \psi_j(\boldsymbol{r}_i)$.

As previously observed, the utilization of high-order nodal basis functions presents two challenges. The first challenge involves selecting a suitable set of functions, denoted as ψ_n, which will span the vector space that contains the solution. The second challenge involves finding good positions for the nodal values in order to minimize interpolation error.

One possible solution to overcome the initial challenge is by selecting orthonormal monomials [6], leading to the following basis functions

$$\psi_m(\boldsymbol{r}) = \sqrt{2} P_i^{(0,0)}(a) P_j^{(2i+1,0)}(b)(1-b)^i, \tag{3.31}$$

where $P_n^{(\alpha,\beta)}(x)$ is the nth order Jacobi polynomial with parameters α and β. Additionally, the remaining indices are defined as

$$m = j + (N+1)i + 1 - \frac{i}{2}(i-1), \quad (i,j) \geq 0; \quad i + j \leq N, \tag{3.32}$$

$$a = 2\frac{1+r}{1-s} - 1 \quad b = s. \tag{3.33}$$

The second issue, which presents a greater challenge, involves the selection of nodal value positions with the aim of minimizing the interpolation error. One approach to achieve this is to begin with an equidistant distribution and through a mapping obtain a distribution resembling Legendre-Gauss-Lobatto, as the Warp&Blend method suggests [6]. These nodal sets can be connected by

$$\omega(r) = \sum_{i=1}^{N_p} (r_i^{LGL} - r_i^e) l_i^e(r), \tag{3.34}$$

where $l_i^e(r)$ are the Lagrange polynomials based on the equidistant points r_i^e. Therefore, $w(r)$ is an N-order transformation mapping equidistant points to the Legendre-Gauss-Lobatto points. The correction $\boldsymbol{w}(\lambda_1, \lambda_2, \lambda_3)$ vector can be defined as

$$\boldsymbol{w}(\lambda_1, \lambda_2, \lambda_3) = \sum_{i=1}^{3} \left(1 + (\alpha\lambda_i)^2\right) b_i \boldsymbol{w}_i, \tag{3.35}$$

where

$$b_1(\lambda_1, \lambda_2, \lambda_3) = 4\lambda_2\lambda_3 \quad b_2(\lambda_1, \lambda_2, \lambda_3) = 4\lambda_1\lambda_3 \quad b_3(\lambda_1, \lambda_2, \lambda_3) = 4\lambda_1\lambda_2, \tag{3.36}$$

where

$$\boldsymbol{w}_1(\lambda_1, \lambda_2, \lambda_3) = \tilde{w}(\lambda_3 - \lambda_2) \begin{bmatrix} 1 \\ 0 \end{bmatrix}, \tag{3.37}$$

$$\boldsymbol{w}_2(\lambda_1, \lambda_2, \lambda_3) = \tilde{w}(\lambda_1 - \lambda_3) \frac{1}{2} \begin{bmatrix} -1 \\ \sqrt{3} \end{bmatrix}, \tag{3.38}$$

$$\boldsymbol{w}_3(\lambda_1, \lambda_2, \lambda_3) = \tilde{w}(\lambda_2 - \lambda_1) \frac{1}{2} \begin{bmatrix} -1 \\ -\sqrt{3} \end{bmatrix}, \tag{3.39}$$

considering

$$\tilde{w}(r) = \frac{\omega(r)}{1 - r^2}. \tag{3.40}$$

The parameter α can be utilized to minimize the Lebesgue constant. A simulation of these values is provided in Table 3. It is evident that, particularly at higher orders, the application of the Warp&Blend method can result in a Vandermonde matrix that exhibits better conditioning.

3.3.2.4 Elementwise Operations

The global mass matrix M^k and reference mass matrix M can be defined as

$$M_{ij}^k = \int_{\Omega_h^k} l_i^k(\boldsymbol{x}) l_j^k(\boldsymbol{x})\, d\Omega = J^k \int_I l_i(\boldsymbol{r}) l_j(\boldsymbol{r}) d\boldsymbol{r} = J^k M_{ij} \tag{3.41}$$

where J^k is constant for the two-dimensional simplex. Given that V is constructed using an orthonormal basis, it follows that $M^k = J^k (V V^\intercal)^{-1}$.

From the chain rule, it can be shown that

$$\frac{\partial}{\partial x} = \frac{\partial r}{\partial x}\mathcal{D}_r + \frac{\partial s}{\partial x}\mathcal{D}_s, \tag{3.42}$$

$$\frac{\partial}{\partial y} = \frac{\partial r}{\partial y}\mathcal{D}_r + \frac{\partial s}{\partial y}\mathcal{D}_s, \tag{3.43}$$

where $\mathcal{D}_r$ and $\mathcal{D}_s$ represent differentiation operators with respect to r and s. We have the derivative Vandermonde matrices

$$V_{r,(i,j)} = \left.\frac{\partial \psi_j}{\partial r}\right|_{\boldsymbol{r}_i} \qquad V_{s,(i,j)} = \left.\frac{\partial \psi_j}{\partial s}\right|_{\boldsymbol{r}_i}, \tag{3.44}$$

Table 3 – Optimization of the parameter α – Two-dimensional

N	α	$\Lambda(\alpha = 0)$	$\Lambda(\alpha$-optimized)	Λ (equidistant)
1	0.0000	1.0000	1.0000	1.0000
2	0.0000	1.6664	1.6664	1.6664
3	0.0000	2.1125	2.1125	2.2692
4	0.0000	2.6606	2.6606	3.4704
5	0.2623	3.1183	3.1164	5.4518
6	0.9851	3.8094	3.6969	8.7356
7	1.0941	4.5447	4.2698	14.3350
8	1.2791	5.6925	4.9451	23.8929
9	1.3668	7.0090	5.7252	40.7845
10	1.4562	9.0752	6.6416	70.5278
11	1.4979	11.8344	7.8848	124.4166
12	1.5454	16.0619	9.2698	217.6584
13	1.5514	21.2122	11.3191	391.0552
14	1.6136	28.8329	13.8568	718.5429
15	1.6270	40.6689	17.6017	1315.4392
16	1.6630	59.2122	21.5660	2399.0527
17	1.8941	87.1553	27.5340	4358.4757
18	1.7185	128.2434	34.6365	7887.6292
19	1.9168	189.0977	47.0611	14226.4582

where the derivatives of the basis functions are computed using the chain rule involving a and b:

$$\frac{\partial \psi_j}{\partial r} = \frac{\partial a}{\partial r}\frac{\partial \psi_j}{\partial a}, \quad \frac{\partial \psi_j}{\partial s} = \frac{\partial a}{\partial s}\frac{\partial \psi_j}{\partial a} + \frac{\partial b}{\partial s}\frac{\partial \psi_j}{\partial b}. \tag{3.45}$$

Defining the reference differentiation matrices

$$D_r = V_r V^{-1} \quad D_s = V_s V^{-1}, \tag{3.46}$$

the corresponding reference stiffness matrices are given by

$$S_r = M D_r \quad S_s = M D_s. \tag{3.47}$$

Finally, the right-hand side of the scheme requires the computation of the surface integral

$$\int_{\partial\Omega_h^k} \hat{\boldsymbol{n}} \cdot \boldsymbol{g}_h l_i^k(\boldsymbol{x})\, d\Omega = \sum_{j=1}^{N_{fp}} \hat{\boldsymbol{n}} \cdot \boldsymbol{g}_j \int_{\partial\Omega_h^k} l_j^k(\boldsymbol{x}) l_i^k(\boldsymbol{x})\, d\Omega \tag{3.48}$$

where N_{fp} is the number of nodes on the edges of the element and $\boldsymbol{g}_h$ is the flux or jump in flux.

Fortunately, this refers to the mass matrix of the edges, specifically it is the mass matrix already developed in the one-dimensional case.

3.3.3 Three Dimensions

3.3.3.1 Modes and Nodes

Assuming that the solution for each element can be expressed as

$$u_h^k(\boldsymbol{x},t) = \sum_{i=1}^{N_p} u_h^k(\boldsymbol{x}_i,t) l_i^k(\boldsymbol{x}) = \sum_{n=1}^{N_p} \hat{u}_n^k(t)\psi_n(\boldsymbol{x}) \quad \boldsymbol{x} \in \Omega_h^k, \tag{3.49}$$

where $l_i^k(\boldsymbol{x})$ is the multidimensional Lagrange polynomial, $\boldsymbol{x}_i$ are the interpolation locations, and $\{\psi_n(\boldsymbol{x})\}_{n=1}^{N_p}$ is a genuine three-dimensional polynomial basis of order N. In a three-dimensional simplex, the order of the element N and the number of basis functions N_p are related by $N_p = (N+1)(N+2)(N+3)/6$.

3.3.3.2 Reference Element Mapping

Introducing a mapping Ψ connecting the global tetrahedron, $\boldsymbol{x} \in \Omega_h^k$, with the reference tetrahedron defined as $I = \{\boldsymbol{r} = (r,s,t) | (r,s,t) \geq -1; r+s+t \leq -1\}$.

Defining the barycentric coordinates $(\lambda_1, \lambda_2, \lambda_3, \lambda_4)$ with vertices $\boldsymbol{v}_1, \boldsymbol{v}_2, \boldsymbol{v}_3, \boldsymbol{v}_4$ and the properties: $0 \leq \lambda_i \leq 1$ and $\lambda_1 + \lambda_2 + \lambda_3 + \lambda_4 = 1$. The direct mapping can be obtained as

$$\boldsymbol{x} = \lambda_1 \boldsymbol{v}_1 + \lambda_2 \boldsymbol{v}_2 + \lambda_3 \boldsymbol{v}_3 + \lambda_4 \boldsymbol{v}_4 = \Psi(\boldsymbol{r}), \tag{3.50}$$

where

$$\lambda_1 = -\frac{r+s+t+1}{2} \quad \lambda_2 = \frac{r+1}{2} \quad \lambda_3 = \frac{s+1}{2} \quad \lambda_4 = \frac{t+1}{2}. \tag{3.51}$$

Noticing that the mapping is linear in $\boldsymbol{r}$ with a constant Jacobian given the affine transformation, the inverse mapping derivatives can be obtained as

$$\begin{bmatrix} \frac{\partial r}{\partial x} & \frac{\partial r}{\partial y} & \frac{\partial r}{\partial z} \\ \frac{\partial s}{\partial x} & \frac{\partial s}{\partial y} & \frac{\partial s}{\partial z} \\ \frac{\partial t}{\partial x} & \frac{\partial t}{\partial y} & \frac{\partial t}{\partial z} \end{bmatrix} = \frac{1}{J} \begin{bmatrix} \frac{\partial y}{\partial s}\frac{\partial z}{\partial t} - \frac{\partial z}{\partial s}\frac{\partial y}{\partial t} & -\frac{\partial x}{\partial s}\frac{\partial z}{\partial t} + \frac{\partial z}{\partial s}\frac{\partial x}{\partial t} & \frac{\partial x}{\partial s}\frac{\partial y}{\partial t} - \frac{\partial y}{\partial s}\frac{\partial x}{\partial t} \\ -\frac{\partial y}{\partial r}\frac{\partial z}{\partial t} + \frac{\partial z}{\partial r}\frac{\partial y}{\partial t} & \frac{\partial x}{\partial r}\frac{\partial z}{\partial t} - \frac{\partial z}{\partial r}\frac{\partial x}{\partial t} & -\frac{\partial x}{\partial r}\frac{\partial y}{\partial t} + \frac{\partial y}{\partial r}\frac{\partial x}{\partial t} \\ \frac{\partial y}{\partial r}\frac{\partial z}{\partial s} - \frac{\partial z}{\partial r}\frac{\partial y}{\partial s} & -\frac{\partial x}{\partial r}\frac{\partial z}{\partial s} + \frac{\partial z}{\partial r}\frac{\partial x}{\partial s} & \frac{\partial x}{\partial r}\frac{\partial y}{\partial s} - \frac{\partial y}{\partial r}\frac{\partial x}{\partial s} \end{bmatrix}, \tag{3.52}$$

where the Jacobian determinant J is

$$J = \det \begin{bmatrix} \frac{\partial x}{\partial r} & \frac{\partial x}{\partial s} & \frac{\partial x}{\partial t} \\ \frac{\partial y}{\partial r} & \frac{\partial y}{\partial s} & \frac{\partial y}{\partial t} \\ \frac{\partial z}{\partial r} & \frac{\partial z}{\partial s} & \frac{\partial z}{\partial t} \end{bmatrix}. \tag{3.53}$$

3.3.3.3 Choosing the Basis Functions and Interpolating Positions

Since the reasoning is identical to that demonstrated in the two-dimensional scenario, this section will present the basis function and the correction vector $\boldsymbol{w}(\lambda_1, \lambda_2, \lambda_3, \lambda_4)$ employed to achieve a distribution resembling Legendre-Gauss-Lobatto.

The basis function is

$$\psi_m(\boldsymbol{r}) = \sqrt{8}P_i^{(0,0)}(a)P_j^{(2i+1,0)}(b)(1-b)^i P_k^{(2i+2j+2,0)}(c)(1-c)^{i+j}$$

where the multi-index m is defined for $0 \leq i, j, k; i+j+k \leq N$ as

$$m = 1 + k + \sum_{p=0}^{i+j-1}(N+1-p) + \sum_{p=0}^{i-1}\frac{(N-p)(N-p+1)}{2}, \tag{3.54}$$

and where

$$a = -2\frac{(1+r)}{s+t} - 1 \quad b = 2\frac{(1+s)}{1-t} - 1 \quad c = t. \tag{3.55}$$

The correction vector $\boldsymbol{w}$ for the Warp&Blend nodes is given by

$$\boldsymbol{w}(\lambda_1, \lambda_2, \lambda_3, \lambda_4) = \sum_{i=1}^{4}(1 + (\alpha\lambda_i)^2)b_i\boldsymbol{w}_i, \tag{3.56}$$

where $\boldsymbol{w}_i$ are face-based warpings and b_i are blend functions. The warpings $\boldsymbol{w}_i$ are based on the 2D warp functions $\boldsymbol{g}_1, \boldsymbol{g}_2$ applied to the barycentric coordinates of the faces, projected by vectors $\boldsymbol{t}_{i,j}$ [6].

$$\boldsymbol{w}_1 = \boldsymbol{g}_1(\lambda_2, \lambda_3, \lambda_4)\boldsymbol{t}_{1,1} + \boldsymbol{g}_2(\lambda_2, \lambda_3, \lambda_4)\boldsymbol{t}_{1,2}, \tag{3.57}$$

$$\boldsymbol{w}_2 = \boldsymbol{g}_1(\lambda_1, \lambda_3, \lambda_4)\boldsymbol{t}_{2,1} + \boldsymbol{g}_2(\lambda_1, \lambda_3, \lambda_4)\boldsymbol{t}_{2,2}, \tag{3.58}$$

$$\boldsymbol{w}_3 = \boldsymbol{g}_1(\lambda_1, \lambda_4, \lambda_2)\boldsymbol{t}_{3,1} + \boldsymbol{g}_2(\lambda_1, \lambda_4, \lambda_2)\boldsymbol{t}_{3,2}, \tag{3.59}$$

$$\boldsymbol{w}_4 = \boldsymbol{g}_1(\lambda_1, \lambda_3, \lambda_2)\boldsymbol{t}_{4,1} + \boldsymbol{g}_2(\lambda_1, \lambda_3, \lambda_2)\boldsymbol{t}_{4,2}. \tag{3.60}$$

The projection vectors $\boldsymbol{t}_{i,j}$ are:

$$\boldsymbol{t}_{1,1} = \begin{bmatrix}1\\0\\0\end{bmatrix} \quad \boldsymbol{t}_{1,2} = \begin{bmatrix}0\\1\\0\end{bmatrix} \quad \boldsymbol{t}_{2,1} = \begin{bmatrix}1\\0\\0\end{bmatrix} \quad \boldsymbol{t}_{2,2} = \begin{bmatrix}0\\1/3\\\sqrt{8}/3\end{bmatrix} \tag{3.61}$$

$$\boldsymbol{t}_{3,1} = \begin{bmatrix}-1/2\\\sqrt{3}/2\\0\end{bmatrix} \quad \boldsymbol{t}_{3,2} = \begin{bmatrix}-\sqrt{1/12}\\1/6\\\sqrt{8}/3\end{bmatrix} \quad \boldsymbol{t}_{4,1} = \begin{bmatrix}-1/2\\-\sqrt{3}/2\\0\end{bmatrix} \quad \boldsymbol{t}_{4,2} = \begin{bmatrix}\sqrt{1/12}\\-1/6\\\sqrt{8}/3\end{bmatrix} \tag{3.62}$$

The blend functions b_i are:

$$b_1(\lambda_1, \lambda_2, \lambda_3, \lambda_4) = \frac{8\lambda_2\lambda_3\lambda_4}{(2\lambda_2 + \lambda_1)(2\lambda_3 + \lambda_1)(2\lambda_4 + \lambda_1)} \tag{3.63}$$

$$b_2(\lambda_1, \lambda_2, \lambda_3, \lambda_4) = \frac{8\lambda_1\lambda_3\lambda_4}{(2\lambda_1 + \lambda_2)(2\lambda_3 + \lambda_2)(2\lambda_4 + \lambda_2)} \tag{3.64}$$

$$b_3(\lambda_1, \lambda_2, \lambda_3, \lambda_4) = \frac{8\lambda_1\lambda_2\lambda_4}{(2\lambda_1 + \lambda_3)(2\lambda_2 + \lambda_3)(2\lambda_4 + \lambda_3)} \tag{3.65}$$

$$b_4(\lambda_1, \lambda_2, \lambda_3, \lambda_4) = \frac{8\lambda_1\lambda_2\lambda_3}{(2\lambda_1 + \lambda_4)(2\lambda_2 + \lambda_4)(2\lambda_3 + \lambda_4)} \tag{3.66}$$

The parameter α can be utilized to minimize the Lebesgue constant. A simulation of these values is provided in Table 4. It is evident that, particularly at higher orders, the application of the Warp&Blend method can result in a Vandermonde matrix that exhibits better conditioning.

Table 4 – Optimization of the parameter α – Three-dimensional

N	α	$\Lambda(\alpha$-optimized)	Λ (equidistant)
1	0.0000	1.00	1.00
2	0.0000	2.00	2.00
3	0.0000	2.93	3.00
4	0.1002	4.07	4.88
5	1.1332	5.32	8.09
6	1.5608	7.01	13.66
7	1.3413	9.21	23.38
8	1.2577	12.54	40.55
9	1.1603	17.02	71.15
10	1.0153	24.36	126.20
11	0.6080	36.35	225.99
12	0.4523	54.18	409.15
13	0.8856	84.62	742.69
14	0.8717	135.75	1360.49
15	0.9655	217.70	2506.95

3.3.3.4 Elementwise Operations

The global mass matrix M^k and reference mass matrix M can be defined as

$$M_{ij}^k = \int_{\Omega_h^k} l_i^k(\boldsymbol{x}) l_j^k(\boldsymbol{x})\, d\Omega = J^k \int_I l_i(\boldsymbol{r}) l_j(\boldsymbol{r}) d\boldsymbol{r} = J^k M_{ij} \tag{3.67}$$

where J^k is constant for the three-dimensional simplex. Given that V is constructed using an orthonormal basis, it follows that $M^k = J^k(VV^\intercal)^{-1}$.

From the chain rule, it can be shown that

$$\frac{\partial}{\partial x} = \frac{\partial r}{\partial x}\mathcal{D}_r + \frac{\partial s}{\partial x}\mathcal{D}_s + \frac{\partial t}{\partial x}\mathcal{D}_t \tag{3.68}$$

$$\frac{\partial}{\partial y} = \frac{\partial r}{\partial y}\mathcal{D}_r + \frac{\partial s}{\partial y}\mathcal{D}_s + \frac{\partial t}{\partial y}\mathcal{D}_t \tag{3.69}$$

$$\frac{\partial}{\partial z} = \frac{\partial r}{\partial z}\mathcal{D}_r + \frac{\partial s}{\partial z}\mathcal{D}_s + \frac{\partial t}{\partial z}\mathcal{D}_t \tag{3.70}$$

where $\mathcal{D}_r, \mathcal{D}_s, \mathcal{D}_t$ are differentiation operators. The derivative Vandermonde matrices are

$$V_{r,(i,j)} = \left.\frac{\partial \psi_j}{\partial r}\right|_{\boldsymbol{r}_i} \quad V_{s,(i,j)} = \left.\frac{\partial \psi_j}{\partial s}\right|_{\boldsymbol{r}_i} \quad V_{t,(i,j)} = \left.\frac{\partial \psi_j}{\partial t}\right|_{\boldsymbol{r}_i} \tag{3.71}$$

where the derivatives of the basis functions involve the chain rule with a, b, c:

$$\frac{\partial \psi_j}{\partial r} = \frac{\partial a}{\partial r}\frac{\partial \psi_j}{\partial a}, \quad \frac{\partial \psi_j}{\partial s} = \frac{\partial a}{\partial s}\frac{\partial \psi_j}{\partial a} + \frac{\partial b}{\partial s}\frac{\partial \psi_j}{\partial b}, \quad \frac{\partial \psi_j}{\partial t} = \frac{\partial a}{\partial t}\frac{\partial \psi_j}{\partial a} + \frac{\partial b}{\partial t}\frac{\partial \psi_j}{\partial b} + \frac{\partial c}{\partial t}\frac{\partial \psi_j}{\partial c}. \tag{3.72}$$

Defining the reference differentiation matrices

$$D_r = V_r V^{-1} \quad D_s = V_s V^{-1} \quad D_t = V_t V^{-1} \tag{3.73}$$

the corresponding reference stiffness matrices are given by

$$S_r = M D_r \quad S_s = M D_s \quad S_t = M D_t. \tag{3.74}$$

Finally the right-hand side of the scheme requires the computation of the surface integral

$$\int_{\partial \Omega_h^k} \hat{\boldsymbol{n}} \cdot \boldsymbol{g}_h l_i^k(\boldsymbol{x})\, d\Omega = \sum_{j=1}^{N_{fp}} \hat{\boldsymbol{n}} \cdot \boldsymbol{g}_j \int_{\partial \Omega_h^k} l_j^k(\boldsymbol{x}) l_i^k(\boldsymbol{x})\, d\Omega \tag{3.75}$$

where N_{fp} is the number of nodes on the faces of the element and $\boldsymbol{g}_h$ is the flux or jump in flux.

Fortunately, this refers to the mass matrix of the faces, specifically it is the mass matrix already developed in the two-dimensional case.

3.4 Curvilinear Elements

While the previous sections focused on discretizing the domain using straight-sided simplices (lines, triangles, tetrahedra), accurately representing domains with curved boundaries often necessitates the use of curvilinear elements.

These elements deform the standard straight-sided reference element I into a curved element Ω_h^k in the physical domain Ω_h. These are generated by a non-linear mapping $\boldsymbol{x} = \boldsymbol{\Psi}(\boldsymbol{r})$ from the reference element I to the physical element Ω_h^k. Often, this mapping $\boldsymbol{\Psi}$ is isoparametric, using the same high-order basis functions $l_i(\boldsymbol{r})$ as the solution approximation.

A key difference from straight-sided elements is that the Jacobian matrix of the transformation, $\mathbf{J}_{mn} = \partial x_m / \partial r_n$, and its determinant $|J| = \det(\mathbf{J})$ are no longer constant within the element; they are functions of the reference coordinates $\boldsymbol{r}$.

This spatial variation affects calculations involving derivatives, which transform using the inverse Jacobian $\mathbf{J}^{-1}$, and integrals, where the volume element transforms as $d\Omega = |J(\boldsymbol{r})|d\boldsymbol{r}$. Consequently, element matrices, such as the mass matrix

$$M_{ij}^{k} = \int_{I} l_i(\boldsymbol{r}) l_j(\boldsymbol{r}) |J(\boldsymbol{r})| \, d\boldsymbol{r}, \tag{3.76}$$

contain non-constant Jacobian terms within the integral.

Due to the presence of these spatially varying Jacobian terms, integrals required for constructing the discrete system cannot usually be computed analytically. Instead, they must be evaluated numerically, typically using Gauss quadrature rules or cubature rules defined on the reference element I. While increasing computational complexity, this approach allows for accurate geometric representation, crucial for many applications.

3.5 Handling Time Discretization

The choice of a time integration scheme is critical when solving time-dependent partial differential equations using the DGTD method. This scheme dictates how the solution evolves over time, directly impacting the fidelity and stability of the simulation. Its fundamental purpose is to discretize the continuous temporal domain into steps, allowing for a step-by-step approximation of how physical phenomena change over a given period. An appropriately chosen integrator ensures that the numerical solution remains stable and accurately reflects the true dynamics of the system, including how waves propagate and maintain their shape.

When selecting an integration scheme for DGTD simulations, a balance must be struck between several key factors:

- **Accuracy:** The scheme must ensure that the numerical approximation remains close to the true solution. This involves minimizing errors introduced by the temporal discretization, often measured by the formal order of accuracy.
- **Stability:** The numerical method must converge towards the expected behavior without spurious oscillations or divergence. The stability region of a scheme determines the maximum allowable time step size (Δt), particularly for explicit methods governed by conditions like the Courant-Friedrichs-Lewy (CFL) limit [5].
- **Computational Efficiency:** This refers to the effective use of computational resources (Central Processing Unit (CPU) time, memory per time step). An efficient scheme minimizes these costs while maintaining the desired levels of accuracy, stability, and wave fidelity. This includes factors like the number of stages or function evaluations per step and memory footprint (e.g., standard vs. low-storage schemes).

- **Dissipation and Dispersion:** These relate to how well the scheme preserves wave characteristics.
  - *Numerical Dissipation* refers to the tendency of a scheme to artificially dampen the amplitude of waves, particularly high-frequency components. While some dissipation can be beneficial for suppressing noise, excessive dissipation can remove physically important features.
  - *Numerical Dispersion* refers to phase errors, where waves of different frequencies propagate at incorrect speeds relative to each other. This can cause wave packets to spread out or distort unrealistically.

  Minimizing unwanted numerical dissipation and dispersion is crucial for simulations where accurate wave propagation over long durations is required.

Commonly employed integration schemes include the RK family and the leapfrog method. For DGTD applications, fourth-order RK (RK4) schemes are often favored over the second-order leapfrog scheme. While leapfrog is non-dissipative, its dispersive errors and stability properties can be less favorable compared to RK4, which generally offers a better balance of accuracy, stability, and manageable (though non-zero) dissipation and dispersion for many wave propagation problems.

Considering these factors, this work focuses on explicit RK methods for the temporal integration. We specifically address the semi-discrete problem arising after spatial discretization

$$\frac{\partial q_h(\boldsymbol{x}, t)}{\partial t} = L_h(q_h(\boldsymbol{x}, t), t) \tag{3.77}$$

where $q_h(\boldsymbol{x}, t)$ represents the spatially discretized solution vector, and L_h is the corresponding semi-discrete operator.

A well-known and widely used example is the classic explicit fourth-order, four-stage RK method, depicted in Algorithm 1. Its popularity stems from its simplicity and good balance between accuracy and computational effort for many problems.

Algorithm 1: Classic Runge-Kutta 4th Order Method (RK4)

Input: Initial condition $q_h(\mathbf{x}, t_0)$, time step Δt, number of steps N_{steps};

Output: Final solution $q_h(\mathbf{x}, t_{\text{final}})$;

Initialize $q \leftarrow q_h(\mathbf{x}, t_0)$;

for $n \leftarrow 1$ **to** N_{steps} **do**

  $t_n \leftarrow t_0 + n \cdot \Delta t$;

  Compute stage derivatives:;

  $k_1 \leftarrow L_h(q, t_n)$;

  $k_2 \leftarrow L_h(q + \frac{\Delta t}{2} k_1, t_n + \frac{\Delta t}{2})$;

  $k_3 \leftarrow L_h(q + \frac{\Delta t}{2} k_2, t_n + \frac{\Delta t}{2})$;

  $k_4 \leftarrow L_h(q + \Delta t k_3, t_n + \Delta t)$;

  Update solution for next step:;

  $q \leftarrow q + \frac{\Delta t}{6}(k_1 + 2k_2 + 2k_3 + k_4)$;

Return q;

However, a drawback of the standard RK4 algorithm (Algorithm 1) is its memory requirement, as it necessitates storing four stage derivatives (k_1 to k_4) or intermediate solutions simultaneously. For large-scale problems, this can be significant. A more memory-efficient alternative is the low-storage, fourth-order, five-stage RK method presented in Algorithm 2. Algorithm 2 [37]. This class of methods cleverly reuses intermediate results to achieve the desired order of accuracy with minimal storage overhead (typically requiring storage only for the solution vector q_h and one or two auxiliary vectors like p and k). The specific coefficients for one such popular scheme are listed in Table 5.

Algorithm 2: Low-Storage Runge-Kutta 4th Order Method (5 Stages)

Input: Initial condition $q_h(\mathbf{x}, t_0)$, time step Δt, number of steps N_{steps}, coefficients a_i, b_i, c_i (from Table 5);

Output: Final solution $q_h(\mathbf{x}, t_{\text{final}})$;

Initialize $q \leftarrow q_h(\mathbf{x}, t_0)$;

for $n \leftarrow 1$ **to** N_{steps} **do**

  $t_n \leftarrow t_0 + n \cdot \Delta t$;

  $p \leftarrow q$;

  $k \leftarrow 0$;

  Compute stages:;

  for $i \leftarrow 0$ **to** 4 **do**

    $k \leftarrow a_i \cdot k + \Delta t \cdot L_h(p, t_n + c_i \Delta t)$;

    $p \leftarrow p + b_i \cdot k$;

  Update solution:;

  $q \leftarrow p$;

Return q;

Table 5 – Coefficients for a low-storage Runge-Kutta 4th Order, 5 stage method

i	a_i	b_i	c_i
0	0	$\frac{1432997174477}{9575080441755}$	0
1	$-\frac{567301805773}{1357537059087}$	$\frac{5161836677717}{13612068292357}$	$\frac{1432997174477}{9575080441755}$
2	$-\frac{2404267990393}{2016746695238}$	$\frac{1720146321549}{2090206949498}$	$\frac{2526269341429}{6820363962896}$
3	$-\frac{3550918686646}{2091501179385}$	$\frac{3134564353537}{4481467310338}$	$\frac{2006345519317}{3224310063776}$
4	$-\frac{1275806237668}{842570457699}$	$\frac{2277821191437}{14882151754819}$	$\frac{2802321613138}{2924317926251}$

While the explicit RK methods discussed above are widely used due to their efficiency per time step, they are only conditionally stable, meaning the time step Δt must be kept below a certain threshold (dictated by the CFL condition for hyperbolic problems like those often solved with DGTD) to prevent instability. For problems where this stability constraint is overly restrictive (e.g., stiff problems or when very fine spatial meshes are used), implicit integration schemes offer an alternative. Implicit methods often possess better stability properties (sometimes

unconditional stability), potentially allowing for much larger time steps, but come at the cost of requiring the solution of a (potentially large and non-linear) system of equations at each stage or time step, as shown schematically in Algorithm 3. This makes the computational cost per step significantly higher than for explicit methods.

Algorithm 3: General Implicit Runge-Kutta Method

Input: Initial condition $q_h(\mathbf{x}, t_0)$, time step Δt, number of steps N_{steps}, Butcher tableau (A, b, c) for s-stage method;

Output: Final solution $q_h(\mathbf{x}, t_{\text{final}})$;

Initialize $q \leftarrow q_h(\mathbf{x}, t_0)$;

for $n \leftarrow 1$ **to** N_{steps} **do**

  $t_n \leftarrow t_0 + n \cdot \Delta t$;

  Solve coupled system:;

  for $i \leftarrow 1$ **to** s **do**

    Solve for K_i in:;

    $K_i = L_h\left(q + \Delta t \sum_{j=1}^{s} A_{ij} K_j,\ t_n + c_i \Delta t\right)$;

  Update solution:;

  $q \leftarrow q + \Delta t \sum_{i=1}^{s} b_i K_i$;

Return q;

A classic example of a high-order implicit scheme is the 2-stage 4th-order Gauss-Legendre method, whose coefficients are given in the Butcher tableau format in Table 6 [38]. Such methods are particularly useful for problems demanding high accuracy and strong stability properties, despite their higher computational cost per step.

Table 6 – Butcher tableau for the Gauss-Legendre 2-stage, 4th-order implicit method

$$\begin{array}{c|cc} c_1 & a_{11} & a_{12} \\ c_2 & a_{21} & a_{22} \\ \hline & b_1 & b_2 \end{array} \quad \rightarrow \quad \begin{array}{c|cc} \frac{1}{2} - \frac{\sqrt{3}}{6} & \frac{1}{4} & \frac{1}{4} - \frac{\sqrt{3}}{6} \\ \frac{1}{2} + \frac{\sqrt{3}}{6} & \frac{1}{4} + \frac{\sqrt{3}}{6} & \frac{1}{4} \\ \hline & \frac{1}{2} & \frac{1}{2} \end{array}$$

CHAPTER 4

Discontinuous Galerkin Time-Domain Method Applied to Electromagnetism

This chapter combines the DGTD from Chapter 3 with Maxwell's equations from Chapter 2, resulting in a powerful approach to solving complex problems in electromagnetism. It provides insights into the fundamental principles of electromagnetic fields and enables accurate and efficient solutions to real-world problems in this field. Additionally, several key concepts used to model electromagnetic problems will be discussed, shedding light on the methods and strategies necessary for accurate simulations and practical applications in electromagnetics.

4.1 The Discontinuous Galerkin Method

Maxwell's curl equations for lossless linear media without sources [8] are defined as

$$\bar{\bar{\mu}}(\boldsymbol{x})\frac{\partial \boldsymbol{\mathcal{H}}(\boldsymbol{x},t)}{\partial t} = -\nabla \times \boldsymbol{\mathcal{E}}(\boldsymbol{x},t), \tag{4.1}$$

$$\bar{\bar{\epsilon}}(\boldsymbol{x})\frac{\partial \boldsymbol{\mathcal{E}}(\boldsymbol{x},t)}{\partial t} = \quad \nabla \times \boldsymbol{\mathcal{H}}(\boldsymbol{x},t), \tag{4.2}$$

where $\boldsymbol{\mathcal{E}}$ and $\boldsymbol{\mathcal{H}}$ are the electric and magnetic fields in the time domain, respectively. Moreover, $\bar{\bar{\epsilon}}$ and $\bar{\bar{\mu}}$ are the electric permittivity and the magnetic permeability tensors, respectively. Furthermore, $\boldsymbol{x}$ and t indicate the spatial position and time, respectively.

In conservation form the aforementioned equations become [39] (derived in Appendix A.1)

$$Q(\boldsymbol{x})\frac{\partial \vec{q}(\boldsymbol{x},t)}{\partial t} + \nabla \cdot \vec{\boldsymbol{\mathcal{F}}}(\vec{q},\boldsymbol{x},t) = 0, \tag{4.3}$$

where

$$\vec{q}(\boldsymbol{x},t) = \begin{bmatrix} \boldsymbol{\mathcal{H}}(\boldsymbol{x},t) \\ \boldsymbol{\mathcal{E}}(\boldsymbol{x},t) \end{bmatrix}, \qquad Q(\boldsymbol{x},t) = \begin{bmatrix} \bar{\bar{\mu}}(\boldsymbol{x},t) & 0 \\ 0 & \bar{\bar{\epsilon}}(\boldsymbol{x},t) \end{bmatrix},$$

$$\vec{\boldsymbol{\mathcal{F}}}(\vec{q}) = \left[\vec{\mathcal{F}}_1, \vec{\mathcal{F}}_2, \vec{\mathcal{F}}_3\right]^\intercal, \qquad \vec{\mathcal{F}}_i(\vec{q}) = \begin{bmatrix} \boldsymbol{e}_i \times \boldsymbol{\mathcal{E}}(\boldsymbol{x},t) \\ -\boldsymbol{e}_i \times \boldsymbol{\mathcal{H}}(\boldsymbol{x},t) \end{bmatrix},$$

with $\vec{\boldsymbol{\mathcal{F}}}$ being the flux and $\boldsymbol{e}_i$ representing the three Cartesian unit vectors ($i = 1, 2, 3$). It is important to note that the symbol $\boldsymbol{\mathcal{F}}$ represents the Cartesian vector $[\mathcal{F}_x, \mathcal{F}_y, \mathcal{F}_z]^\intercal$ while $\vec{\mathcal{F}}$ represents a general vector $[\mathcal{F}_1, \mathcal{F}_2, \mathcal{F}_3, \mathcal{F}_4, \ldots]^\intercal$. Therefore, $\nabla \cdot \vec{\boldsymbol{\mathcal{F}}} = \partial\vec{\mathcal{F}}_x/\partial x + \partial\vec{F}_y/\partial y + \partial\vec{F}_z/\partial z$ has the same shape as $\vec{\mathcal{F}}_x$, $\vec{\mathcal{F}}_y$ and $\vec{\mathcal{F}}_z$.

Although the previous set of equations can be applied to anisotropic materials using the tensor notation, the focus of the formulation herein will be on isotropic materials for simplicity. This simplification is made by assuming scalar values for the permittivity ϵ and permeability μ.

The following section briefly applies the general framework presented in Section 3.2 to the specific case of Equation (4.3).

4.1.1 The Galerkin Method

Assuming that Ω_h is a tessellated finite region (bounded by $\partial\Omega_h$) of the physical domain Ω with K non-overlapping elements (Ω_h^k, bounded by $\partial\Omega_h^k$) where Equation (4.3) is solved. Thus

$$\Omega \approx \Omega_h = \bigcup_k^K \Omega_h^k. \tag{4.4}$$

Introducing a globally defined vector space $\mathcal{V}_h$ to approximate $\vec{q}(\boldsymbol{x},t)$ given that $\mathcal{V}_h = \oplus_{k=1}^K \mathcal{V}_h^k$ where the locally defined vector spaces are defined as $\mathcal{V}_h^k = \text{span}\left\{\psi_n(\Omega_h^k)\right\}_{n=1}^{N_p}$. Considering that $\mathcal{V}_h$ is piecewise smooth over Ω_h, a local approximation $\vec{q}_h^k(\boldsymbol{x},t)$ defined in the local vector space $\mathcal{V}_h$ is [6]

$$\vec{q}_h^k(\boldsymbol{x},t) = \sum_{n=1}^{N_p} \hat{\vec{q}}_n^k(t) \cdot \psi_n(\boldsymbol{x}) = \sum_{i=1}^{N_p} \tilde{\vec{q}}_h^k(\boldsymbol{x}_i,t) \cdot l_i(\boldsymbol{x}) \quad \boldsymbol{x} \in \Omega^k, \tag{4.5}$$

where l_i are the interpolating Lagrange nodal basis functions which possess the Kronecker delta property [40]. The relation between modal coefficients $\hat{\vec{q}}_n^k(t)$ and nodal coefficients $\tilde{\vec{q}}_h^k(\boldsymbol{x}_i,t)$ is given by the Vandermonde matrix [6]. The modal basis functions are usually chosen to be normalized monomials, while the interpolating positions $\boldsymbol{x}_i$ are spread in a Gauss-Lobatto alike distribution, usually obtained by the Warp&Blend method [6].

By applying the Galerkin testing and integration by parts over Equation (4.3) locally for each element, the strong variational formulation of Maxwell's curl equations [40] can be derived as

$$\int_{\Omega_h^k} \left[Q\frac{\partial \vec{q}_h^k}{\partial t} + \nabla \cdot \vec{\boldsymbol{\mathcal{F}}}_h^k(\vec{q}_h^k) \right] \cdot l_i(\boldsymbol{x})\, d\Omega = \int_{\partial\Omega_h^k} \hat{\boldsymbol{n}} \cdot \left[\vec{\boldsymbol{\mathcal{F}}}_h^k(\vec{q}_h^k) - \vec{\boldsymbol{\mathcal{F}}}^*(\vec{q}_h^k) \right] \cdot l_i(\boldsymbol{x})\, d\Omega \quad \forall l_i \in \mathcal{V}_h^k, \tag{4.6}$$

where $\hat{\boldsymbol{n}}$ is the outward unit vector normal to the boundary surface $\partial\Omega_h^k$ and $\mathcal{F}_h^k - \mathcal{F}^*$ are termed as the numerical flux difference used for information exchange.

Within each element, the physical fields $\boldsymbol{\mathcal{E}}(\boldsymbol{x},t)$ and $\boldsymbol{\mathcal{H}}(\boldsymbol{x},t)$ are approximated by $\boldsymbol{\mathcal{E}}_h^k(\boldsymbol{x},t)$ and $\boldsymbol{\mathcal{H}}_h^k(\boldsymbol{x},t)$ using nodal basis functions as

$$\boldsymbol{\mathcal{E}}_h^k(\boldsymbol{x},t) = \sum_{i=1}^{N_p} \tilde{\boldsymbol{e}}_h^k(\boldsymbol{x}_i,t)\cdot l_i(\boldsymbol{x}) \qquad \boldsymbol{x}\in\Omega_h^k, \tag{4.7}$$

$$\boldsymbol{\mathcal{H}}_h^k(\boldsymbol{x},t) = \sum_{i=1}^{N_p} \tilde{\boldsymbol{h}}_h^k(\boldsymbol{x}_i,t)\cdot l_i(\boldsymbol{x}) \qquad \boldsymbol{x}\in\Omega_h^k, \tag{4.8}$$

where $\tilde{\boldsymbol{e}}$ and $\tilde{\boldsymbol{h}}$ are the nodal coefficients.

After replacing Equations (4.7) and (4.8) into Equation (4.6), assuming that Q in Equation (4.3) is constant within each element for simplicity, the occurring integrals simplify to

$$M_{ij}^k = \int_{\Omega_h^k} l_i(\boldsymbol{x})\cdot l_j(\boldsymbol{x})\,d\Omega, \tag{4.9}$$

$$S_{ij,s}^k = \int_{\Omega_h^k} l_i(\boldsymbol{x})\cdot \frac{\partial l_j(\boldsymbol{x})}{\partial s}\,d\Omega \quad s=x,y,z, \tag{4.10}$$

$$F_{ij,f}^k = \int_{\partial\Omega_h^k} l_i(\boldsymbol{x})\cdot l_j(\boldsymbol{x})\,d\Omega. \tag{4.11}$$

where M^k is the mass matrix, S_s^k is the stiffness matrix along the s component and F_f^k is the face mass matrix for face f. Isolating the time derivatives one obtains

$$\epsilon^k \frac{\partial \tilde{\boldsymbol{e}}^k}{\partial t} = \left(M^k\right)^{-1}\cdot\left[\ \boldsymbol{S}^k\times\tilde{\boldsymbol{h}}^k + \sum_f F_f^k\cdot\left(\hat{n}\cdot\left[\mathcal{F}_E^k - \mathcal{F}_E^*\right]\right)\right], \tag{4.12}$$

$$\mu^k \frac{\partial \tilde{\boldsymbol{h}}^k}{\partial t} = \left(M^k\right)^{-1}\cdot\left[-\boldsymbol{S^k}\times\tilde{\boldsymbol{e}}^k + \sum_f F_f^k\cdot\left(\hat{n}\cdot\left[\mathcal{F}_H^k - \mathcal{F}_H^*\right]\right)\right], \tag{4.13}$$

where $\boldsymbol{S}^k = \left[S_x^k, S_y^k, S_z^k\right]^\intercal$, and $\mathcal{F}_E$ and $\mathcal{F}_H$ are the fluxes related to the electric and magnetic field, respectively.

4.1.2 Numerical Flux

Analyzing the simplest differential equation in conservation form allows for a better understanding of the numerical flux. Specifically, examining the one-dimensional advection equation

$$\frac{\partial u(x,t)}{\partial t} + \lambda\frac{\partial u(x,t)}{\partial x} = 0, \tag{4.14}$$

where λ is its eigenvalue and $\lambda u(x,t)$ is the flux.

The solution can be described as a waveform represented by the function $u(x,0)$, which propagates with a velocity of magnitude $|\lambda|$. If λ is positive, the waveform moves towards the right, while if λ is negative, it moves towards the left.

Examining the discontinuous function with $u^+ > u^-$ given by

$$u(x,0) = u^+ h(x - x_0) - u^- h(x - x_0), \tag{4.15}$$

where $h(x)$ is the Heaviside step function generally defined as

$$h(x) = \begin{cases} 0 & \text{if } x < 0 \\ 1 & \text{if } x > 0 \end{cases}, \tag{4.16}$$

considering two infinite elements defined by the regions $(-\infty, x_0]$ and $[x_0, -\infty)$, the challenge arises when attempting to calculate the flux at the discontinuity point x_0 depicted in Figure 4. It is not clear whether the value to be used should be u^+, u^-, or a combination of both. In this context, the numerical flux λu^* is defined, assuming that u^* represents the value at the discontinuity which may depend on both u^+ and u^-.

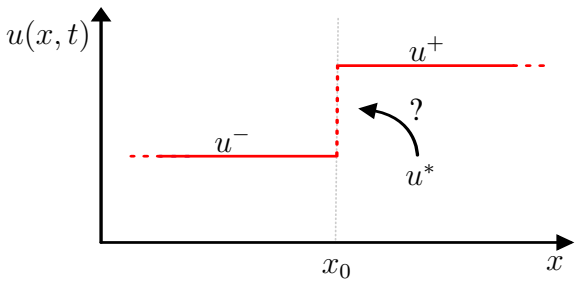

Figure 4 – Analysis of an advection function.

The determination of the numerical flux λu^* is primarily influenced by the dynamics of the partial differential equation under consideration. In the case of advection seen in Figure 5, considering $\lambda > 0$, it is observed that after an infinitesimal time step Δt, the waveform shifts towards the right. Thus, selecting $u^* = u^-$ would correspond to an upwind scheme, whereas $u^* = (u^- + u^+)/2$ would indicate a central scheme.

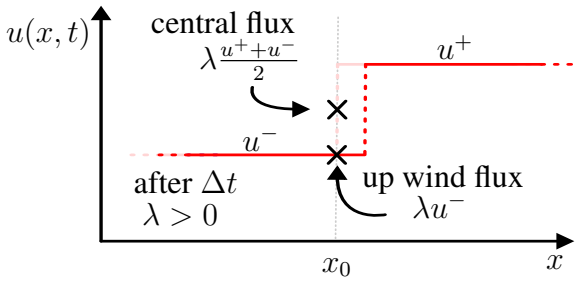

Figure 5 – Analysis of an advection function after Δt.

Hence, the numerical flux corresponds to the uniquely determined flux at the point of discontinuity. In this particular case, λu^* is leaving the region $(-\infty, x_0]$ and entering $[x_0, +\infty)$ given that $\lambda > 0$ and $u^+ > u^-$.

Other multidimensional problems can use the generalization of this approach since a system of Partial Differential Equations (PDEs) can be expanded into a set of first order Ordinary Differential Equations (ODEs) through diagonalization, which results in solving multiple Riemann problems analytically or numerically.

In the case of the Maxwell's equations with constant permittivity and permeability inside each element, the numerical flux for the linear case can be derived analytically by solving a Riemann's problem with Rankine-Hugoniot jump conditions [6] along a normal $\hat{\boldsymbol{n}}$. The mathematical development of the flux difference is shown in Appendix A.2 for the one-dimensional case. Therefore, the numerical flux difference for the three-dimensional case is [6]

$$\hat{\boldsymbol{n}} \cdot [\vec{\boldsymbol{\mathcal{F}}} - \vec{\boldsymbol{\mathcal{F}}}^*] = \hat{\boldsymbol{n}} \cdot \begin{bmatrix} \vec{\boldsymbol{\mathcal{F}}}_H - \vec{\boldsymbol{\mathcal{F}}}^*_H \\ \vec{\boldsymbol{\mathcal{F}}}_E - \vec{\boldsymbol{\mathcal{F}}}^*_{\boldsymbol{E}} \end{bmatrix} = \begin{bmatrix} \dfrac{1}{\{\{Y\}\}} \dfrac{\hat{\boldsymbol{n}} \times (Y^+[\boldsymbol{E}] + \alpha \hat{\boldsymbol{n}} \times [\boldsymbol{H}])}{2} \\ -\dfrac{1}{\{\{Z\}\}} \dfrac{\hat{\boldsymbol{n}} \times (Z^+[\boldsymbol{H}] + \alpha \hat{\boldsymbol{n}} \times [\boldsymbol{E}])}{2} \end{bmatrix}, \tag{4.17}$$

where

$$[\boldsymbol{u}] = \boldsymbol{u}^- - \boldsymbol{u}^+, \tag{4.18a}$$

$$\{\{\boldsymbol{u}\}\} = \frac{\boldsymbol{u}^- + \boldsymbol{u}^+}{2}, \tag{4.18b}$$

$$[\![\boldsymbol{u}]\!] = \hat{\boldsymbol{n}}^- \boldsymbol{u}^- + \hat{\boldsymbol{n}}^+ \boldsymbol{u}^+, \tag{4.18c}$$

$$Z^\pm = \frac{1}{Y^\pm} = \sqrt{\frac{\mu^\pm}{\epsilon^\pm}}. \tag{4.18d}$$

In this notation, "$-$" represents the local element while "$+$" represents the neighboring element, as shown in Figure 6. The upwind parameter $\alpha \in [0, 1]$ ensures that the scheme is stable and convergent. Setting $\alpha = 1$ represents the pure upwind flux, whereas the central flux can be recovered with $\alpha = 0$.

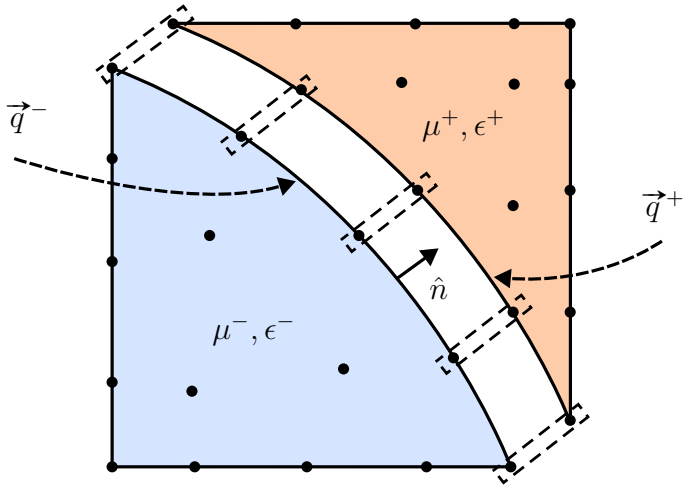

Figure 6 – Notation used for the definition of numerical fluxes. The blue element color represents the local element while the orange color represents a neighboring element.

4.2 Boundary Conditions

In computational electromagnetics, boundary conditions are fundamental for truncating finite domains while ensuring physical fidelity and numerical stability. Idealized reflective boundaries include Perfect Electric Conductors (PECs) and Perfect Magnetic Conductors (PMCs), which enforce strict electromagnetic constraints: PEC boundaries nullify the tangential electric field ($\hat{\boldsymbol{n}} \times \boldsymbol{\mathcal{E}} = 0$) and the normal magnetic flux density ($\hat{\boldsymbol{n}} \cdot \boldsymbol{\mathcal{B}} = 0$), modeling perfectly conductive surfaces. Conversely, PMC boundaries impose $\hat{\boldsymbol{n}} \times \boldsymbol{\mathcal{H}} = 0$ on the tangential magnetic field and $\hat{\boldsymbol{n}} \cdot \boldsymbol{\mathcal{D}} = 0$ on the normal electric flux density, serving as idealized magnetic interfaces. While these conditions are effective for enforcing symmetries or modeling conductors, their total reflectivity makes them unsuitable for open-region problems where outgoing waves must propagate indefinitely. To address this, ABCs like the Silver-Müller formulation approximate an unbounded domain by partially absorbing outgoing radiation. The Silver-Müller ABC link the tangential electric and magnetic fields through the medium's impedance Z as

$$\hat{\boldsymbol{n}} \times \boldsymbol{\mathcal{E}} = \quad Z\boldsymbol{\mathcal{H}}, \tag{4.19}$$

$$\hat{\boldsymbol{n}} \times \boldsymbol{\mathcal{H}} = -\frac{1}{Z}\boldsymbol{\mathcal{E}}, \tag{4.20}$$

where $\hat{\boldsymbol{n}}$ is the outward boundary normal. These conditions ensure that outgoing waves are absorbed with minimal reflection for normally incident radiation. Though imperfect for oblique incidence compared to advanced methods like PMLs, the Silver-Müller ABC balances simplicity and absorption efficiency, mitigating spurious resonances in wave propagation and scattering problems.

To incorporate boundary conditions into the DGTD method, the concept of *virtual elements* is employed as an abstraction. Virtual elements are not physically present in the computational domain but are conceptually introduced to represent the exterior side of the boundary. These elements are defined to match the material properties of the adjacent physical elements, i.e., $Y^- = Y^+$ and $Z^- = Z^+$. In the DGTD framework, boundary conditions are inherently imposed through the numerical flux, and virtual elements provide a consistent way to calculate the flux jumps at boundaries as if the exterior region were explicitly represented. This abstraction ensures that reflective conditions (PEC or PMC) or ABCs (e.g., Silver-Müller) are naturally embedded into the flux formulation. Since the flux is the only mechanism through which boundary conditions can be enforced in DGTD, virtual elements are not merely a simplification but a fundamental requirement for correctly handling wave interactions at domain boundaries.

The treatment of a PEC boundary involves enforcing the condition $\hat{\boldsymbol{n}} \times \boldsymbol{\mathcal{E}}^* = 0$, where $\boldsymbol{\mathcal{E}}^*$ is the numerical electric field at the boundary. Focusing on the magnetic part of the numerical flux from Equation (4.17), the expression can be rewritten as

$$\hat{\boldsymbol{n}} \cdot \left(\vec{\boldsymbol{\mathcal{F}}}_H - \vec{\boldsymbol{\mathcal{F}}}^*_H\right) = \hat{\boldsymbol{n}} \times \left(\boldsymbol{\mathcal{E}}^- - \boldsymbol{\mathcal{E}}^*\right) = \frac{\hat{\boldsymbol{n}} \times Y^+[\boldsymbol{\mathcal{E}}]}{2\{\{Y\}\}} + \frac{\hat{\boldsymbol{n}} \times \alpha\hat{\boldsymbol{n}} \times [\boldsymbol{\mathcal{H}}]}{2\{\{Y\}\}}. \tag{4.21}$$

Here, $[\boldsymbol{\mathcal{E}}] = \boldsymbol{\mathcal{E}}^- - \boldsymbol{\mathcal{E}}^+$ and $[\boldsymbol{\mathcal{H}}] = \boldsymbol{\mathcal{H}}^- - \boldsymbol{\mathcal{H}}^+$ represent the jumps in the electric and magnetic fields across the boundary, respectively. The terms $\{\{Y\}\}$ and α denote the average admittance and the flux parameter which control the flux behavior, respectively.

To enforce the PEC condition, $[\boldsymbol{\mathcal{H}}] = 0$ is imposed. Since the material properties of the physical element and the virtual element are considered to be identical ($Y^- = Y^+$), the flux expression simplifies to

$$\hat{\boldsymbol{n}} \times \left(\boldsymbol{\mathcal{E}}^- - \boldsymbol{\mathcal{E}}^*\right) = \frac{\hat{\boldsymbol{n}} \times [\boldsymbol{\mathcal{E}}]}{2}. \tag{4.22}$$

Enforcing $\hat{\boldsymbol{n}} \times \boldsymbol{\mathcal{E}}^* = 0$ at the boundary implies that the jump in the electric field satisfies $[\boldsymbol{\mathcal{E}}] = 2\boldsymbol{\mathcal{E}}^-$. This result can also be interpreted from the perspective of the central flux: setting $[\boldsymbol{\mathcal{H}}] = 0$ is equivalent to choosing $\alpha = 0$, which corresponds to the central flux. The central flux defines the numerical field $\boldsymbol{\mathcal{E}}^*$ as the average of the neighboring elements' values, i.e., $\boldsymbol{\mathcal{E}}^* = \frac{1}{2}(\boldsymbol{\mathcal{E}}^- + \boldsymbol{\mathcal{E}}^+)$. For $\boldsymbol{\mathcal{E}}^* = 0$, this implies $\boldsymbol{\mathcal{E}}^+ = -\boldsymbol{\mathcal{E}}^-$, leading to $[\boldsymbol{\mathcal{E}}] = \boldsymbol{\mathcal{E}}^- - \boldsymbol{\mathcal{E}}^+ = 2\boldsymbol{\mathcal{E}}^-$.

A similar procedure applies to the PMC boundary condition. In this case, the electric part of the flux is modified to ensure $\hat{\boldsymbol{n}} \times \boldsymbol{\mathcal{H}}^* = 0$. By duality with the PEC case, this leads to $[\boldsymbol{\mathcal{E}}] = 0$ and $[\boldsymbol{\mathcal{H}}] = 2\boldsymbol{\mathcal{H}}^-$, ensuring the correct behavior for the magnetic field at the boundary.

For the Silver-Müller boundary condition, the goal is to absorb outgoing waves as if they were propagating as plane waves normal to the interface. This requires enforcing the impedance conditions $\hat{\boldsymbol{n}} \times \boldsymbol{\mathcal{E}} = Z\boldsymbol{\mathcal{H}}$ or $\hat{\boldsymbol{n}} \times \boldsymbol{\mathcal{H}} = -Y\boldsymbol{\mathcal{E}}$. To achieve this, the jump terms in the flux are modified such that $[\boldsymbol{\mathcal{E}}] = \boldsymbol{\mathcal{E}}^-$ and $[\boldsymbol{\mathcal{H}}] = \boldsymbol{\mathcal{H}}^-$ [41]. This ensures that the numerical flux mimics the behavior of an ABC, allowing outgoing waves to propagate without significant reflections.

All these common boundary conditions that are naturally imposed [40] directly into Equation (4.17) are summarized in Table 7.

Table 7 – Field differences for commonly used boundary conditions

Boundary Condition	$[\boldsymbol{\mathcal{E}}]$	$[\boldsymbol{\mathcal{H}}]$
Perfect Electric Conductor (PEC)	$2\boldsymbol{\mathcal{E}}^-$	0
Perfect Magnetic Conductor (PMC)	0	$2\boldsymbol{\mathcal{H}}^-$
First Order Absorbing (Silver-Müller)	$\boldsymbol{\mathcal{E}}^-$	$\boldsymbol{\mathcal{H}}^-$

4.3 Perfect Matched Layers

PMLs have many advantages over ABCs including being independent of frequency, wave polarization, and angle of incidence. The general time-harmonic Maxwell's equations within the frequency domain in the uniaxial PML medium [36] are given by

$$\nabla \times \boldsymbol{H}(\boldsymbol{x}, \omega) = \quad j\omega\bar{\bar{\Lambda}}_e \epsilon \boldsymbol{E}(\boldsymbol{x}, \omega), \tag{4.23}$$

$$\nabla \times \boldsymbol{E}(\boldsymbol{x},\omega) = -j\omega\bar{\bar{\Lambda}}_m \mu \boldsymbol{H}(\boldsymbol{x},\omega), \tag{4.24}$$

where

$$\bar{\bar{\Lambda}}_e \equiv \begin{bmatrix} \frac{s_{y,e}s_{z,e}}{s_{x,e}} & 0 & 0 \\ 0 & \frac{s_{x,e}s_{z,e}}{s_{y,e}} & 0 \\ 0 & 0 & \frac{s_{x,e}s_{y,e}}{s_{z,e}} \end{bmatrix}, \quad \bar{\bar{\Lambda}}_m \equiv \begin{bmatrix} \frac{s_{y,m}s_{z,m}}{s_{x,m}} & 0 & 0 \\ 0 & \frac{s_{x,m}s_{z,m}}{s_{y,m}} & 0 \\ 0 & 0 & \frac{s_{x,m}s_{y,m}}{s_{z,m}} \end{bmatrix}, \tag{4.25}$$

given that the uniaxial PML parameters for $i = x, y, z$ are

$$s_{i,e} = k_i + \frac{\sigma_{i,e}}{j\omega\epsilon_0}, \quad s_{i,m} = k_i + \frac{\sigma_{i,m}}{j\omega\mu_0}, \tag{4.26}$$

where the ratio $\sigma_e/\epsilon_0 = \sigma_m/\mu_0$ must be enforced.

Directly implementing Equations (4.23) and (4.24) leads to a convolution between the tensor coefficients and the electromagnetic fields which is computationally intensive. A better approach is to define constitutive relationships to decouple the frequency terms, specifically

$$\boldsymbol{D}(\boldsymbol{x},\omega) = \bar{\bar{s}}_e \epsilon \boldsymbol{E}(\boldsymbol{x},\omega), \tag{4.27}$$

$$\boldsymbol{B}(\boldsymbol{x},\omega) = \bar{\bar{s}}_m \mu \boldsymbol{H}(\boldsymbol{x},\omega), \tag{4.28}$$

with

$$\bar{\bar{s}}_e \equiv \begin{bmatrix} \frac{s_{z,e}}{s_{x,e}} & 0 & 0 \\ 0 & \frac{s_{x,e}}{s_{y,e}} & 0 \\ 0 & 0 & \frac{s_{y,e}}{s_{z,e}} \end{bmatrix} \quad \bar{\bar{s}}_m \equiv \begin{bmatrix} \frac{s_{z,m}}{s_{x,m}} & 0 & 0 \\ 0 & \frac{s_{x,m}}{s_{y,m}} & 0 \\ 0 & 0 & \frac{s_{y,m}}{s_{z,m}} \end{bmatrix}. \tag{4.29}$$

To simplify the notation, the e index will be omitted when considering electric variables. Starting by replacing Equation (4.25) into Equation (4.23) and expanding the components leads to

$$\begin{bmatrix} \frac{\partial H_z(\boldsymbol{x},\omega)}{\partial y} - \frac{\partial H_y(\boldsymbol{x},\omega)}{\partial z} \\ \frac{\partial H_x(\boldsymbol{x},\omega)}{\partial z} - \frac{\partial H_z(\boldsymbol{x},\omega)}{\partial x} \\ \frac{\partial H_y(\boldsymbol{x},\omega)}{\partial x} - \frac{\partial H_x(\boldsymbol{x},\omega)}{\partial y} \end{bmatrix} = j\omega \begin{bmatrix} s_x^{-1}s_y s_z & 0 & 0 \\ 0 & s_y^{-1}s_z s_x & 0 \\ 0 & 0 & s_z^{-1}s_x s_y \end{bmatrix} \epsilon \begin{bmatrix} E_x(\boldsymbol{x},\omega) \\ E_y(\boldsymbol{x},\omega) \\ E_z(\boldsymbol{x},\omega) \end{bmatrix}. \tag{4.30}$$

Replacing Equation (4.29) into Equation (4.27) gives

$$\begin{bmatrix} D_x(\boldsymbol{x},\omega) \\ D_y(\boldsymbol{x},\omega) \\ D_z(\boldsymbol{x},\omega) \end{bmatrix} = \begin{bmatrix} \frac{s_z}{s_x} & 0 & 0 \\ 0 & \frac{s_x}{s_y} & 0 \\ 0 & 0 & \frac{s_y}{s_z} \end{bmatrix} \epsilon \begin{bmatrix} E_x(\boldsymbol{x},\omega) \\ E_y(\boldsymbol{x},\omega) \\ E_z(\boldsymbol{x},\omega) \end{bmatrix}. \tag{4.31}$$

Therefore, combining Equations (4.30) and (4.31) leads to the intermediate stage

$$\begin{bmatrix} \dfrac{\partial H_z(\boldsymbol{x},\omega)}{\partial y} - \dfrac{\partial H_y(\boldsymbol{x},\omega)}{\partial z} \\ \dfrac{\partial H_x(\boldsymbol{x},\omega)}{\partial z} - \dfrac{\partial H_z(\boldsymbol{x},\omega)}{\partial x} \\ \dfrac{\partial H_y(\boldsymbol{x},\omega)}{\partial x} - \dfrac{\partial H_x(\boldsymbol{x},\omega)}{\partial y} \end{bmatrix} = j\omega \begin{bmatrix} s_y & 0 & 0 \\ 0 & s_z & 0 \\ 0 & 0 & s_x \end{bmatrix} \begin{bmatrix} D_x(\boldsymbol{x},\omega) \\ D_y(\boldsymbol{x},\omega) \\ D_z(\boldsymbol{x},\omega) \end{bmatrix}, \tag{4.32}$$

which can be easily transformed back to the time domain through the inverse Fourier transform, resulting in the following set of equations

$$\frac{\partial \mathcal{H}_z(\boldsymbol{x},t)}{\partial y} - \frac{\partial \mathcal{H}_y(\boldsymbol{x},t)}{\partial z} = \kappa_y \frac{\partial \mathcal{D}_x(\boldsymbol{x},t)}{\partial t} + \frac{\sigma_y}{\epsilon_0}\mathcal{D}_x(\boldsymbol{x},t), \tag{4.33}$$

$$\frac{\partial \mathcal{H}_x(\boldsymbol{x},t)}{\partial z} - \frac{\partial \mathcal{H}_z(\boldsymbol{x},t)}{\partial x} = \kappa_z \frac{\partial \mathcal{D}_y(\boldsymbol{x},t)}{\partial t} + \frac{\sigma_z}{\epsilon_0}\mathcal{D}_y(\boldsymbol{x},t), \tag{4.34}$$

$$\frac{\partial \mathcal{H}_y(\boldsymbol{x},t)}{\partial x} - \frac{\partial \mathcal{H}_x(\boldsymbol{x},t)}{\partial y} = \kappa_x \frac{\partial \mathcal{D}_z(\boldsymbol{x},t)}{\partial t} + \frac{\sigma_x}{\epsilon_0}\mathcal{D}_z(\boldsymbol{x},t), \tag{4.35}$$

while the electric auxiliary equations are also transformed to the time domain leading to

$$\kappa_x \frac{\partial \mathcal{D}_x(\boldsymbol{x},t)}{\partial t} + \frac{\sigma_x}{\epsilon_0}\mathcal{D}_x(\boldsymbol{x},t) = \epsilon \left[\kappa_z \frac{\partial \mathcal{E}_x(\boldsymbol{x},t)}{\partial t} + \frac{\sigma_z}{\epsilon_0}\mathcal{E}_x(\boldsymbol{x},t) \right], \tag{4.36}$$

$$\kappa_y \frac{\partial \mathcal{D}_y(\boldsymbol{x},t)}{\partial t} + \frac{\sigma_y}{\epsilon_0}\mathcal{D}_y(\boldsymbol{x},t) = \epsilon \left[\kappa_x \frac{\partial \mathcal{E}_y(\boldsymbol{x},t)}{\partial t} + \frac{\sigma_x}{\epsilon_0}\mathcal{E}_y(\boldsymbol{x},t) \right], \tag{4.37}$$

$$\kappa_z \frac{\partial \mathcal{D}_z(\boldsymbol{x},t)}{\partial t} + \frac{\sigma_z}{\epsilon_0}\mathcal{D}_z(\boldsymbol{x},t) = \epsilon \left[\kappa_y \frac{\partial \mathcal{E}_z(\boldsymbol{x},t)}{\partial t} + \frac{\sigma_y}{\epsilon_0}\mathcal{E}_z(\boldsymbol{x},t) \right]. \tag{4.38}$$

Applying the same procedure to Equations (4.24) and (4.28), results in

$$-\frac{\partial \mathcal{E}_z(\boldsymbol{x},t)}{\partial y} + \frac{\partial \mathcal{E}_y(\boldsymbol{x},t)}{\partial z} = \kappa_y \frac{\partial \mathcal{B}_x(\boldsymbol{x},t)}{\partial t} + \frac{\sigma_{m,y}}{\mu_0}\mathcal{B}_x(\boldsymbol{x},t), \tag{4.39}$$

$$-\frac{\partial \mathcal{E}_x(\boldsymbol{x},t)}{\partial z} + \frac{\partial \mathcal{E}_z(\boldsymbol{x},t)}{\partial x} = \kappa_z \frac{\partial \mathcal{B}_y(\boldsymbol{x},t)}{\partial t} + \frac{\sigma_{m,z}}{\mu_0}\mathcal{B}_y(\boldsymbol{x},t), \tag{4.40}$$

$$-\frac{\partial \mathcal{E}_y(\boldsymbol{x},t)}{\partial x} + \frac{\partial \mathcal{E}_x(\boldsymbol{x},t)}{\partial y} = \kappa_x \frac{\partial \mathcal{B}_z(\boldsymbol{x},t)}{\partial t} + \frac{\sigma_{m,x}}{\mu_0}\mathcal{B}_z(\boldsymbol{x},t), \tag{4.41}$$

and likewise, the magnetic auxiliary equations are given by

$$\kappa_x \frac{\partial \mathcal{B}_x(\boldsymbol{x},t)}{\partial t} + \frac{\sigma_{m,x}}{\mu_0}\mathcal{B}_x(\boldsymbol{x},t) = \mu \left[\kappa_z \frac{\partial \mathcal{H}_x(\boldsymbol{x},t)}{\partial t} + \frac{\sigma_{m,z}}{\mu_0}\mathcal{H}_x(\boldsymbol{x},t) \right], \tag{4.42}$$

$$\kappa_y \frac{\partial \mathcal{B}_y(\boldsymbol{x},t)}{\partial t} + \frac{\sigma_{m,y}}{\mu_0}\mathcal{B}_y(\boldsymbol{x},t) = \mu \left[\kappa_x \frac{\partial \mathcal{H}_y(\boldsymbol{x},t)}{\partial t} + \frac{\sigma_{m,x}}{\mu_0}\mathcal{H}_y(\boldsymbol{x},t) \right], \tag{4.43}$$

$$\kappa_z \frac{\partial \mathcal{B}_z(\boldsymbol{x},t)}{\partial t} + \frac{\sigma_{m,z}}{\mu_0}\mathcal{B}_z(\boldsymbol{x},t) = \mu \left[\kappa_y \frac{\partial \mathcal{H}_z(\boldsymbol{x},t)}{\partial t} + \frac{\sigma_{m,y}}{\mu_0}\mathcal{H}_z(\boldsymbol{x},t) \right]. \tag{4.44}$$

To summarize, the direct solution of Equations (4.23) and (4.24) leads to a convolution integral in the time domain. However, this can be avoided by employing two ADEs: Equations (4.27) and (4.28). Therefore, instead of calculating the next step of $\boldsymbol{\mathcal{E}}(\boldsymbol{x},t)$ directly from $\boldsymbol{\mathcal{H}}(\boldsymbol{x},t)$, now the next step of $\boldsymbol{\mathcal{E}}(\boldsymbol{x},t)$ is calculated from $\boldsymbol{\mathcal{D}}(\boldsymbol{x},t)$ which is calculated from $\boldsymbol{\mathcal{H}}(\boldsymbol{x},t)$ as seen in Equations (4.33) to (4.35) and Equations (4.36) to (4.38), respectively. The same happens for the next step of the magnetic field $\boldsymbol{\mathcal{H}}(\boldsymbol{x},t)$ that could be calculated from $\boldsymbol{\mathcal{E}}(\boldsymbol{x},t)$, now the next step of $\boldsymbol{\mathcal{H}}(\boldsymbol{x},t)$ is calculated from $\boldsymbol{\mathcal{B}}(\boldsymbol{x},t)$ which is calculated from $\boldsymbol{\mathcal{E}}(\boldsymbol{x},t)$ as seen in Equations (4.39) to (4.41) and Equations (4.42) to (4.44), respectively. Hence, using the constitutive relationships as an intermediate stage and then applying the inverse Fourier transform, precisely the identity $j\omega f(\omega) = \partial f(t)/\partial t$, yields a system of time-domain differential equations [5]. This system can be straightforwardly implemented into the Discontinuous Galerkin (DG) method [40].

Furthermore, the electric flux density $\boldsymbol{\mathcal{D}}(\boldsymbol{x},t)$ and the magnetic flux density $\boldsymbol{\mathcal{B}}(\boldsymbol{x},t)$ retain their physical interpretations beyond the boundaries of the uniaxial PML region. Moreover, rather than modifying the parameter κ_i individually for $i = x, y, z$, it is generally simpler and equivalent from an implementation point of view to set $k_i = 1$ for $i = x, y, z$ and to alter the geometry of the PML through stretching.

4.4 Sources

This section focuses on two widely employed approaches for incorporating sources in the DGTD method: modeling current point sources and utilizing the Total-Field/Scattered-Field (TF/SF) formulation. However, alternative methods are also viable, such as directly modifying the magnetic field associated with the node positioned at $\boldsymbol{x}_0$ through $\boldsymbol{\mathcal{H}}(\boldsymbol{x}_0,t) = \hat{\boldsymbol{n}} \times \boldsymbol{\mathcal{J}}(\boldsymbol{x}_0,t)$, or employing waveports to inject analytical solutions into the jump terms of the flux [17].

4.4.1 Current Point Source

The simplest approach to address this issue is by incorporating the source term $\boldsymbol{\mathcal{J}}(\boldsymbol{x},t)$ found in Maxwell's equations. This can be seen in the following equation

$$\nabla \times \boldsymbol{\mathcal{H}}(\boldsymbol{x},t) = \epsilon(\boldsymbol{x},t)\frac{\partial \boldsymbol{\mathcal{E}}(\boldsymbol{x},t)}{\partial t} + \boldsymbol{\mathcal{J}}(\boldsymbol{x},t). \tag{4.45}$$

This method is highly attractive for modeling point sources as they can be easily represented by a singular current distribution like

$$\boldsymbol{\mathcal{J}}(\boldsymbol{x},t) = I_0 \boldsymbol{l} \cdot f(t) \cdot \delta^3(\boldsymbol{x} - \boldsymbol{x}_0), \tag{4.46}$$

where $I_0\boldsymbol{l}$ is current moment, $f(t)$ is its waveform and $\delta^3(\cdot)$ denotes the three-dimensional Dirac distribution.

Unfortunately, Lagrange polynomials are known to be inadequate in accurately determining field values near $\boldsymbol{x}_0$ where the values are theoretically infinite. In order to obtain the distribution of a field in the vicinity of $\boldsymbol{x}_0$, it would be necessary to significantly increase the mesh refinement locally, resulting in smaller time steps.

4.4.2 The Total Field/Scattered Field Formulation

Based on the Huygen's principle, it is possible to split the computational domain into two regions: the Total-Field Region (TFR) and Scattered-Field Region (SFR). This technique, known as the TF/SF formulation [36], is widely used in the FDTD method. It relies on the linearity of Maxwell's equations and the known scattering relation

$$\vec{q}_{\text{tot}}(\boldsymbol{x},t) = \vec{q}_{\text{inc}}(\boldsymbol{x},t) + \vec{q}_{\text{scat}}(\boldsymbol{x},t). \tag{4.47}$$

The subscripts "tot", "scat", and "inc" indicate the total, scattered and incident, i.e., physical fields, respectively. The incident field is a known analytical expression, e.g., a plane wave. An illustration of the scheme is shown in Figure 7.

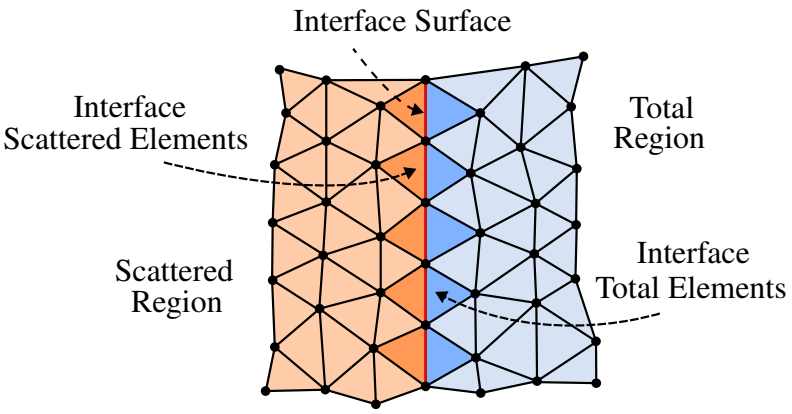

Figure 7 – Illustration of the TF/SF scheme.

Due to linearity, Equation (4.3) is still valid in the TFR and SFR. Hence, the following equations

$$Q\frac{\partial \vec{q}_{\text{tot}}(\boldsymbol{x},t)}{\partial t} + \nabla\cdot\vec{\boldsymbol{\mathcal{F}}}(\vec{q}_{\text{tot}}(\boldsymbol{x},t),\boldsymbol{x},t) = 0, \tag{4.48}$$

$$Q\frac{\partial \vec{q}_{\text{scat}}(\boldsymbol{x},t)}{\partial t} + \nabla\cdot\vec{\boldsymbol{\mathcal{F}}}(\vec{q}_{\text{scat}}(\boldsymbol{x},t),\boldsymbol{x},t) = 0, \tag{4.49}$$

are solved in their respective domains. The field differences are

$$[\vec{q}_{\text{tot}}(\boldsymbol{x},t)] = \vec{q}^{-}_{\text{tot}}(\boldsymbol{x},t) - \vec{q}^{+}_{\text{tot}}(\boldsymbol{x},t), \tag{4.50}$$

$$[\vec{q}_{\text{scat}}(\boldsymbol{x},t)] = \vec{q}^{-}_{\text{scat}}(\boldsymbol{x},t) - \vec{q}^{+}_{\text{scat}}(\boldsymbol{x},t). \tag{4.51}$$

As long as the local element is within TFR or SFR, the evaluation is straightforward. The only change happens at interface elements sharing a face, indicated in Figure 7, with the TF/SF interface surface. If the local element is in the TFR, the field difference is updated to

$$[\vec{q}(\boldsymbol{x},t)]_{\text{tot}} = \vec{q}^{-}_{\text{tot}}(\boldsymbol{x},t) - \vec{q}^{+}_{\text{scat}}(\boldsymbol{x},t) - \vec{q}_{\text{inc}}(\boldsymbol{x},t), \tag{4.52}$$

while if the local element is within the SFR

$$[\vec{q}(\boldsymbol{x},t)]_{\text{scat}} = \vec{q}^{-}_{\text{scat}}(\boldsymbol{x},t) - \vec{q}^{+}_{\text{tot}}(\boldsymbol{x},t) + \vec{q}_{\text{inc}}(\boldsymbol{x},t). \tag{4.53}$$

The use of Equation (4.53) can be seen in Figure 8 considering a one-dimensional electric field analyzed from the perspective of an element in the SFR region. As shown, the total electric field $\mathcal{E}^{+}_{\text{scat}}$ in the TFR is converted to its scattered counterpart $\mathcal{E}^{+}_{\text{scat}}$ by subtracting the incident field $\mathcal{E}_{\text{inc}}$. The resulting $[\mathcal{E}]_{\text{scat}}$ is then used in the calculation of the flux difference.

This formulation has the requirement that all electromagnetic fields must approach zero at $t = 0$ everywhere [40].

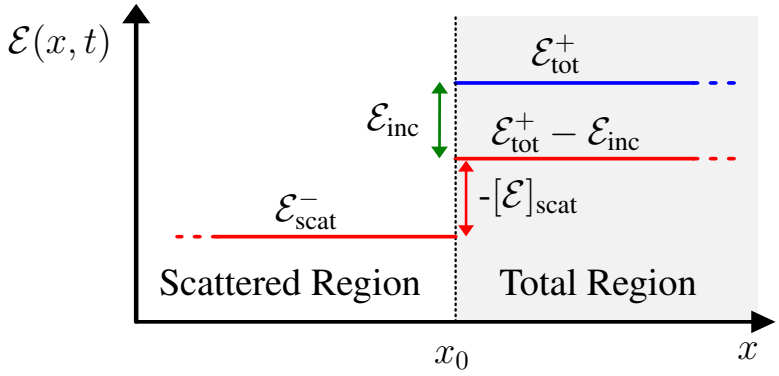

Figure 8 – One-dimensional TF/SF scheme.
Conversion considering an element within the SFR.

CHAPTER 5

DGTD Method Applied to General Dispersive Materials

The DGTD method offers an effective approach for solving electromagnetic problems, particularly in scattering, wave propagation, and antenna analysis [42, 43, 44, 45, 46]. It combines the geometric flexibility of the FEM [8] with, to some extent, the versatility of explicit time integration of the FDTD method [5].

In this chapter, the standard DGTD framework for solving Maxwell's equations [6] is extended to handle general dielectric dispersive media modeled by the CCPR model [26] and to incorporate a *dispersive* PML absorbing boundary condition in a modular way. Unlike earlier approaches based on Padé approximants that rely on Scattering Boundary Condition (SBC) for domain truncation [47] or demand extra space between the scatterer and the PML [48], the proposed DGTD formulation is a generalization of [22] that allows for direct truncation of dispersive materials without any additional free space. It incorporates a general dielectric dispersive CCPR model [17] while extending the uniaxial PML [16] to match general dispersive media, enabling efficient simulation of open space [28].

This formulation first solves the standard Maxwell equations across the entire domain, providing a unified baseline. Additional terms, such as those for PML or dispersive media modeled using vector fitting [27], are then selectively added through the ADE approach, in a plug-and-play fashion. Depending on each region's characteristics—dispersive media, simple dielectric PML, or dispersive PML—additional differential equations and correction terms are incorporated as needed (see Figure 9). This modular approach activates specific extensions only in targeted regions, enabling efficient batch processing and scalable computation. The careful definition of ADE terms, particularly for boundary conditions in dispersive media, ensures the algorithm remains adaptable and modular.

The main advantage of this approach is its modularity, combined with the ability to directly truncate general dispersive media without any additional free space. It is particularly

beneficial for wideband problems [23, 24, 25] in open domains, where multiple dispersion terms are required to capture material behavior across a broad frequency range efficiently.

Additionally, incident fields are naturally incorporated using the TF/SF formulation [5]. Numerical validation is performed by comparing the DGTD solutions of two-dimensional and three-dimensional canonical scattering problems with their analytical counterparts.

5.1 Mathematical Formulation

Maxwell's curl equations for lossless linear media without sources [8] are written as

$$\bar{\bar{\mu}}(\boldsymbol{r})\frac{\partial \boldsymbol{\mathcal{H}}(\boldsymbol{r},t)}{\partial t} + \nabla \times \boldsymbol{\mathcal{E}}(\boldsymbol{r},t) = 0, \qquad \text{(4.1 revisited)}$$

$$\bar{\bar{\epsilon}}(\boldsymbol{r})\frac{\partial \boldsymbol{\mathcal{E}}(\boldsymbol{r},t)}{\partial t} - \nabla \times \boldsymbol{\mathcal{H}}(\boldsymbol{r},t) = 0, \qquad \text{(4.2 revisited)}$$

where $\boldsymbol{\mathcal{E}}$ and $\boldsymbol{\mathcal{H}}$ are the electric and magnetic fields in the time domain, respectively. Additionally, $\bar{\bar{\epsilon}}$ and $\bar{\bar{\mu}}$ are the electric permittivity and the magnetic permeability tensors, respectively. Furthermore, $\boldsymbol{r}$ and t indicate the spatial and temporal dependencies, respectively. In conservation form, the aforementioned equations become [39]

$$\boldsymbol{Q}(\boldsymbol{r})\frac{\partial \vec{q}(\boldsymbol{r},t)}{\partial t} + \nabla \cdot \vec{\boldsymbol{\mathcal{F}}}(\vec{q},\boldsymbol{r},t) = 0. \qquad \text{(4.3 revisited)}$$

For simplicity, any medium in this work is considered isotropic.

5.1.1 Dispersive Media Modeling

A general dispersive dielectric material can be modeled by considering its permittivity $\epsilon(\omega)$ as $\epsilon_0\epsilon_\infty + \epsilon_0\chi_e(\omega)$, where ϵ_∞ is the high frequency relative permittivity limit and $\chi_e(\omega)$ is the frequency-dependent electric susceptibility. Specifically, using the CCPR model [26], $\chi_e(\omega)$ can be expanded as

$$\chi_e(\omega) = \sum_{r=1}^{R}\left(\frac{c_r}{j\omega - a_r} + \frac{c_r^*}{j\omega - a_r^*}\right), \tag{5.1}$$

where R is the number of poles, c_r and a_r are the model's parameters obtained from data fitting.

This dispersion model can be incorporated via the electric constitutive equation as

$$j\omega\boldsymbol{D}(\boldsymbol{r},\omega) = j\omega\epsilon_0\epsilon_\infty\boldsymbol{E}(\boldsymbol{r},\omega) + j\omega\epsilon_0\chi_e(\omega)\boldsymbol{E}(\boldsymbol{r},\omega). \tag{5.2}$$

The aforementioned equation can be decomposed into the following system of equations

$$j\omega\boldsymbol{D}(\boldsymbol{r},\omega) = j\omega\epsilon_0\epsilon_\infty\boldsymbol{E}(\boldsymbol{r},\omega) + \epsilon_0\boldsymbol{K}(\boldsymbol{r},\omega), \tag{5.3}$$

$$\boldsymbol{K}(\boldsymbol{r},\omega) = j\omega\chi_e(\boldsymbol{r},\omega)\boldsymbol{E}(\boldsymbol{r},\omega). \tag{5.4}$$

By introducing the following definitions

$$\boldsymbol{P}_r(\boldsymbol{x},\omega) = \frac{c_r}{j\omega - a_r}\boldsymbol{E}(\boldsymbol{x},\omega), \tag{5.5}$$

$$\boldsymbol{P}'_r(\boldsymbol{x},\omega) = \frac{c^*_r}{j\omega - a^*_r}\boldsymbol{E}(\boldsymbol{x},\omega), \tag{5.6}$$

where both of them can be easily converted back to the time-domain as

$$\frac{\partial \boldsymbol{\mathcal{P}}_r(\boldsymbol{x},t)}{\partial t} - a_r\boldsymbol{\mathcal{P}}_r(\boldsymbol{x},t) = c_r\boldsymbol{\mathcal{E}}(\boldsymbol{x},t), \tag{5.7}$$

$$\frac{\partial \boldsymbol{\mathcal{P}}'_r(\boldsymbol{x},t)}{\partial t} - a^*_r\boldsymbol{\mathcal{P}}'_r(\boldsymbol{x},t) = c^*_r\boldsymbol{\mathcal{E}}(\boldsymbol{x},t), \tag{5.8}$$

Equation (5.4) can be rewritten as

$$\boldsymbol{K}(\boldsymbol{x},\omega) = j\omega\sum_{r=1}^{R}\left(\boldsymbol{P}_r(\boldsymbol{x},\omega) + \boldsymbol{P}'_r(\boldsymbol{x},\omega)\right). \tag{5.9}$$

Since $\boldsymbol{\mathcal{E}}(\boldsymbol{x},t) \in \mathbb{R}$, it implies that $\boldsymbol{\mathcal{P}}'_r(\boldsymbol{x},t) = \boldsymbol{\mathcal{P}}^*_r(\boldsymbol{x},t)$, resulting in its time-domain equation to be

$$\boldsymbol{\mathcal{K}}(\boldsymbol{x},t) = 2\sum_{r=1}^{R}\Re\left\{\frac{\partial \boldsymbol{\mathcal{P}}_r(\boldsymbol{x},t)}{\partial t}\right\}, \tag{5.10}$$

with only one of ADEs (5.7) or (5.8) needing to be solved. Therefore, within a dispersive material, (4.2) becomes

$$\nabla\times\boldsymbol{\mathcal{H}}(\boldsymbol{r},t) = \epsilon_0\epsilon_\infty\frac{\partial\boldsymbol{\mathcal{E}}(\boldsymbol{r},t)}{\partial t} - 2\epsilon_0\sum_{r=1}^{R}\Re\left\{\frac{\partial \boldsymbol{\mathcal{P}}_r(\boldsymbol{r},t)}{\partial t}\right\}, \tag{5.11}$$

and an additional ADE of a polarization field $\boldsymbol{\mathcal{P}}_r$ for every pole r is solved

$$\frac{\partial \boldsymbol{\mathcal{P}}_r(\boldsymbol{r},t)}{\partial t} = a_r\boldsymbol{\mathcal{P}}_r(\boldsymbol{r},t) + c_r\boldsymbol{\mathcal{E}}(\boldsymbol{r},t). \tag{5.12}$$

5.1.2 Perfectly Matched Layer

To truncate unbounded domains, the uniaxial PML [16] technique can be used by introducing matched artificial conductivities in the outer regions of the grid to absorb outgoing waves. This PML is incorporated by modifying the electrical constitutive equation to

$$j\omega\boldsymbol{D}(\boldsymbol{x},\omega) = j\omega\bar{\bar{\Lambda}}\epsilon_0\epsilon_\infty\boldsymbol{E}(\boldsymbol{x},\omega), \tag{5.13}$$

where the tensor $\bar{\bar{\Lambda}}$ is defined as

$$\bar{\bar{\Lambda}} = \begin{bmatrix} s_y s_z/s_x & 0 & 0 \\ 0 & s_x s_z/s_y & 0 \\ 0 & 0 & s_x s_y/s_z \end{bmatrix}, \tag{5.14}$$

with $s_i = 1 + \sigma_i/j\omega$ for $i = x, y, z$. Equation (5.13) can be rewritten as [40]

$$j\omega \boldsymbol{D}(\boldsymbol{x},\omega) = j\omega\epsilon_0\epsilon_\infty \boldsymbol{E}(\boldsymbol{x},\omega) + j\omega(\bar{\bar{\Lambda}} - \boldsymbol{I})\epsilon_0\epsilon_\infty \boldsymbol{E}(\boldsymbol{x},\omega), \tag{5.15}$$

which it can be further decomposed into the following set of equations

$$j\omega \boldsymbol{D}(\boldsymbol{x},\omega) = j\omega\epsilon_0\epsilon_\infty \boldsymbol{E}(\boldsymbol{x},\omega) + \epsilon_0 \boldsymbol{U}(\boldsymbol{x},\omega), \tag{5.16}$$

$$\boldsymbol{U}(\boldsymbol{x},\omega) = j\omega(\bar{\bar{\Lambda}} - \boldsymbol{I})\epsilon_\infty \boldsymbol{E}(\boldsymbol{x},\omega). \tag{5.17}$$

By defining the following coefficients

$$\bar{\bar{\sigma}}_0 = \begin{bmatrix} \sigma_x & 0 & 0 \\ 0 & \sigma_y & 0 \\ 0 & 0 & \sigma_z \end{bmatrix}, \quad \bar{\bar{\sigma}}_1 = \begin{bmatrix} \sigma_y\sigma_z & 0 & 0 \\ 0 & \sigma_x\sigma_z & 0 \\ 0 & 0 & \sigma_x\sigma_y \end{bmatrix},$$

$$\bar{\bar{\sigma}}_2 = \begin{bmatrix} \sigma_y + \sigma_z - \sigma_x & 0 & 0 \\ 0 & \sigma_x + \sigma_z - \sigma_y & 0 \\ 0 & 0 & \sigma_x + \sigma_y - \sigma_z \end{bmatrix},$$

Equation (5.17) can be expanded to

$$\bar{\bar{\sigma}}_0 \boldsymbol{U}(\boldsymbol{x},\omega) = \bar{\bar{\sigma}}_1\epsilon_\infty \boldsymbol{E}(\boldsymbol{x},\omega) + j\omega\left[-\boldsymbol{U}(\boldsymbol{x},\omega) + \bar{\bar{\sigma}}_2\epsilon_\infty \boldsymbol{E}(\boldsymbol{x},\omega)\right]. \tag{5.18}$$

The following substitution

$$\boldsymbol{K}(\boldsymbol{x},\omega) = -\boldsymbol{U}(\boldsymbol{x},\omega) + \bar{\bar{\sigma}}_2\epsilon_\infty \boldsymbol{E}(\boldsymbol{x},\omega), \tag{5.19}$$

results in the following equation after some simplifications

$$j\omega \boldsymbol{K}(\boldsymbol{x},\omega) = -\bar{\bar{\sigma}}_0 \boldsymbol{K}(\boldsymbol{x},\omega) + \left(\bar{\bar{\sigma}}_0\bar{\bar{\sigma}}_2 - \bar{\bar{\sigma}}_1\right)\epsilon_\infty \boldsymbol{E}(\boldsymbol{x},\omega), \tag{5.20}$$

which in the time domain simply becomes

$$\frac{\partial \boldsymbol{\mathcal{K}}(\boldsymbol{r},t)}{\partial t} = -\bar{\bar{\sigma}}_0 \boldsymbol{\mathcal{K}}(\boldsymbol{r},t) + \left(\bar{\bar{\sigma}}_0\bar{\bar{\sigma}}_2 - \bar{\bar{\sigma}}_1\right)\epsilon_\infty \boldsymbol{\mathcal{E}}(\boldsymbol{r},t). \tag{5.21}$$

The same procedure can be applied to the magnetic field, resulting in the following ADE

$$\frac{\partial \boldsymbol{\mathcal{G}}(\boldsymbol{r},t)}{\partial t} = -\bar{\bar{\sigma}}_0 \boldsymbol{\mathcal{G}}(\boldsymbol{r},t) + \left(\bar{\bar{\sigma}}_0\bar{\bar{\sigma}}_2 - \bar{\bar{\sigma}}_1\right) \boldsymbol{\mathcal{H}}(\boldsymbol{r},t). \tag{5.22}$$

Finally, the set of equations to be solved within the uniaxial PML is given by

$$\nabla \times \boldsymbol{\mathcal{H}}(\boldsymbol{x},t) = \epsilon_0\epsilon_\infty \frac{\partial \boldsymbol{\mathcal{E}}(\boldsymbol{x},t)}{\partial t} - \epsilon_0 \boldsymbol{\mathcal{K}}(\boldsymbol{x},t) + \bar{\bar{\sigma}}_2\epsilon_0\epsilon_\infty \boldsymbol{\mathcal{E}}(\boldsymbol{x},t), \tag{5.23}$$

$$\nabla \times \boldsymbol{\mathcal{E}}(\boldsymbol{x},t) = -\mu_0 \frac{\partial \boldsymbol{\mathcal{H}}(\boldsymbol{x},t)}{\partial t} - \mu_0 \boldsymbol{\mathcal{G}}(\boldsymbol{x},t) + \bar{\bar{\sigma}}_2\mu_0 \boldsymbol{\mathcal{H}}(\boldsymbol{x},t), \tag{5.24}$$

$$\frac{\partial \boldsymbol{\mathcal{K}}(\boldsymbol{x},t)}{\partial t} = -\bar{\bar{\sigma}}_0 \boldsymbol{\mathcal{K}}(\boldsymbol{x},t) + \left(\bar{\bar{\sigma}}_0\bar{\bar{\sigma}}_2 - \bar{\bar{\sigma}}_1\right)\epsilon_\infty \boldsymbol{\mathcal{E}}(\boldsymbol{x},t), \tag{5.25}$$

$$\frac{\partial \boldsymbol{\mathcal{G}}(\boldsymbol{x},t)}{\partial t} = -\bar{\bar{\sigma}}_0 \boldsymbol{\mathcal{G}}(\boldsymbol{x},t) + \left(\bar{\bar{\sigma}}_0\bar{\bar{\sigma}}_2 - \bar{\bar{\sigma}}_1\right) \boldsymbol{\mathcal{H}}(\boldsymbol{x},t). \tag{5.26}$$

5.1.3 PML Matched to General Dispersive Media

In order to properly truncate dispersive media, it is necessary to incorporate the PML equations in tandem with the dispersive medium model. In this case, the electric constitutive equation becomes

$$j\omega \boldsymbol{D}(\boldsymbol{x},\omega) = j\omega[\boldsymbol{I} + (\bar{\bar{\Lambda}} - \boldsymbol{I})]\epsilon_0 \left(\epsilon_\infty + \chi_e(\boldsymbol{x},\omega)\right) \boldsymbol{E}(\boldsymbol{x},\omega). \tag{5.27}$$

Expanding the previous equation leads to

$$\begin{aligned} j\omega \boldsymbol{D}(\boldsymbol{x},\omega) = \overbrace{j\omega\epsilon_0\epsilon_\infty \boldsymbol{E}(\boldsymbol{x},\omega)}^{\text{simple dielectric}} + \overbrace{j\omega(\bar{\bar{\Lambda}} - \boldsymbol{I})\epsilon_0\epsilon_\infty \boldsymbol{E}(\boldsymbol{x},\omega)}^{\text{simple PML}} \\ + \underbrace{j\omega\epsilon_0\chi_e(\boldsymbol{x},\omega)\boldsymbol{E}(\boldsymbol{x},\omega)}_{\text{dispersive media}} + \underbrace{j\omega(\bar{\bar{\Lambda}} - \boldsymbol{I})\epsilon_0\chi_e(\boldsymbol{x},\omega)\boldsymbol{E}(\boldsymbol{x},\omega)}_{\text{coupling: PML + dispersive media}} \end{aligned} \tag{5.28}$$

where the simple dielectric, the dispersive media, and the simple PML terms have already been addressed in the previous subsections. Therefore, we focus next on the remaining coupling term.

By writing Equation (5.28) as the following set of equations

$$\begin{aligned} j\omega \boldsymbol{D}(\boldsymbol{x},\omega) = j\omega\epsilon_0\epsilon_\infty \boldsymbol{E}(\boldsymbol{x},\omega) + j\omega\epsilon_0\chi_e(\boldsymbol{x},\omega)\boldsymbol{E}(\boldsymbol{x},\omega) \\ + j\omega(\bar{\bar{\Lambda}} - \boldsymbol{I})\epsilon_0\epsilon_\infty \boldsymbol{E}(\boldsymbol{x},\omega) + \epsilon_0 \boldsymbol{R}(\boldsymbol{x},\omega), \end{aligned} \tag{5.29}$$

$$\boldsymbol{R}(\boldsymbol{x},\omega) = j\omega(\bar{\bar{\Lambda}} - \boldsymbol{I})\chi_e(\boldsymbol{x},\omega)\boldsymbol{E}(\boldsymbol{x},\omega), \tag{5.30}$$

and considering the subsequent definition

$$\boldsymbol{R}(\boldsymbol{x},\omega) = \sum_{r=1}^{R} \boldsymbol{R}_r(\boldsymbol{x},\omega), \tag{5.31}$$

Equation (5.30) can be rewritten as a sum of ADEs associated to each pole r as

$$j\omega \boldsymbol{R}_r(\boldsymbol{x},\omega) = -\bar{\bar{\sigma}}_0 \boldsymbol{R}_r(\boldsymbol{x},\omega) + (j\omega\bar{\bar{\sigma}}_2 + \bar{\bar{\sigma}}_1)\left(\boldsymbol{P}_r(\boldsymbol{x},\omega) + \boldsymbol{P}'_r(\boldsymbol{x},\omega)\right) \tag{5.32}$$

with its time-domain counterpart being

$$\frac{\partial \boldsymbol{\mathcal{R}}_r(\boldsymbol{x},t)}{\partial t} = -\bar{\bar{\sigma}}_0 \boldsymbol{\mathcal{R}}_r(\boldsymbol{x},t) + 2\bar{\bar{\sigma}}_1 \Re\left\{\boldsymbol{\mathcal{P}}_r(\boldsymbol{x},t)\right\} + 2\bar{\bar{\sigma}}_2 \Re\left\{\frac{\partial \boldsymbol{\mathcal{P}}_r(\boldsymbol{x},t)}{\partial t}\right\}. \tag{5.33}$$

Therefore, the set of equations to be solved are

$$\begin{aligned} \epsilon_0\epsilon_\infty \frac{\partial \boldsymbol{\mathcal{E}}(\boldsymbol{x},t)}{\partial t} = \nabla \times \boldsymbol{\mathcal{H}}(\boldsymbol{x},t) + \epsilon_0 \boldsymbol{\mathcal{K}}(\boldsymbol{x},t) - \bar{\bar{\sigma}}_2\epsilon_0\epsilon_\infty \boldsymbol{\mathcal{E}}(\boldsymbol{x},t) \\ - 2\epsilon_0 \sum_{r=1}^{R} \Re\left\{\frac{\partial \boldsymbol{\mathcal{P}}_r(\boldsymbol{x},t)}{\partial t}\right\} - \epsilon_0 \sum_{r=1}^{R} \boldsymbol{\mathcal{R}}_r(\boldsymbol{x},t), \end{aligned} \tag{5.34}$$

$$\mu_0 \frac{\partial \boldsymbol{\mathcal{H}}(\boldsymbol{x},t)}{\partial t} = -\nabla \times \boldsymbol{\mathcal{E}}(\boldsymbol{x},t) + \mu_0 \boldsymbol{\mathcal{G}}(\boldsymbol{x},t) - \bar{\bar{\sigma}}_2\mu_0 \boldsymbol{\mathcal{H}}(\boldsymbol{x},t), \tag{5.35}$$

$$\frac{\partial \boldsymbol{\mathcal{K}}(\boldsymbol{x},t)}{\partial t} = -\bar{\bar{\sigma}}_0 \boldsymbol{\mathcal{K}}(\boldsymbol{x},t) + (\bar{\bar{\sigma}}_0 \bar{\bar{\sigma}}_2 - \bar{\bar{\sigma}}_1)\, \epsilon_\infty \boldsymbol{\mathcal{E}}(\boldsymbol{x},t), \tag{5.36}$$

$$\frac{\partial \boldsymbol{\mathcal{G}}(\boldsymbol{x},t)}{\partial t} = -\bar{\bar{\sigma}}_0 \boldsymbol{\mathcal{G}}(\boldsymbol{x},t) + (\bar{\bar{\sigma}}_0 \bar{\bar{\sigma}}_2 - \bar{\bar{\sigma}}_1)\, \boldsymbol{\mathcal{H}}(\boldsymbol{x},t), \tag{5.37}$$

$$\frac{\partial \boldsymbol{\mathcal{P}}_r(\boldsymbol{x},t)}{\partial t} = a_r \boldsymbol{\mathcal{P}}_r(\boldsymbol{x},t) + c_r \boldsymbol{\mathcal{E}}(\boldsymbol{x},t), \quad r = 1,\ldots,R, \tag{5.38}$$

$$\frac{\partial \boldsymbol{\mathcal{R}}_r(\boldsymbol{x},t)}{\partial t} = -\bar{\bar{\sigma}}_0 \boldsymbol{\mathcal{R}}_r(\boldsymbol{x},t) + 2\bar{\bar{\sigma}}_2 \Re\left\{\frac{\partial \boldsymbol{\mathcal{P}}_r(\boldsymbol{x},t)}{\partial t}\right\} + 2\bar{\bar{\sigma}}_1 \Re\left\{\boldsymbol{\mathcal{P}}_r(\boldsymbol{x},t)\right\} \quad r = 1,\ldots,R. \tag{5.39}$$

5.1.4 Modular Implementation

An examination of all possible scenarios makes it evident that the (simple) dielectric case, Equations (4.1) and (4.2), the dispersive media case, Equations (4.1), (5.11) and (5.12), and the dielectric PML case, Equations (5.23) to (5.26), are just specific instances of the more general dispersive PML case, Equations (5.34) to (5.39). Notably, while the (simple) dielectric media case can be computed for the entire domain directly, other regions only require respective additional terms according to their specific characteristics. This modular approach is illustrated in Figure 9.

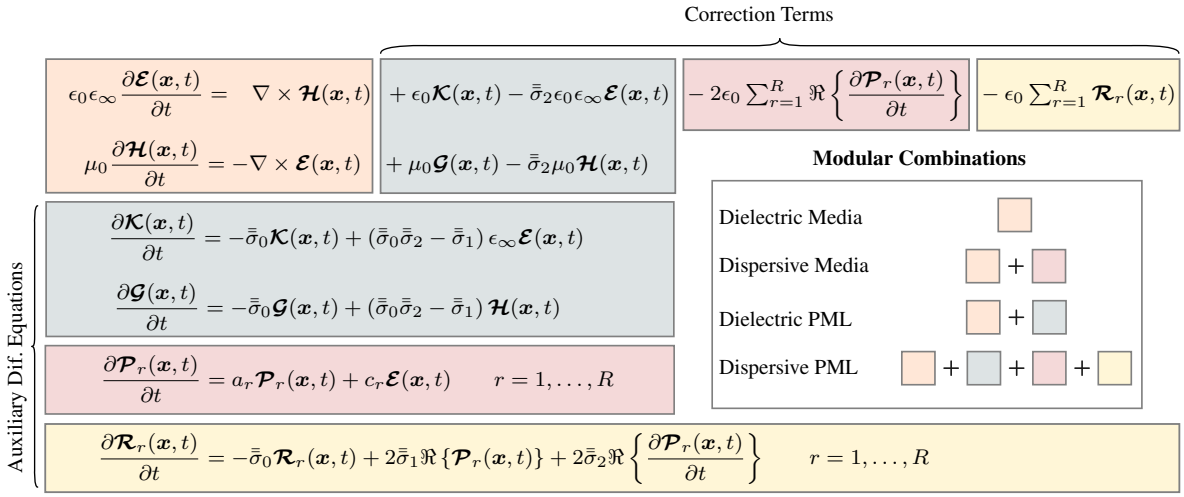

Figure 9 – Illustration of the modular implementation of Maxwell's equations containing dispersive media truncated by dispersive PML

The system of equations is solved synchronously, with each timestep iteration computing the Right-Hand Side (RHS) numerically. Initially, Maxwell's equations for dielectric media are computed across the entire computational domain using the respective nodal fields $\boldsymbol{\mathcal{E}}$ and $\boldsymbol{\mathcal{H}}$ (highlighted in orange). If the region is dispersive, additional auxiliary fields $\boldsymbol{\mathcal{P}}_r$ are added *in place* to the RHS, updating the previously calculated values for that region based on their respective ADE (highlighted in red). In regions with dielectric PML, the RHS is updated *in place* with terms involving the nodal fields $\boldsymbol{\mathcal{G}}$ and $\boldsymbol{\mathcal{K}}$, which are calculated using their respective ADEs (highlighted in gray). In regions with dispersive PML, the updates for both dispersive

media and dielectric PML are combined, introducing an additional coupling $\boldsymbol{\mathcal{R}}_r$ (highlighted in yellow). Auxiliary fields are defined only when needed, and region updates are performed via array indexing.

5.2 The Discontinous Galerkin Method

Assume that Ω_h is a tessellated finite region (bounded by $\partial\Omega_h$) of the physical domain Ω with K non-overlapping elements (Ω_h^k, bounded by $\partial\Omega_h^k$) where Equation (4.3) is to be solved. Thus

$$\Omega \approx \Omega_h = \bigcup_k^K \Omega_h^k. \tag{5.40}$$

A globally defined vector space $\mathcal{V}_h$ is introduced to approximate $\vec{q}(\boldsymbol{r},t)$ given that $\mathcal{V}_h = \oplus_{k=1}^K \mathcal{V}_h^k$, where the locally defined vector spaces are defined as $\mathcal{V}_h^k = \text{span}\{\psi_n(\Omega_h^k)\}_{n=1}^{N_p}$. Considering that $\mathcal{V}_h$ is piecewise smooth over Ω_h, a local approximation $\vec{q}_h^k(\boldsymbol{r},t)$ is defined in the local vector space $\mathcal{V}_h$ [6]

$$\vec{q}_h^k(\boldsymbol{r},t) = \sum_{n=1}^{N_p} \vec{\hat{q}}_n^k(t)\cdot\psi_n(\boldsymbol{r}) = \sum_{i=1}^{N_p} \vec{\tilde{q}}_h^k(\boldsymbol{r},t)\cdot l_i(\boldsymbol{r}) \quad \boldsymbol{r}\in\Omega^k, \tag{5.41}$$

where l_i are the interpolating Lagrange nodal-basis which possess the Kronecker delta property [40]. The relation between modal coefficients $\vec{\hat{q}}_n^k(t)$ and nodal coefficients $\vec{\tilde{q}}_h^k(\boldsymbol{r},t)$ is given by the Vandermonde matrix [6]. The modal-basis are usually chosen to be normalized monomials, while the interpolating positions $\boldsymbol{r}$ are spread in a Gauss-Lobatto alike distribution, usually obtained by the Warp-Blend method [6].

By applying the Galerkin testing and local integration by parts over Equation (4.3) for each element, the strong variational formulation of Maxwell's curl equations [40] writes as

$$\int_{\Omega_h^k}\left[Q\frac{\partial\vec{q}_h^k}{\partial t} + \nabla\cdot\vec{\boldsymbol{\mathcal{F}}}_h^k(\vec{q}_h^k)\right]\cdot l_i(\boldsymbol{x})\,d\Omega = \int_{\partial\Omega_h^k}\hat{\boldsymbol{n}}\cdot\left[\vec{\boldsymbol{\mathcal{F}}}_h^k(\vec{q}_h^k) - \vec{\boldsymbol{\mathcal{F}}}^*(\vec{q}_h^k)\right]\cdot l_i(\boldsymbol{x})\,d\Omega \quad \forall l_i\in\mathcal{V}_h^k, \tag{5.42}$$

where $\hat{\boldsymbol{n}}$ is the outward unit vector normal to the boundary surface $\partial\Omega_h^k$ and $\mathcal{F}_h^k - \mathcal{F}^*$ are termed as the numerical flux difference used for inter-element coupling. Within each element, the physical fields $\boldsymbol{\mathcal{E}}(\boldsymbol{x},t)$ and $\boldsymbol{\mathcal{H}}(\boldsymbol{x},t)$ are approximated by $\boldsymbol{\mathcal{E}}_h^k(\boldsymbol{x},t)$ and $\boldsymbol{\mathcal{H}}_h^k(\boldsymbol{x},t)$ using nodal basis functions as

$$\boldsymbol{\mathcal{E}}_h^k(\boldsymbol{x},t) = \sum_{i=1}^{N_p}\tilde{\boldsymbol{e}}_h^k(\boldsymbol{x}_i,t)\cdot l_i(\boldsymbol{x}) \qquad \boldsymbol{x}\in\Omega_h^k, \tag{5.43}$$

$$\boldsymbol{\mathcal{H}}_h^k(\boldsymbol{x},t) = \sum_{i=1}^{N_p}\tilde{\boldsymbol{h}}_h^k(\boldsymbol{x}_i,t)\cdot l_i(\boldsymbol{x}) \qquad \boldsymbol{x}\in\Omega_h^k, \tag{5.44}$$

where $\tilde{\boldsymbol{e}}_h^k$ and $\tilde{\boldsymbol{h}}_h^k$ are the nodal coefficients. After replacing Equations (5.43) and (5.44) into Equation (5.42) and assuming that Q in Equation (4.3) is constant within each element for simplicity, the integrals simplify to

$$M_{ij}^k = \int_{\Omega_h^k} l_i(\boldsymbol{x}) \cdot l_j(\boldsymbol{x})\, d\Omega, \tag{5.45}$$

$$S_{ij,s}^k = \int_{\Omega_h^k} l_i(\boldsymbol{x}) \cdot \frac{\partial l_j(\boldsymbol{x})}{\partial s}\, d\Omega \quad s = x, y, z, \tag{5.46}$$

$$F_{ij,f}^k = \int_{\partial\Omega_h^k} l_i(\boldsymbol{x}) \cdot l_j(\boldsymbol{x})\, d\Omega, \tag{5.47}$$

where M^k is the mass matrix, S_s^k is the stiffness matrix along the s component, and F_f^k is the face mass matrix for face f. By isolating the time-derivatives and approximating the fields $\boldsymbol{\mathcal{K}}$, $\boldsymbol{\mathcal{G}}$, $\boldsymbol{\mathcal{P}}$, $\boldsymbol{\mathcal{R}}$ in a similar fashion as in Equations (5.43) and (5.44), one obtains

$$\epsilon_0 \epsilon_\infty^k \frac{\partial \tilde{\boldsymbol{e}}^k}{\partial t} = \left(M^k\right)^{-1} \cdot \left[\boldsymbol{S}^k \times \tilde{\boldsymbol{h}}^k + \sum_f F_f^k \cdot \left(\hat{\boldsymbol{n}} \cdot \left[\vec{\boldsymbol{\mathcal{F}}}_E^k - \vec{\boldsymbol{\mathcal{F}}}_E^* \right] \right) \right] + \epsilon_0 \tilde{\boldsymbol{k}}^k - \bar{\bar{\sigma}}_2 \epsilon_0 \epsilon_\infty^k \tilde{\boldsymbol{e}}^k - 2\epsilon_0 \sum_{r=1}^{R} \Re\left\{ \frac{\partial \tilde{\boldsymbol{p}}_r^k}{\partial t} \right\} - \epsilon_0 \sum_{r=1}^{R} \tilde{\boldsymbol{r}}_r, \tag{5.48}$$

$$\mu_0 \frac{\partial \tilde{\boldsymbol{h}}^k}{\partial t} = \left(M^k\right)^{-1} \cdot \left[-\boldsymbol{S}^{\boldsymbol{k}} \times \tilde{\boldsymbol{e}}^k + \sum_f F_f^k \cdot \left(\hat{\boldsymbol{n}} \cdot \left[\vec{\boldsymbol{\mathcal{F}}}_H^k - \vec{\boldsymbol{\mathcal{F}}}_H^* \right] \right) \right] + \mu_0 \tilde{\boldsymbol{g}}^k - \bar{\bar{\sigma}}_2 \mu_0 \tilde{\boldsymbol{h}}^k, \tag{5.49}$$

$$\frac{\partial \tilde{\boldsymbol{k}}^k}{\partial t} = -\bar{\bar{\sigma}}_0 \tilde{\boldsymbol{k}}^k + \left(\bar{\bar{\sigma}}_0 \bar{\bar{\sigma}}_2 - \bar{\bar{\sigma}}_1\right) \epsilon_\infty \tilde{\boldsymbol{e}}^k, \tag{5.50}$$

$$\frac{\partial \tilde{\boldsymbol{g}}^k}{\partial t} = -\bar{\bar{\sigma}}_0 \tilde{\boldsymbol{g}}^k + \left(\bar{\bar{\sigma}}_0 \bar{\bar{\sigma}}_2 - \bar{\bar{\sigma}}_1\right) \tilde{\boldsymbol{h}}^k, \tag{5.51}$$

$$\frac{\partial \tilde{\boldsymbol{p}}_r^k}{\partial t} = a_r \tilde{\boldsymbol{p}}_r^k + c_r \tilde{\boldsymbol{e}}^k \quad r = 1, \ldots, R, \tag{5.52}$$

$$\frac{\partial \tilde{\boldsymbol{r}}_r^k}{\partial t} = -\bar{\bar{\sigma}}_0 \tilde{\boldsymbol{r}}_r^k + 2\bar{\bar{\sigma}}_2 \Re\left\{ \frac{\partial \tilde{\boldsymbol{p}}_r^k}{\partial t} \right\} + 2\bar{\bar{\sigma}}_1 \Re\left\{ \tilde{\boldsymbol{p}}_r^k \right\} \quad r = 1, \ldots, R, \tag{5.53}$$

where $\boldsymbol{S}^k = \left[S_x^k, S_y^k, S_z^k\right]^\intercal$, and $\mathcal{F}_E$ and $\mathcal{F}_H$ are the fluxes related to the electric and magnetic field, respectively.

5.3 Numerical Results

This section validates the formulation by applying it to a two-dimensional canonical problem that covers all previously described scenarios, confirming its accuracy and reliability. Subsequently, the formulation is tested on a more complex three-dimensional problem to demonstrate its effectiveness in addressing intricate scenarios.

The explicit fourth-order Runge-Kutta method is used for time integration, with the time step based on the minimum nodal distance [6]. Simplexes (triangles in 2D and tetrahedra in 3D) are chosen as grid elements. The upwind scheme is used for numerical flux and boundary conditions are integrated into the flux calculation [6].

5.3.1 Two-Dimensional Scattering Problem

The proposed formulation is validated by analyzing the propagation of a TMz plane wave with normal incidence into a region containing dispersive dielectric media. This setup covers all possible scenarios: a PML truncating free space, free space itself, dispersive dielectric media, and a PML truncating the dispersive media, as shown in Figure 10. In the simulation, the

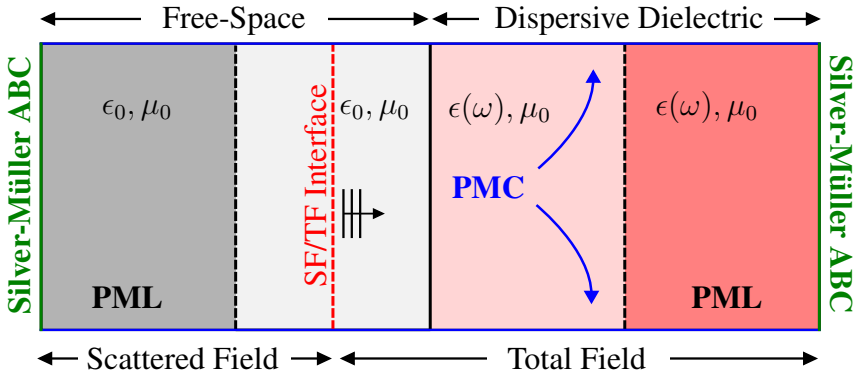

Figure 10 – Illustration of the two-dimensional case study.

incident field is given by

$$\boldsymbol{\mathcal{E}}_{\text{inc}}(\boldsymbol{x}, t) = g(t - \sqrt{\epsilon_0 \mu_0}\, \hat{\boldsymbol{x}} \cdot \boldsymbol{x})\hat{\boldsymbol{z}}, \tag{5.54}$$

$$\boldsymbol{\mathcal{H}}_{\text{inc}}(\boldsymbol{x}, t) = \sqrt{\frac{\epsilon_0}{\mu_0}}\hat{\boldsymbol{x}} \times \boldsymbol{\mathcal{E}}_{\text{inc}}(\boldsymbol{x}, t), \tag{5.55}$$

where $g(t)$ is the cosine-modulated Gaussian waveform

$$g(t) = \cos(2\pi f_c t) \exp\left(-t^2/\tau^2\right), \tag{5.56}$$

with f_c being its center frequency and τ representing its time constant. To analyze a frequency band from 100 MHz to 500 MHz, f_c was set to 300 MHz and τ was set to $0.8/f_c$ seconds. To ensure that the electromagnetic fields were zero at both the start and end of the simulation, a time delay of 7τ was applied, and the fields were simulated for a total duration of 20τ. A single Lorentz pole was used to model the dispersive dielectric media with its parameters set to $\omega_1 = 1.25 \times 2\pi f_c$, $\delta_1 = 0.3 \times \omega_1$, $\Delta\epsilon = 2.5$ and $\epsilon_\infty = 1$[26]. The computational domain of size $3\lambda_c \times 2\lambda_c$ was considered, where λ_c is the wavelength of the central frequency. The mesh size was set to $1/6\lambda_c$ and $1/12\lambda_c$, resulting in a total of 570 and 2070 elements, respectively. The PML profile was a second-degree polynomial with parameters chosen to achieve an attenuation

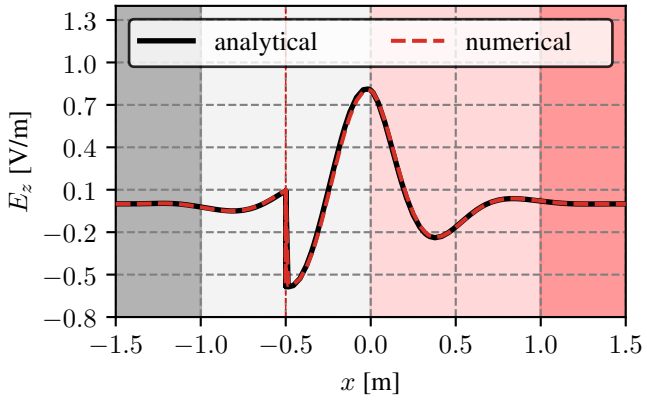

Figure 11 – Electric field with 6th order elements at $t = 7\tau$ and $1/6\lambda_c$ mesh.

of 72 dB within the PML. The geometric dimensions and the electric field at a cross-section along the propagation direction are shown in Figure 11.

To evaluate the impact of the frequency dependence of the dispersive dielectric media in the simulation, the relative L2 error was calculated as

$$\text{L2 Error} = \sqrt{\frac{\int_\Omega ||\mathbf{E}^\text{n} - \mathbf{E}^\text{a}||^2 d\Omega}{\int_\Omega ||\mathbf{E}^\text{a}||^2 d\Omega}}, \tag{5.57}$$

with a representing the analytical and n the numerical results. This error is determined by taking the Fourier transform of the electric field from the time-domain numerical solution and comparing it to the frequency-domain analytical solution, weighted by the incident field's frequency components.

Figure 12 shows how the error across the frequency band of interest changes with varying element orders. The gray area represents the frequency spectrum of the incident field, with its power spectrum aligned with the vertical axis of the error. The parabolic trend observed at lower

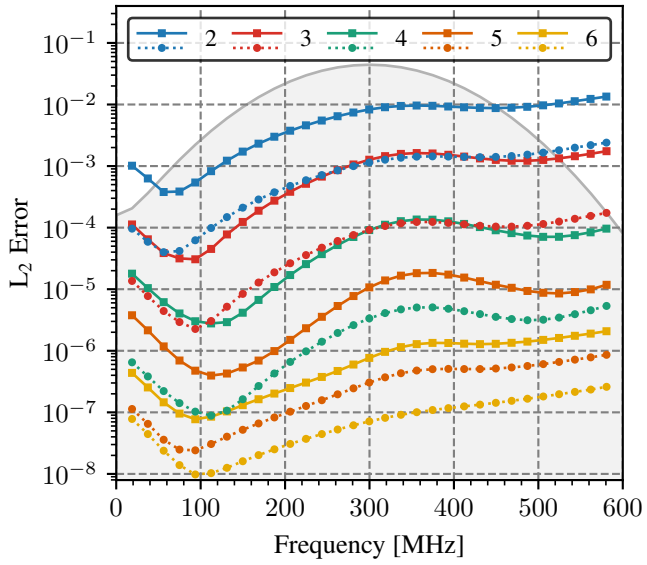

Figure 12 – L2 error of the electric field varying the order of the elements.

frequencies is related to the intensity of the incident field at those frequencies. As the frequency moves away from the center frequency, the spectral energy decreases, leading to a reduction in the denominator of Equation (5.57). The error also gradually increases with frequency due to numerical grid dispersion. As frequency rises, the spatial sampling rate (number of elements per wavelength) decreases, resulting in increased mesh dispersion. Figure 13 shows the convergence rate of the L2 error at the center frequency 300 MHz with varying element orders. It was observed that doubling the mesh density reduced the overall error by 20 dB with only minor variations in the spectrum.

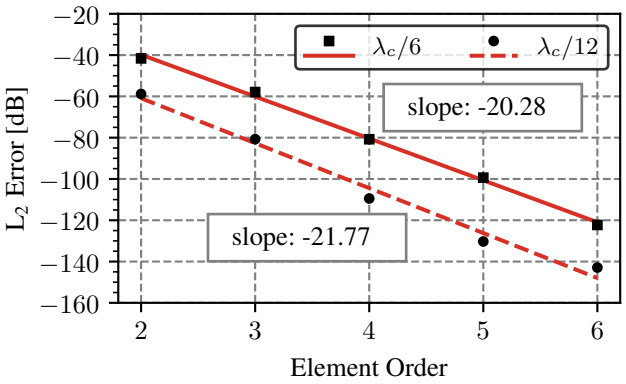

Figure 13 – Convergence rate of the L2 error varying element orders at 300 MHz.

5.3.2 Three-Dimensional Scattering Problem

The next problem involves the electromagnetic scattering of a plane wave by a dispersive dielectric sphere, as illustrated in Figure 14. The material properties of the sphere were deter-

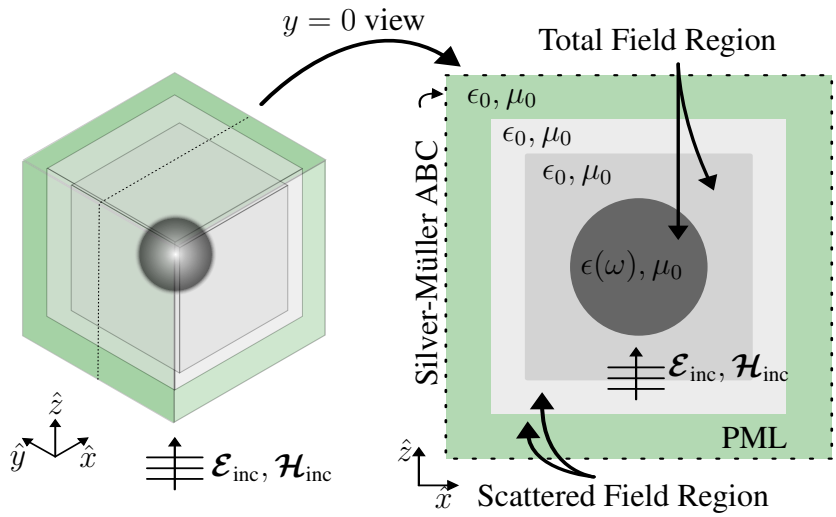

Figure 14 – Illustration of the three-dimensional case study.

mined using vector fitting with data from [49] for silver across the frequency range of 30 THz to 1200 THz. In contrast to [26], which employed six conjugate poles, a satisfactory approximation

was achieved with only three conjugate poles through basin-hopping combined with non-linear least squares optimization. The poles and residues of the fitted model are illustrated in Figure 15, and their values are listed in Table 8.

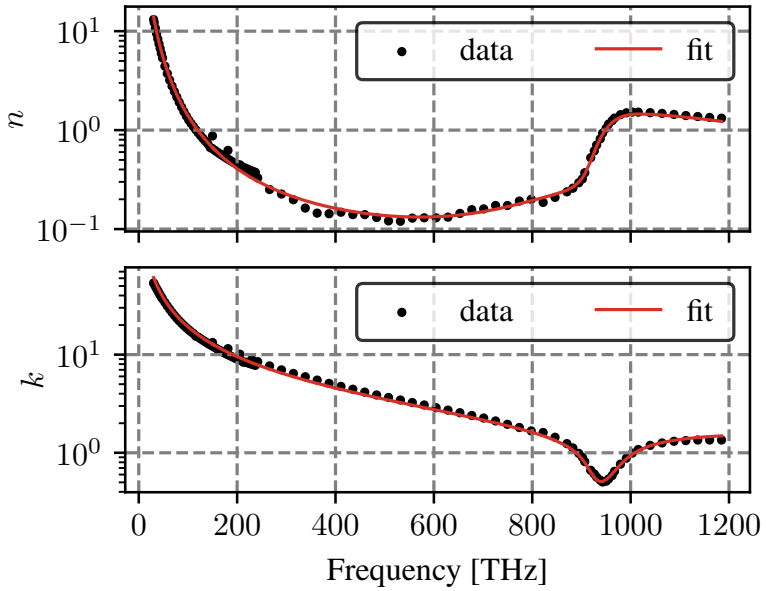

Figure 15 – Fitting of the refractive index n and extinction coefficient k of silver over the frequency range from 30 THz to 1200 THz.

Table 8 – Poles and residues of the fitted model

Residues	**Poles**
$+0.27 + 2931j$	$-0.03 - 0.01j$
$-29.39 + 212j$	$-18.60 - 3.75j$
$+1.10 + 0.61j$	$-0.37 - 4.20j$

The simulation was performed with a plane wave propagating in the z direction and the electric field polarized along x. To analyze the time-domain response, considering the frequency response of the material between 100 THz and 500 THz, the central frequency, f_c, was set to 300 THz, with $\tau = 0.8/f_c$ seconds. A time delay of 7τ was applied to ensure that the electromagnetic fields were zero at the start of the simulation. The total duration of the simulation was also 7τ seconds, which corresponds to the time when the electromagnetic incident field reaches its peak value. The computational domain had dimensions of $1.5\lambda_c \times 1.5\lambda_c \times 1.5\lambda_c$, where λ_c represents the wavelength at the center frequency. The mesh size within the sphere was set to $1/15\lambda_c$, and up to $1/4\lambda_c$ within the PML, resulting in a total of 4752 elements. The PML employed a second-degree polynomial profile, with parameters chosen to achieve an attenuation of 36 dB. The width of the PML was $0.25\lambda_c$, the width of the scattering region (excluding the PML) was $0.125\lambda_c$, and the radius of the sphere was $0.25\lambda_c$.

The absolute value of the electric field at the $y = 0$ plane is shown in Figure 16 while the normalized error at two different planes, absolute difference between the numerical solution and

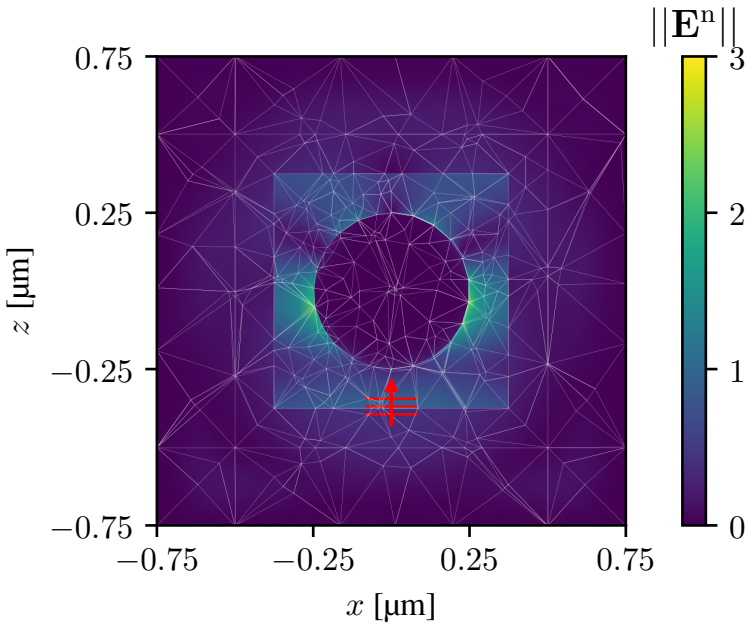

Figure 16 – Absolute value of the electric field at the $y = 0$ plane at $t = 7\tau$ using 4th order elements.

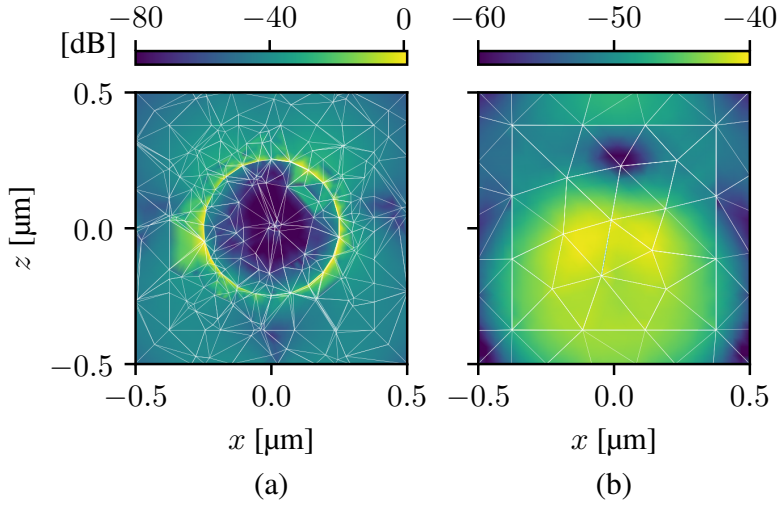

Figure 17 – Normalized error $||\boldsymbol{\mathcal{E}}^{\mathrm{n}} - \boldsymbol{\mathcal{E}}^{\mathrm{a}}||/E_0$ of the electric field at $t = 7\tau$ using 4th order elements at (a) $y = 0$ and (b) $y = -0.375\lambda_c$, excluding the PML, where E_0 is the amplitude of the incident field. The error slightly above 0 dB in (a) occurs only at elements intersecting the sphere due to rapid electric field changes and discretization, unlike (b), where the error stays below -40 dB.

the analytical solution [50] (with 50 terms) normalized by the amplitude the incident field, is shown in Figure 17 using 4th order elements. The error is concentrated near the surface of the sphere, as illustrated in Figure 17a. This discrepancy is attributed to the limited discretization of the sphere, which has a significant impact on the accuracy of the near field. Taking into account these factors, the relative L2 error was computed at the TF/SF interface, yielding a value of 1.04% with 4th order elements. The normalized error at one of the faces of the cube containing the TF/SF interface is shown in Figure 17b. This finding indicates a strong agreement between

the numerical and analytical solutions, especially considering the notable variation in permittivity of the material analyzed.

5.4 Conclusion

This work has presented a new formulation of the DGTD method applied to electromagnetic scattering problems involving general dispersive media modeled by vector fitting. The main contribution is enabling direct truncation of dispersive materials without the need for a region of simple dielectric between the scatterer and the PML by extending the uniaxial PML to handle general dispersive media based on the CCPR model. The formulation's modularity allows for flexible and efficient adaptation to various problem types, activating dispersive and/or PML components as needed. Numerical results for two-dimensional and three-dimensional scattering problems demonstrate excellent agreement with analytical solutions, showcasing the accuracy and flexibility of the proposed method.

CHAPTER 6

DGTD Method Applied to Doubly Dispersive Materials

In recent years, the demand for advanced modeling techniques in electromagnetics has increased substantially, as driven, for example, by the need to accurately simulate complex materials with both electric and magnetic dispersive properties [51, 52].

In this chapter, the modular implementation of the DGTD method [29] is extended to account for (a) doubly dispersive media exhibiting both dielectric and magnetic dispersion effects and (b) grids with curvilinear elements [6], which enables more accurate modeling of complex geometries. The proposed DGTD formulation is also capable of tackling unbounded domains. While various methods have been proposed to handle unbounded domains, such as absorbing boundary conditions [53, 28] or integral equation-based approaches [54], this work implements an extension of the uniaxial PML technique [16] to general doubly dispersive media.

These advancements aim at extending the capability of the DGTD method to address a wider range of electromagnetic problems [35, 55, 56], particularly those involving dispersive materials [57, 58, 59, 60] with intricate shapes. The proposed algorithm is validated through several examples that demonstrate its robustness and versatility.

6.1 Mathematical Formulation

6.1.1 Dispersive Media Modeling

In isotropic dispersive materials, the frequency-dependent permittivity can be expressed as $\epsilon(\omega) = \epsilon_0\epsilon_\infty + \epsilon_0\chi_e(\omega)$, where ϵ_∞ represents the high-frequency relative permittivity and $\chi_e(\omega)$ is the electric susceptibility. Following the CCPR model [26], $\chi_e(\omega)$ can be expanded as a

sum of complex-conjugate pole pairs

$$\chi_e(\omega) = \sum_{r=1}^{R} \left(\frac{c_r}{j\omega - a_r} + \frac{c_r^*}{j\omega - a_r^*} \right), \tag{6.1}$$

where R is the number of poles, and a_r and c_r are the model's parameters that can be obtained from data fitting. The magnetic permeability $\mu(\omega)$ can sometimes exhibit a similar dispersive behavior, modeled as $\mu_0\mu_\infty + \mu_0\chi_m(\omega)$, where

$$\chi_m(\omega) = \sum_{s=1}^{S} \left(\frac{d_s}{j\omega - b_s} + \frac{d_s^*}{j\omega - b_s^*} \right), \tag{6.2}$$

with S poles and corresponding parameters b_s and d_s.

6.1.2 Generalized Doubly Dispersive Formulation

The generalized doubly dispersive formulation is derived by introducing dual ADEs within the modular implementation of the DGTD method based on the CCPR model introduced in [29]. With the inclusion of the dual auxiliary fields, $\boldsymbol{\mathcal{S}}$ and $\boldsymbol{\mathcal{Q}}$, the full set of governing equations is presented in Figure 18.

6.1.3 The Discontinuous Galerkin Method

The DGTD method discretizes the spatial domain Ω_h into K non-overlapping elements Ω_h^k, bounded by $\partial\Omega_h^k$, and approximates the solution using piecewise polynomial functions. This

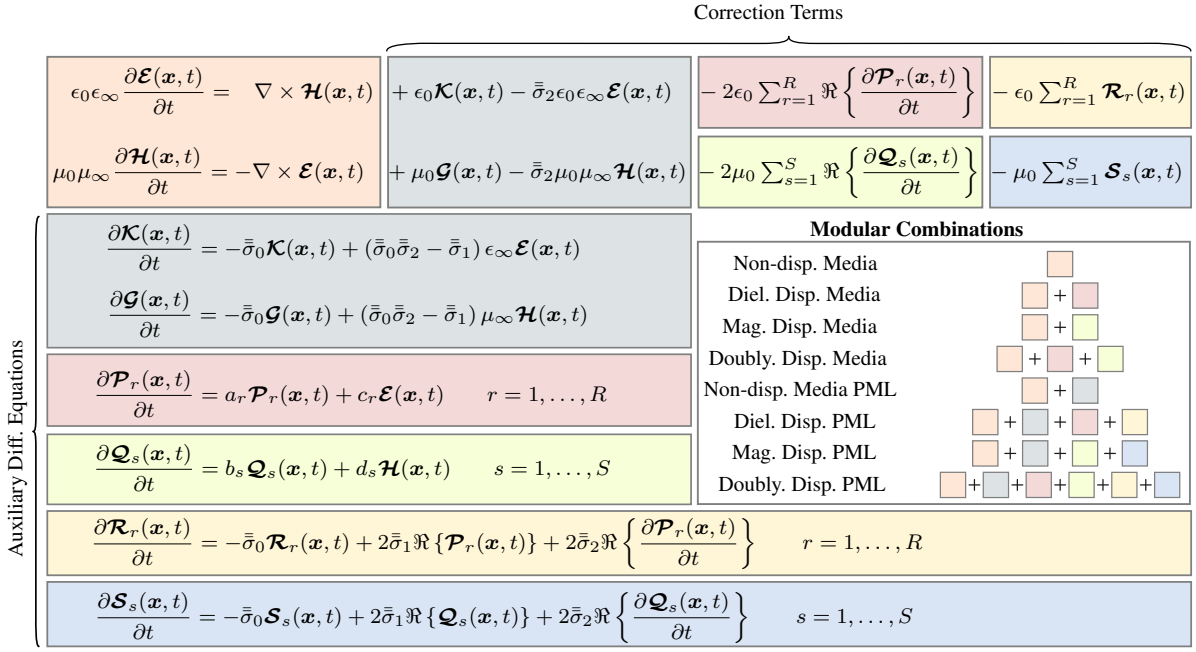

Figure 18 – Illustration of the modular implementation of Maxwell's equations containing doubly dispersive media truncated by PML.

approach allows us to write the weak form of the generalized doubly dispersive formulation with upwind numerical flux in bilinear form as

$$\epsilon_0\left(\phi_h, \epsilon_\infty \frac{\partial \boldsymbol{\mathcal{E}}_h}{\partial t}\right)_{\Omega_h} = (\phi_h, \nabla \times \boldsymbol{\mathcal{H}}_h)_{\Omega_h} + \epsilon_0(\phi_h, \boldsymbol{\mathcal{K}}_h)_{\Omega_h} - \epsilon_0(\phi_h, \bar{\bar{\sigma}}_2 \epsilon_\infty \boldsymbol{\mathcal{E}}_h)_{\Omega_h} - 2\epsilon_0 \sum_{r=1}^{R} \left(\phi_h, \Re\left\{\frac{\partial \boldsymbol{\mathcal{P}}_{h,r}}{\partial t}\right\}\right)_{\Omega_h} - \epsilon_0 \sum_{r=1}^{R} (\phi_h, \boldsymbol{\mathcal{R}}_{h,r})_{\Omega_h} + \sum_{k=1}^{K} \left(\phi_h, \frac{-\hat{n} \times \eta_0 \eta_\infty^+ [\boldsymbol{\mathcal{H}}_h] + \hat{n} \times \hat{n} \times [\boldsymbol{\mathcal{E}}_h]}{2\{\{\eta_0 \eta_\infty\}\}}\right)_{\partial \Omega_h^k}, \tag{6.3}$$

$$\mu_0\left(\phi_h, \mu_\infty \frac{\partial \boldsymbol{\mathcal{H}}_h}{\partial t}\right)_{\Omega_h} = (\phi_h, -\nabla \times \boldsymbol{\mathcal{E}}_h)_{\Omega_h} + \mu_0(\phi_h, \boldsymbol{\mathcal{G}}_h)_{\Omega_h} - \mu_0(\phi_h, \bar{\bar{\sigma}}_2 \mu_\infty \boldsymbol{\mathcal{H}}_h)_{\Omega_h} - 2\mu_0 \sum_{s=1}^{S} \left(\phi_h, \Re\left\{\frac{\partial \boldsymbol{\mathcal{Q}}_{h,s}}{\partial t}\right\}\right)_{\Omega_h} - \mu_0 \sum_{s=1}^{S} (\phi_h, \boldsymbol{\mathcal{S}}_{h,s})_{\Omega_h} + \sum_{k=1}^{K} \left(\phi_h, \frac{\{\{\eta_0 \eta_\infty\}\}}{2}\left[\hat{n} \times \frac{[\boldsymbol{\mathcal{E}}_h]}{\eta_0 \eta_\infty^+} + \hat{n} \times \hat{n} \times [\boldsymbol{\mathcal{H}}_h]\right]\right)_{\partial \Omega_h^k}, \tag{6.4}$$

$$\left(\phi_h, \frac{\partial \boldsymbol{\mathcal{K}}_h}{\partial t}\right)_{\Omega_h} = -(\phi_h, \bar{\bar{\sigma}}_0 \boldsymbol{\mathcal{K}}_h)_{\Omega_h} + (\phi_h, (\bar{\bar{\sigma}}_0 \bar{\bar{\sigma}}_2 - \bar{\bar{\sigma}}_1)\, \epsilon_\infty \boldsymbol{\mathcal{E}}_h)_{\Omega_h}, \tag{6.5}$$

$$\left(\phi_h, \frac{\partial \boldsymbol{\mathcal{G}}_h}{\partial t}\right)_{\Omega_h} = -(\phi_h, \bar{\bar{\sigma}}_0 \boldsymbol{\mathcal{G}}_h)_{\Omega_h} + (\phi_h, (\bar{\bar{\sigma}}_0 \bar{\bar{\sigma}}_2 - \bar{\bar{\sigma}}_1)\, \mu_\infty \boldsymbol{\mathcal{H}}_h)_{\Omega_h}, \tag{6.6}$$

$$\left(\phi_h, \frac{\partial \boldsymbol{\mathcal{P}}_{h,r}}{\partial t}\right)_{\Omega_h} = (\phi_h, a_r \boldsymbol{\mathcal{P}}_{h,r})_{\Omega_h} + (\phi_h, c_r \boldsymbol{\mathcal{E}}_h)_{\Omega_h}, \tag{6.7}$$

$$\left(\phi_h, \frac{\partial \boldsymbol{\mathcal{Q}}_{h,s}}{\partial t}\right)_{\Omega_h} = (\phi_h, b_s \boldsymbol{\mathcal{Q}}_{h,s})_{\Omega_h} + (\phi_h, d_s \boldsymbol{\mathcal{H}}_h)_{\Omega_h}, \tag{6.8}$$

$$\left(\phi_h, \frac{\partial \boldsymbol{\mathcal{R}}_{h,r}}{\partial t}\right)_{\Omega_h} = 2\left(\phi_h, \bar{\bar{\sigma}}_2 \Re\left\{\frac{\partial \boldsymbol{\mathcal{P}}_{h,r}}{\partial t}\right\}\right)_{\Omega_h} - (\phi_h, \bar{\bar{\sigma}}_0 \boldsymbol{\mathcal{R}}_{h,r})_{\Omega_h} + 2(\phi_h, \bar{\bar{\sigma}}_1 \Re\{\boldsymbol{\mathcal{P}}_{h,r}\})_{\Omega_h}, \tag{6.9}$$

$$\left(\phi_h, \frac{\partial \boldsymbol{\mathcal{S}}_{h,s}}{\partial t}\right)_{\Omega_h} = 2\left(\phi_h, \bar{\bar{\sigma}}_2 \Re\left\{\frac{\partial \boldsymbol{\mathcal{Q}}_{h,s}}{\partial t}\right\}\right)_{\Omega_h} - (\phi_h, \bar{\bar{\sigma}}_0 \boldsymbol{\mathcal{S}}_{h,s})_{\Omega_h} + 2(\phi_h, \bar{\bar{\sigma}}_1 \Re\{\boldsymbol{\mathcal{Q}}_{h,s}\})_{\Omega_h}, \tag{6.10}$$

where $\boldsymbol{\mathcal{E}}_h, \boldsymbol{\mathcal{H}}_h, \boldsymbol{\mathcal{P}}_h, \boldsymbol{\mathcal{Q}}_h, \boldsymbol{\mathcal{R}}_h, \boldsymbol{\mathcal{S}}_h, \boldsymbol{\mathcal{G}}_h, \boldsymbol{\mathcal{K}}_h \in (V_h)^3$ and $\phi_h \in V_h$ with $V_h = \bigoplus_{k=1}^{K} P_N(\Omega^k)$ being the space of piecewise polynomial functions, $[q] = q^- - q^+$, $\{\{q\}\} = (q^- + q^+)/2$, and $\eta = \sqrt{\mu/\epsilon}$. Once the weak form is established, the solution can be obtained using the standard DGTD steps detailed in [6].

6.2 Numerical Results

The proposed formulation is validated by analyzing scattering problems assuming of an incident TMz plane wave given by

$$\boldsymbol{\mathcal{E}}_{\text{inc}}(\boldsymbol{x}, t) = \hat{\boldsymbol{z}}\, g(t - \sqrt{\epsilon_0 \mu_0}\, \hat{\boldsymbol{x}} \cdot \boldsymbol{x}), \tag{6.11}$$

$$\boldsymbol{\mathcal{H}}_{\text{inc}}(\boldsymbol{x}, t) = \sqrt{\frac{\epsilon_0}{\mu_0}} \hat{\boldsymbol{x}} \times \boldsymbol{\mathcal{E}}_{\text{inc}}(\boldsymbol{x}, t), \tag{6.12}$$

with $g(t)$ being the cosine-modulated Gaussian waveform

$$g(t) = \cos(2\pi f_c (t - t_0)) \exp\left(-(t - t_0)^2 / \tau^2\right), \tag{6.13}$$

where f_c denotes the center frequency, τ characterizes the time constant, and t_0 represents a time delay. To analyze a frequency band from 100 MHz to 500 MHz, f_c was set to 300 MHz and τ was set to $1.25/f_c$ seconds. To ensure that the electromagnetic fields were zero at both the start and end of the simulation, a time delay t_0 of 7τ was applied, and the fields were simulated for a total duration of 20τ in all cases. The time step was chosen according to [6]. To model the dispersive media, we employed the doubly dispersive model described in [51] with relative permittivity and relative permeability responses shown in Figure 19.

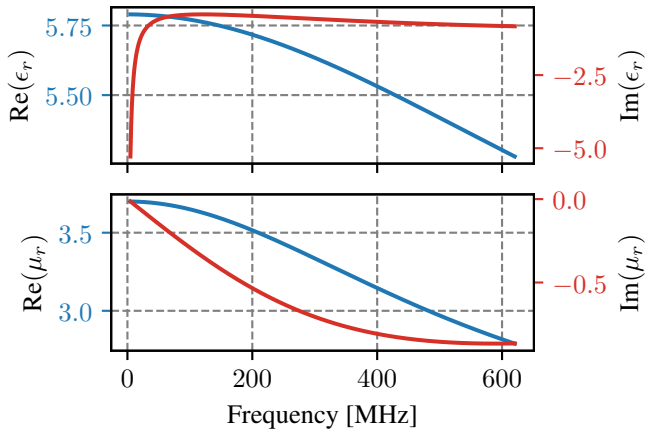

Figure 19 – Relative permittivity and relative permeability of the analyzed material.

A second-degree polynomial defines the PML profile in all simulations. The PML is designed to achieve an attenuation of the reflected field of about 70 dB.

The errors are analyzed using the relative L2 error norm [29] and the normalized error, defined as $|\boldsymbol{\mathcal{E}}^n - \boldsymbol{\mathcal{E}}^a|/\boldsymbol{\mathcal{E}}_0$, where a refers to the analytical and n to the numerical values, and $\boldsymbol{\mathcal{E}}_0$ is the amplitude of the incident electric field.

6.2.1 Validation: Doubly Dispersive Slab

We first study the scattering of the TMz plane wave by a doubly dispersive slab truncated by a doubly dispersive PML as shown in Figure 20.

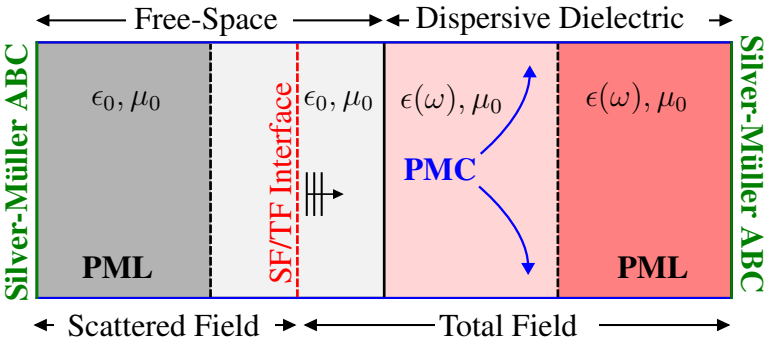

Figure 20 – Meridian cut view of the slab's two-dimensional validation case.

The computational domain was sized at $3.0\lambda_c \times 2.0\lambda_c$, where λ_c is the wavelength at the center frequency f_c. The PML had a width of $0.5\lambda_c$, and the doubly dispersive slab was $1.0\lambda_c$ wide. The TF/SF interface was positioned at the center of the SFR, excluding the PML. To evaluate convergence, a coarse mesh with $1/6\lambda_c$ resolution (570 elements) and a refined mesh with $1/12\lambda_c$ resolution (2070 elements) were tested. Figure 21 shows the L2 error compared to the analytical solution while Figure 22 shows the convergence of the solution with respect to the number of elements at 300 MHz. Compared to the results in [29], it is evident that using a static conductivity significantly increases and saturates the error at low frequencies, which was also observed in [61]. This occurs because the model employs the term $\sigma/(j\omega)$ [51], where the static conductivity σ leads to large contributions at low frequencies as ω approaches zero. In general, more complex doubly dispersive materials require both higher-order schemes and denser meshes to achieve the same error levels as those observed in materials with only electric dispersion. Nevertheless, the convergence rate remains closely the same.

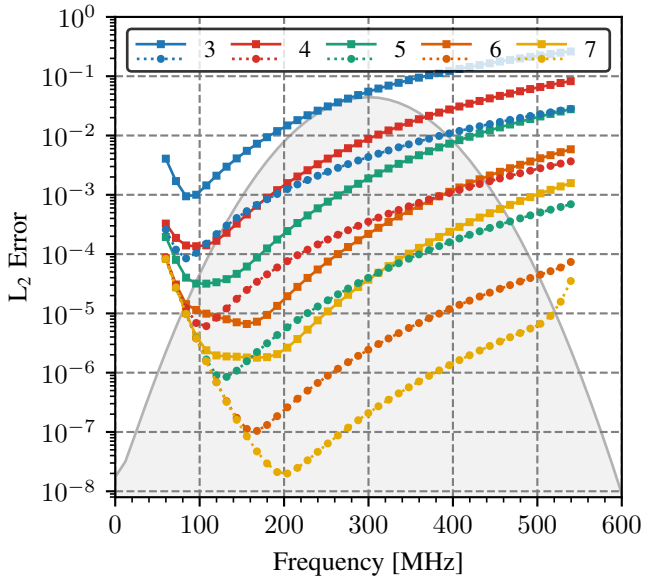

Figure 21 – L2 error of the electric field varying the order of the elements. The gray area represents the frequency spectrum of the incident field.

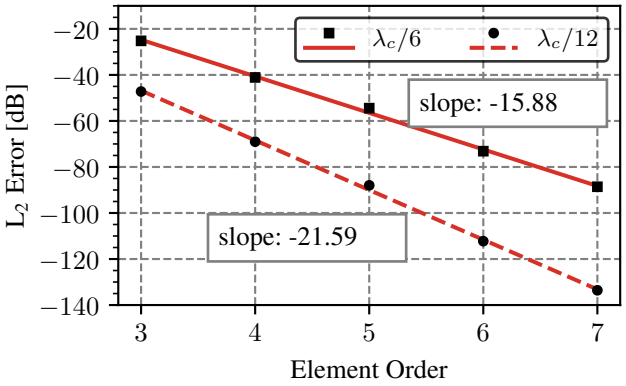

Figure 22 – Convergence rate of the L2 error varying element orders at 300 MHz.

6.2.2 Doubly Dispersive Cylinder

This section aims to illustrate how curvilinear elements can further decrease the modeling error for problems involving doubly dispersive curved objects by analyzing the scattering of a plane wave by a doubly dispersive circular cylinder, as illustrated in Figure 23. The

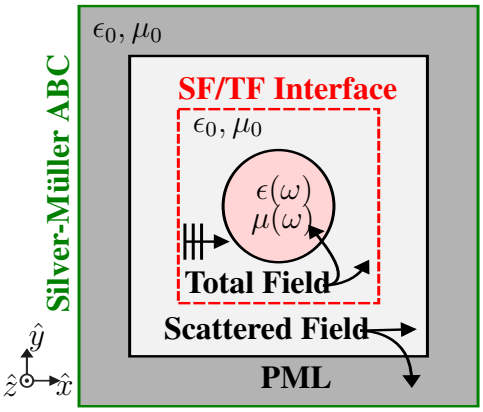

Figure 23 – Illustration of the cylinder's two-dimensional case study.

computational domain has dimensions of $2.0\lambda_c \times 2.0\lambda_c$, with a PML width of $0.25\lambda_c$ and a cylinder radius of $0.25\lambda_c$. Curvilinear elements were specifically used along the cylinder boundary. The performance of the curvilinear DGTD was compared against DGTD with linear elements. Figure 24 shows the time-domain response of the electric field using a mesh density of $1/10\lambda_c$ corresponding to 374 elements. The electric field error at $t = 7\tau$ along the line $y = 0$, highlighted by the red line in Figure 24, is shown in Figure 25. The time-dependent error at the center of the cylinder is displayed in Figure 26. The analytical time-domain solution was based on the frequency-domain series solution [50], as in [29], using 50 terms. The results show that the curvilinear DGTD method achieves an error reduction of about 20 dB compared to the standard DGTD approach in this case. This improvement highlights the enhanced accuracy and efficiency of the proposed curvilinear DGTD method in modeling curved geometries while preserving computational performance. Notably, the computational cost of employing a small

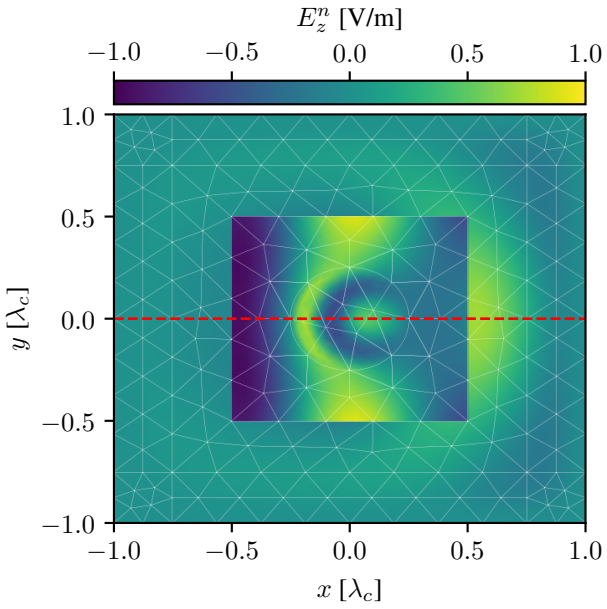

Figure 24 – Electric field distribution at $t = 7\tau$ with 4th order elements.

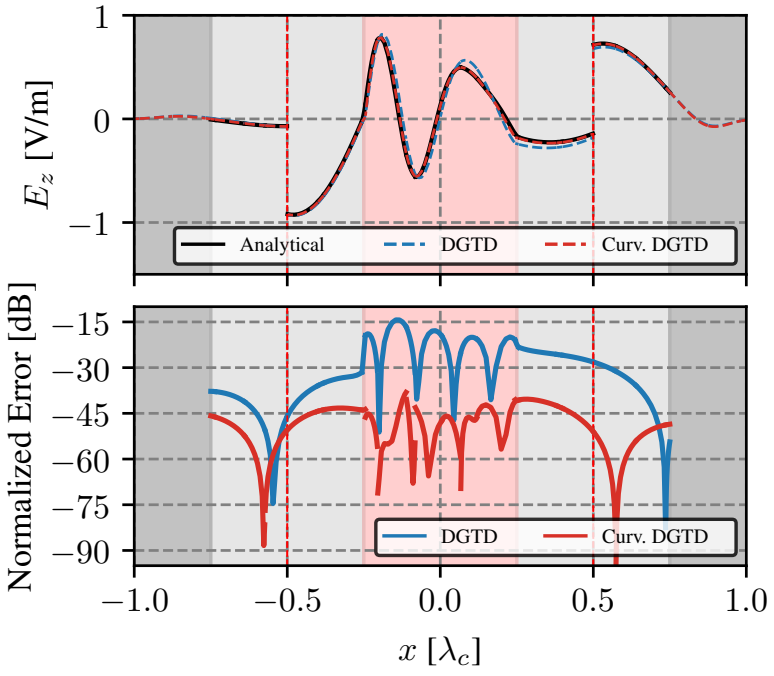

Figure 25 – Electric field at $y = 0$ and $t = 7\tau$.

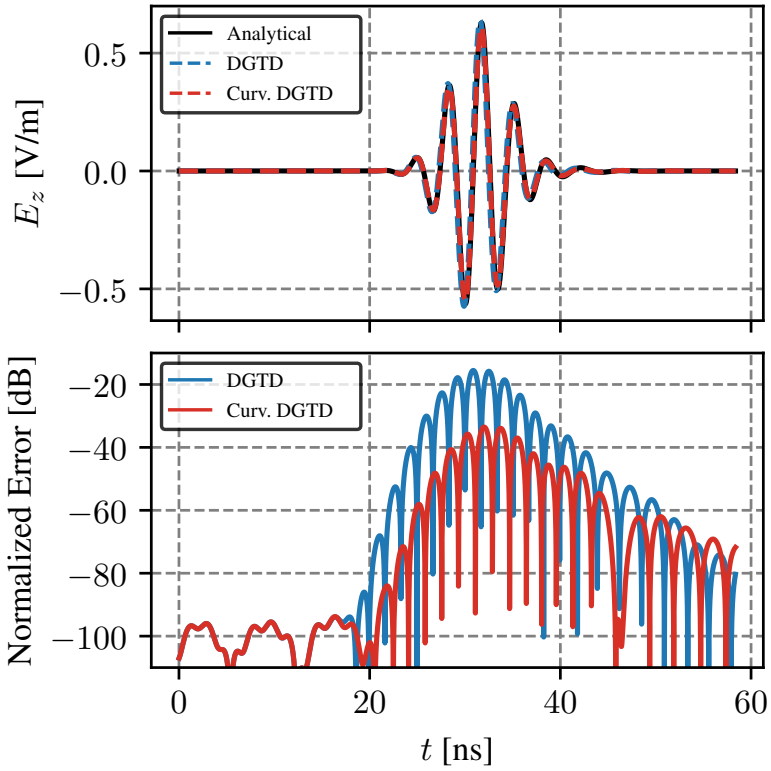

Figure 26 – Electric field observed at the center of the cylinder.

number of curvilinear elements is comparable to either doubling the mesh density or increasing the polynomial order by one degree across all elements.

6.3 Conclusion

A modular DGTD algorithm was extended for modeling general doubly dispersive materials described by very general complex-conjugate pole-residue models. The modular implementation of the algorithm allows for the simulation of open domain problems by simply adding suitable correction terms that incorporate the PML absorbing boundary condition. The algorithm also integrates curvilinear elements to improve the accuracy over standard DGTD for modeling curved geometries without compromising the computational efficiency.

CHAPTER 7

IMEX Time-Stepping for DGTD in Doubly Dispersive Media

The simulation of electromagnetic wave propagation in complex media, particularly those with frequency-dependent permittivity and permeability (doubly dispersive media), presents significant computational challenges. The DGTD method is widely recognized as a robust technique for addressing these challenges by effectively handling complex geometries and material modeling doubly dispersive media as seen in Chapter 6. This is made possible through its flexibility in mesh generation and its ability to naturally incorporate varying polynomial orders for spatial discretization [6]. While dispersive dielectric materials have been extensively studied, the investigation of doubly dispersive materials, especially using the IMEX integration scheme, remains relatively unexplored [62].

This work models doubly dispersive materials using CCPR representations, which are readily incorporated into the simulation via the ADE framework. Applying the DGTD spatial discretization to Maxwell's equations—accounting for the coupling with these ADEs and incorporating domain truncation via absorbing boundary conditions such as the dispersive uniaxial PML detailed in Chapter 6—yields a large, coupled system of ODEs in time. This ODE system describes the evolution of the basis function coefficients associated with the electromagnetic fields as well as the auxiliary variables capturing the material's polarization/magnetization dynamics and the absorbing layer behavior.

A key challenge in solving this system of ODEs lies in numerical stiffness. The auxiliary equations describing the material response or the PML often involve relaxation times or resonant frequencies that introduce *fast time scales*—rapidly evolving dynamics that can dominate the numerical behavior of the system. These fast dynamics demand very small time steps when using standard explicit time integration schemes (such as Leapfrog or explicit RK methods), purely for stability reasons rather than accuracy. Moreover, resolving fine-scale wave phenomena or steep field gradients in dispersive and absorbing media typically requires *fine spatial discretization*,

which further reduces the allowable time step due to the CFL condition. Conversely, fully implicit methods can handle stiffness unconditionally, but require solving large linear systems at every time step, which can be computationally prohibitive given the size and complexity of typical DGTD systems.

IMEX time integration schemes offer a compelling compromise. They partition the ODE system into stiff and non-stiff components, applying a stable implicit method to the former and an efficient explicit method to the latter. This chapter details how a specific fourth-order IMEX RK scheme can be effectively applied to the semi-discrete DGTD equations for doubly dispersive media including dispersive PMLs, enabling stable and efficient simulations.

7.1 Semi-Discrete DGTD System for Doubly Dispersive Media

Applying the DGTD spatial discretization procedure to the governing equations—which include Maxwell's equations coupled with the ADEs for doubly dispersive media and dispersive PML for domain truncation (schematically represented in Figure 18)—transforms the problem into a system of ODEs. This procedure involves projecting the fields onto local polynomial basis functions within each element k, integrating by parts, and introducing numerical fluxes at element faces f. The resulting ODE system governs the evolution of the time-dependent coefficients (degrees of freedom) for these basis functions.

Let $\vec{\boldsymbol{e}}_h^k$ and $\vec{\boldsymbol{h}}_h^k$ represent the vectors containing the coefficients for the electric and magnetic field components, respectively. Additional auxiliary variables are required to model both the material dispersion (using a CCPR model) and the PML absorption:

- $\vec{\boldsymbol{p}}_{h,r}^k$ $(r = 1, \ldots, R)$ and $\vec{\boldsymbol{q}}_{h,s}^k$ $(s = 1, \ldots, S)$ represent the electric and magnetic polarization/magnetization contributions capturing material dispersion.
- $\vec{\boldsymbol{k}}_h^k$ and $\vec{\boldsymbol{g}}_h^k$ are auxiliary variables inherent to the uniaxial PML formulation used for wave absorption.
- $\vec{\boldsymbol{r}}_{h,r}^k$ and $\vec{\boldsymbol{s}}_{h,s}^k$ arise specifically from the interaction between the material dispersion ADEs (for $\vec{\boldsymbol{p}}_h^k$, $\vec{\boldsymbol{q}}_h^k$) and the uniaxial PML mechanism when dispersive materials are present within the PML region itself.

The resulting semi-discrete system couples these coefficient vectors and takes the form

$$\epsilon_0\epsilon_\infty^k \frac{d\vec{\boldsymbol{e}}_h^k}{dt} = (M^k)^{-1}\left(\boldsymbol{S}^k \times \vec{\boldsymbol{h}}_h^k + \sum_f F_f^k \cdot \left(\hat{\boldsymbol{n}} \cdot \left[\vec{\boldsymbol{\mathcal{F}}}_E^k - \vec{\boldsymbol{\mathcal{F}}}_E^*\right]\right)\right) + \epsilon_0 \vec{\boldsymbol{k}}_h^k - \bar{\bar{\sigma}}_2\epsilon_0\epsilon_\infty^k \vec{\boldsymbol{e}}_h^k - 2\epsilon_0 \sum_{r=1}^{R} \Re\left\{\frac{d\vec{\boldsymbol{p}}_{h,r}^k}{dt}\right\} - \epsilon_0 \sum_{r=1}^{R} \vec{\boldsymbol{r}}_{h,r}^k \tag{7.1}$$

$$\mu_0\mu_\infty^k \frac{d\vec{\boldsymbol{h}}_h^k}{dt} = (M^k)^{-1}\left(-\boldsymbol{S}^k \times \vec{\boldsymbol{e}}_h^k + \sum_f F_f^k \cdot \left(\hat{\boldsymbol{n}} \cdot \left[\vec{\boldsymbol{\mathcal{F}}}_H^k - \vec{\boldsymbol{\mathcal{F}}}_H^*\right]\right)\right) + \mu_0 \vec{\boldsymbol{g}}_h^k - \bar{\bar{\sigma}}_2\mu_0\mu_\infty^k \vec{\boldsymbol{h}}_h^k - 2\mu_0 \sum_{s=1}^{S} \Re\left\{\frac{d\vec{\boldsymbol{q}}_{h,s}^k}{dt}\right\} - \mu_0 \sum_{s=1}^{S} \vec{\boldsymbol{s}}_{h,s}^k \tag{7.2}$$

$$\frac{d\vec{\boldsymbol{k}}_h^k}{dt} = -\bar{\bar{\sigma}}_0 \vec{\boldsymbol{k}}_h^k + \left(\bar{\bar{\sigma}}_0\bar{\bar{\sigma}}_2 - \bar{\bar{\sigma}}_1\right)\epsilon_\infty^k \vec{\boldsymbol{e}}_h^k \tag{7.3}$$

$$\frac{d\vec{\boldsymbol{g}}_h^k}{dt} = -\bar{\bar{\sigma}}_0 \vec{\boldsymbol{g}}_h^k + \left(\bar{\bar{\sigma}}_0\bar{\bar{\sigma}}_2 - \bar{\bar{\sigma}}_1\right)\mu_\infty^k \vec{\boldsymbol{h}}_h^k \tag{7.4}$$

$$\frac{d\vec{\boldsymbol{p}}_{h,r}^k}{dt} = a_r \vec{\boldsymbol{p}}_{h,r}^k + c_r\epsilon_\infty^k \vec{\boldsymbol{e}}_h^k \qquad r = 1, \ldots, R \tag{7.5}$$

$$\frac{d\vec{\boldsymbol{r}}_{h,r}^k}{dt} = -\bar{\bar{\sigma}}_0 \vec{\boldsymbol{r}}_{h,r}^k + 2\bar{\bar{\sigma}}_1 \Re\left\{\vec{\boldsymbol{p}}_{h,r}^k\right\} + 2\bar{\bar{\sigma}}_2 \Re\left\{\frac{d\vec{\boldsymbol{p}}_{h,r}^k}{dt}\right\} \qquad r = 1, \ldots, R \tag{7.6}$$

$$\frac{d\vec{\boldsymbol{q}}_{h,s}^k}{dt} = b_s \vec{\boldsymbol{q}}_{h,s}^k + d_s\mu_\infty^k \vec{\boldsymbol{h}}_h^k \qquad s = 1, \ldots, S \tag{7.7}$$

$$\frac{d\vec{\boldsymbol{s}}_{h,s}^k}{dt} = -\bar{\bar{\sigma}}_0 \vec{\boldsymbol{s}}_{h,s}^k + 2\bar{\bar{\sigma}}_1 \Re\left\{\vec{\boldsymbol{q}}_{h,s}^k\right\} + 2\bar{\bar{\sigma}}_2 \Re\left\{\frac{d\vec{\boldsymbol{q}}_{h,s}^k}{dt}\right\} \qquad s = 1, \ldots, S \tag{7.8}$$

In these equations, M^k represents the mass matrix for element k, $\boldsymbol{S}^k$ represents the discrete curl (stiffness) operator, F_f^k contains terms related to face integration, and $\vec{\boldsymbol{\mathcal{F}}}^*$ denotes the numerical flux. The parameters $\bar{\bar{\sigma}}_0, \bar{\bar{\sigma}}_1, \bar{\bar{\sigma}}_2$ define the PML, while a_r, c_r, b_s, d_s are parameters derived from the CCPR material dispersion model. Note that the coupling terms $\vec{\boldsymbol{r}}_{h,r}^k$, $\vec{\boldsymbol{s}}_{h,s}^k$ (and their governing Equations (7.6) and (7.8)) are only non-zero for elements where both PML parameters ($\bar{\bar{\sigma}}_i$) and dispersion (a_r, c_r or b_s, d_s) are active.

Since this system, Equation (7.1) to Equation (7.8), is linear and assuming time-invariant parameters and geometry, it can be written compactly in matrix form as

$$\frac{\partial \vec{q}}{\partial t} = L\vec{q} + \vec{f}(t) \tag{7.9}$$

where $\vec{q}$ is the global state vector containing all degrees of freedom across all elements, L is the large, sparse matrix representing the discretized spatial operators and the coupling terms from

the material and PML models, and $\vec{f}(t)$ represents any time-dependent source terms projected onto the basis functions. The structure of $\vec{q}$ concatenates these coefficient vectors as

$$\vec{q} = \left[e^1_{x,1}, \ldots, e^K_{x,N}, e^1_{y,1}, \ldots, e^K_{y,N}, p^1_{x,1,1}, \ldots, p^K_{x,N,R}, \ldots, s^1_{z,1,1}, \ldots, s^K_{z,N,S}\right]^\intercal \tag{7.10}$$

where K is the total number of elements in the mesh, and N is the number of nodes per element assuming a uniform approximation order across all elements.

7.2 IMEX Time Integration Algorithm

The Implicit-Explicit (IMEX) time integration method, as implemented in Algorithm 4, numerically solves the system of ODEs resulting from the DGTD discretization. This method partitions the system's Degrees of Freedom (DOFs) based on the characteristics of the mesh elements they originate from. DOFs associated with elements considered numerically stiff (e.g., small elements requiring small explicit time steps for stability, or elements containing stiff material models) are assigned to the implicitly treated set ($\mathcal{I}$), while DOFs from non-stiff elements (e.g., larger elements in a coarse region) are assigned to the explicitly treated set ($\mathcal{E}$).

This partitioning of the DOFs naturally leads to a block structure when writing the full semi-discrete system of ODEs

$$\frac{\partial}{\partial t}\begin{bmatrix}\vec{q}_{\mathcal{E}}\\ \vec{q}_{\mathcal{I}}\end{bmatrix} = \begin{bmatrix}L_{\mathcal{E}\mathcal{E}} & L_{\mathcal{E}\mathcal{I}}\\ L_{\mathcal{I}\mathcal{E}} & L_{\mathcal{I}\mathcal{I}}\end{bmatrix}\begin{bmatrix}\vec{q}_{\mathcal{E}}\\ \vec{q}_{\mathcal{I}}\end{bmatrix} + \begin{bmatrix}\vec{f}_{\mathcal{E}}(t)\\ \vec{f}_{\mathcal{I}}(t)\end{bmatrix}, \tag{7.11}$$

where $\vec{q}_{\mathcal{E}}$ and $\vec{q}_{\mathcal{I}}$ are the sub-vectors of the global state vector $\vec{q}$ corresponding to the explicit and implicit partitions, respectively. The matrix L is partitioned conformally, where $L_{\mathcal{E}\mathcal{E}}$ and $L_{\mathcal{I}\mathcal{I}}$ represent the internal couplings within the explicit and implicit sets, while $L_{\mathcal{E}\mathcal{I}}$ and $L_{\mathcal{I}\mathcal{E}}$ describe the cross-couplings between the two sets. Similarly, $\vec{f}_{\mathcal{E}}(t)$ and $\vec{f}_{\mathcal{I}}(t)$ are the corresponding partitions of the source vector $\vec{f}(t)$. The IMEX algorithm then proceeds by applying different Runge-Kutta update rules to the equations governing $\vec{q}_{\mathcal{E}}$ (first row) and $\vec{q}_{\mathcal{I}}$ (second row).

The time integration from $\vec{q}^{\,n}$ at t_n to $\vec{q}^{\,n+1}$ at $t_{n+1} = t_n + \Delta t$ uses an additive RK method. Such schemes are characterized by coefficients A (explicit), $\tilde{A}$ (implicit), $\vec{b}$ (final weights), and $\vec{c}$ (stage times); the specific values used here are listed in Appendix C. The key aspect of applying this scheme within the IMEX framework lies in how the stage derivatives are computed separately for the explicit ($\mathcal{E}$) and implicit ($\mathcal{I}$) parts of the system.

For each stage $i = 1, \ldots, s$, the algorithm computes stage derivatives $\vec{k}^{(i)} = [\vec{k}^{(i)}_{\mathcal{E}}; \vec{k}^{(i)}_{\mathcal{I}}]$. This begins by calculating intermediate state values $\vec{q}^{(i)}_{\mathcal{E}}$ and $\vec{q}^{(i)}_{\mathcal{I}}$ using the results from previous

stages ($j < i$)

$$\vec{q}_{\mathcal{E}}^{(i)} = \vec{q}_{\mathcal{E}}^{n} + \Delta t \sum_{j=1}^{i-1} A_{ij} \vec{k}_{\mathcal{E}}^{(j)}, \tag{7.12}$$

$$\vec{q}_{\mathcal{I}}^{(i)} = \vec{q}_{\mathcal{I}}^{n} + \Delta t \sum_{j=1}^{i-1} \tilde{A}_{ij} \vec{k}_{\mathcal{I}}^{(j)}. \tag{7.13}$$

These intermediate values are then used to evaluate the right-hand side of Equation (7.11) at the stage time $t^{(i)} = t_n + c_i \Delta t$.

The explicit part of the stage derivative, $\vec{k}_{\mathcal{E}}^{(i)}$, corresponds directly to the first block row of Equation (7.11), evaluated using the intermediate states

$$\vec{k}_{\mathcal{E}}^{(i)} = \underbrace{L_{\mathcal{E}\mathcal{E}} \vec{q}_{\mathcal{E}}^{(i)} + L_{\mathcal{E}\mathcal{I}} \vec{q}_{\mathcal{I}}^{(i)} + \vec{f}_{\mathcal{E}}(t^{(i)})}_{\text{Derivative calculation for } \mathcal{E} \text{ variables}}. \tag{7.14}$$

This calculation uses only already computed values and is fully explicit.

The implicit part of the stage derivative, $\vec{k}_{\mathcal{I}}^{(i)}$, corresponds to the second block row of Equation (7.11). An implicit step is required here. First, the right-hand side for the implicit variables is computed based on the intermediate state

$$\vec{r}^{(i)} = \underbrace{L_{\mathcal{I}\mathcal{E}} \vec{q}_{\mathcal{E}}^{(i)} + L_{\mathcal{I}\mathcal{I}} \vec{q}_{\mathcal{I}}^{(i)} + \vec{f}_{\mathcal{I}}(t^{(i)})}_{\text{Derivative calculation for } \mathcal{I} \text{ variables}}. \tag{7.15}$$

The implicitness arises from the diagonal coefficient $\tilde{A}_{ii}$ of the implicit Runge-Kutta method. The stage derivative $\vec{k}_{\mathcal{I}}^{(i)}$ is the solution to the following linear system

$$\vec{k}_{\mathcal{I}}^{(i)} = \Delta t \tilde{A}_{ii} \left(L_{\mathcal{I}\mathcal{I}} \vec{k}_{\mathcal{I}}^{(i)} \right) + \vec{r}^{(i)} \quad \Longrightarrow \quad (I - \Delta t \tilde{A}_{ii} L_{\mathcal{I}\mathcal{I}}) \vec{k}_{\mathcal{I}}^{(i)} = \vec{r}^{(i)}. \tag{7.16}$$

The term $L_{\mathcal{I}\mathcal{E}} \vec{q}_{\mathcal{E}}^{(i)} + \vec{f}_{\mathcal{I}}(t^{(i)})$ from $\vec{r}^{(i)}$ acts like an explicit source term for this solve. This linear system involves only the matrix block $L_{\mathcal{I}\mathcal{I}}$, making the solve efficient compared to a fully implicit method.

After completing all s stages, the final solution $\vec{q}^{n+1}$ at time t_{n+1} is obtained by combining the initial state $\vec{q}^{n}$ with the weighted sum of the stage derivatives

$$\vec{q}_{\mathcal{E}}^{n+1} = \vec{q}_{\mathcal{E}}^{n} + \Delta t \sum_{i=1}^{s} b_i \vec{k}_{\mathcal{E}}^{(i)} \tag{7.17}$$

$$\vec{q}_{\mathcal{I}}^{n+1} = \vec{q}_{\mathcal{I}}^{n} + \Delta t \sum_{i=1}^{s} b_i \vec{k}_{\mathcal{I}}^{(i)}. \tag{7.18}$$

This IMEX approach effectively uses an explicit RK update rule for the $\mathcal{E}$ variables based on their governing equation (first row of Equation (7.11)), and an implicit RK update rule for the $\mathcal{I}$ variables based on their governing equation (second row), but structures the implicit solve to only involve the $L_{\mathcal{I}\mathcal{I}}$ block.

Finally, these updated sub-vectors are concatenated to form the complete state vector for the next time step

$$\vec{q}^{n+1} = \begin{bmatrix} \vec{q}_{\mathcal{E}}^{n+1} \\ \vec{q}_{\mathcal{I}}^{n+1} \end{bmatrix}. \tag{7.19}$$

Algorithm 4: Generalized IMEX Step with Source Term

Input: q, L, $f(t)$, Δt, `mask_implicit`

Output: q_{next}

$s \leftarrow$ number of stages

$\mathcal{E} \leftarrow \texttt{where}(\texttt{mask\_implicit} = \texttt{false})$

$\mathcal{I} \leftarrow \texttt{where}(\texttt{mask\_implicit} = \texttt{true})$

$q_{\mathcal{E}}, q_{\mathcal{I}} \leftarrow q[\mathcal{E}], q[\mathcal{I}]$

$L_{\mathcal{E}\mathcal{E}}, L_{\mathcal{E}\mathcal{I}}, L_{\mathcal{I}\mathcal{E}}, L_{\mathcal{I}\mathcal{I}} \leftarrow L[\mathcal{E},\mathcal{E}], L[\mathcal{E},\mathcal{I}], L[\mathcal{I},\mathcal{E}], L[\mathcal{I},\mathcal{I}]$ `// Can be cached`

for $i \leftarrow 1$ **to** s **do**

  $t^{(i)} \leftarrow t + c_i \cdot \Delta t$

  `// Compute intermediate states`

  $q_{\mathcal{E}}^{(i)} \leftarrow q_{\mathcal{E}} + \Delta t \cdot \sum_{j=1}^{i-1} A_{ij} \cdot k_{\mathcal{E}}^{(j)}$

  $q_{\mathcal{I}}^{(i)} \leftarrow q_{\mathcal{I}} + \Delta t \cdot \sum_{j=1}^{i-1} \tilde{A}_{ij} \cdot k_{\mathcal{I}}^{(j)}$

  `// Evaluate right-hand side`

  $f_{\mathcal{E}}^{(i)} \leftarrow f(t^{(i)})[\mathcal{E}]$

  $f_{\mathcal{I}}^{(i)} \leftarrow f(t^{(i)})[\mathcal{I}]$

  `// Explicit stage`

  $k_{\mathcal{E}}^{(i)} \leftarrow L_{\mathcal{E}\mathcal{E}} q_{\mathcal{E}}^{(i)} + L_{\mathcal{E}\mathcal{I}} q_{\mathcal{I}}^{(i)} + f_{\mathcal{E}}^{(i)}$

  `// Implicit stage`

  $r \leftarrow L_{\mathcal{I}\mathcal{E}} q_{\mathcal{E}}^{(i)} + L_{\mathcal{I}\mathcal{I}} q_{\mathcal{I}}^{(i)} + f_{\mathcal{I}}^{(i)}$

  $k_{\mathcal{I}}^{(i)} \leftarrow \texttt{solve}\left(I - \Delta t \cdot \tilde{A}_{ii} L_{\mathcal{I}\mathcal{I}}, r\right)$

$q_{\mathcal{E}}^{+} \leftarrow q_{\mathcal{E}} + \Delta t \cdot \sum_{i=1}^{s} b_i \cdot k_{\mathcal{E}}^{(i)}$

$q_{\mathcal{I}}^{+} \leftarrow q_{\mathcal{I}} + \Delta t \cdot \sum_{i=1}^{s} \tilde{b}_i \cdot k_{\mathcal{I}}^{(i)}$

$q_{\text{next}}[\mathcal{E}] \leftarrow q_{\mathcal{E}}^{+}, \quad q_{\text{next}}[\mathcal{I}] \leftarrow q_{\mathcal{I}}^{+}$

return q_{next}

7.3 Numerical Results

This study investigates the numerical simulation of electromagnetic fields within a two-dimensional cavity bounded by PEC walls. It focuses on the evolution of the fundamental

Transverse Magnetic (TM) mode. The initial condition is set to a pure TM_{11} spatial distribution for the electric field, specifically

$$\boldsymbol{\mathcal{E}}_z(\boldsymbol{x}, t=0) = E_0 \sin\left(\frac{\pi x}{L_x}\right) \sin\left(\frac{\pi y}{L_y}\right), \tag{7.20}$$

with zero initial magnetic fields ($\boldsymbol{\mathcal{H}}_x(\boldsymbol{x}, 0) = \boldsymbol{\mathcal{H}}_y(\boldsymbol{x}, 0) = 0$), where L_x and L_y are the cavity dimensions. For an ideal lossless cavity, the analytical solution describes a standing wave oscillating harmonically in time

$$\boldsymbol{\mathcal{E}}_z(\boldsymbol{x}, t) = E_0 \sin\left(\frac{\pi x}{L_x}\right) \sin\left(\frac{\pi y}{L_y}\right) \cos(\omega_{11} t), \tag{7.21}$$

where the resonant angular frequency ω_{11} is given by

$$\omega_{11} = c\pi \sqrt{\left(\frac{1}{L_x}\right)^2 + \left(\frac{1}{L_y}\right)^2}. \tag{7.22}$$

Here, c is the speed of light and E_0 is the initial amplitude. The primary goal is to compare and contrast the performance (in terms of accuracy against the analytical solution, stability, and computational efficiency) of various time-integration schemes applied to Maxwell's equations, including fully explicit, fully implicit, and IMEX methods, using this well-defined test case.

The simulation geometry is a $2\,\mathrm{m} \times 2\,\mathrm{m}$ square cavity ($L_x = L_y = 2\,\mathrm{m}$). The simulation time spans three-halves a period ($3T_{11}/2$) of the TM_{11} resonant mode. A two-region mesh was employed for spatial discretization, featuring a refined zone in the interior surrounded by a coarser zone near the boundaries, illustrated in Figure 27. Only the upwind numerical flux was considered.

The time step size, Δt, for the explicit time integration scheme was determined based on the stability criterion adopted in [6]. This criterion relates Δt to the mesh geometry and the polynomial order N used for the spatial approximation. Specifically, it is calculated using the minimum inscribed radius among all mesh elements, $h_{min} = \min_K r_{in,K}$, and the minimum spacing between the $N+1$ Gauss-Lobatto nodes on the reference interval $[-1, 1]$, denoted as $\Delta\xi_{min,N}$. The formula used is:

$$\Delta t = C \cdot \frac{h_{min} \cdot \Delta\xi_{min,N}}{c} \tag{7.23}$$

where the constant is $C = 2/3$. The minimum nodal spacing $\Delta\xi_{min,N}$ implicitly incorporates the dependence on the polynomial order N.

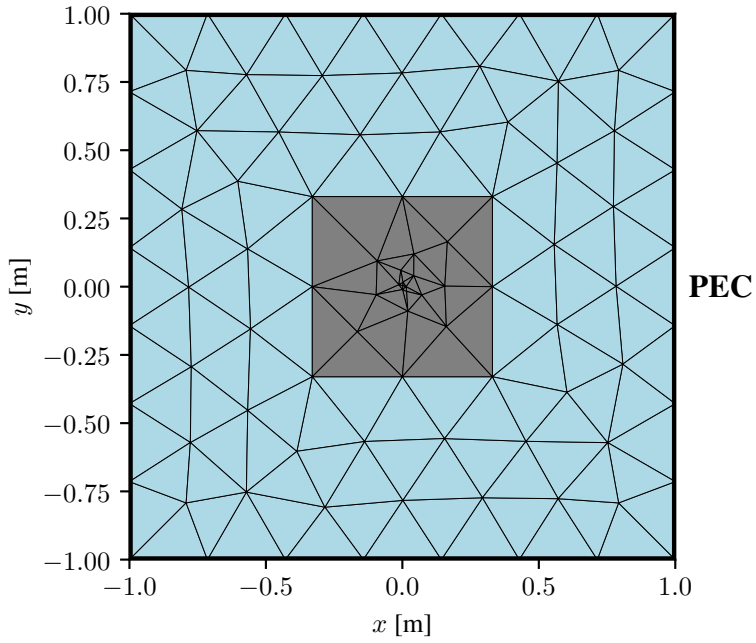

Figure 27 – Representation of the case study geometry and the generated mesh.

Representing the system of ODEs in the form given by Equation (7.9) allows for a stability analysis based on the eigenvalues of the matrix L. The eigenvalues computed for this problem are displayed in the complex plane in Figure 28. To assess stability for an explicit time integration scheme, these eigenvalues (λ) must satisfy the condition that $\lambda\Delta t$ lies within the method's absolute stability region. Consequently, Figure 28 also shows the stability region for the chosen 4th-order, 6-stage RK method (in red) for reference, whose coefficients are provided in Appendix C.

The structure of the system matrix L also warrants attention. Figure 29 illustrates the sparsity pattern of L by showing the locations of its non-zero elements. Two inset plots provide magnified views. The bottom-left inset highlights the block-diagonal structure resulting from the local element terms (related to the mass and stiffness matrices), along with sparser, scattered entries away from the diagonal that arise from the numerical flux calculations coupling adjacent elements. The upper-right inset clearly demonstrates that the matrix L is non-symmetric.

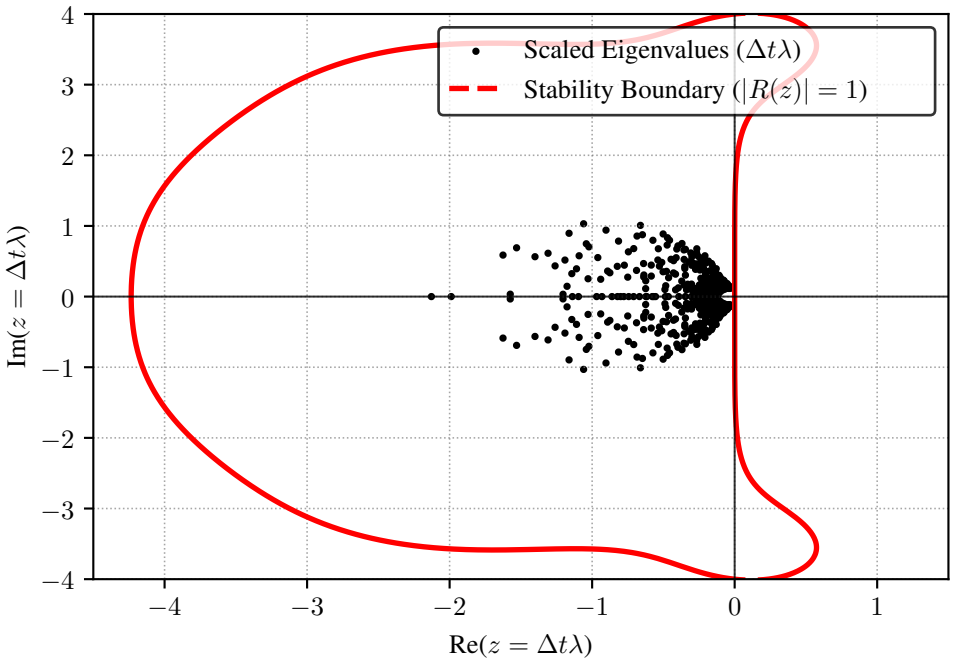

Figure 28 – Distribution in the complex plane of the 500 eigenvalues of the system matrix L possessing the largest magnitudes.

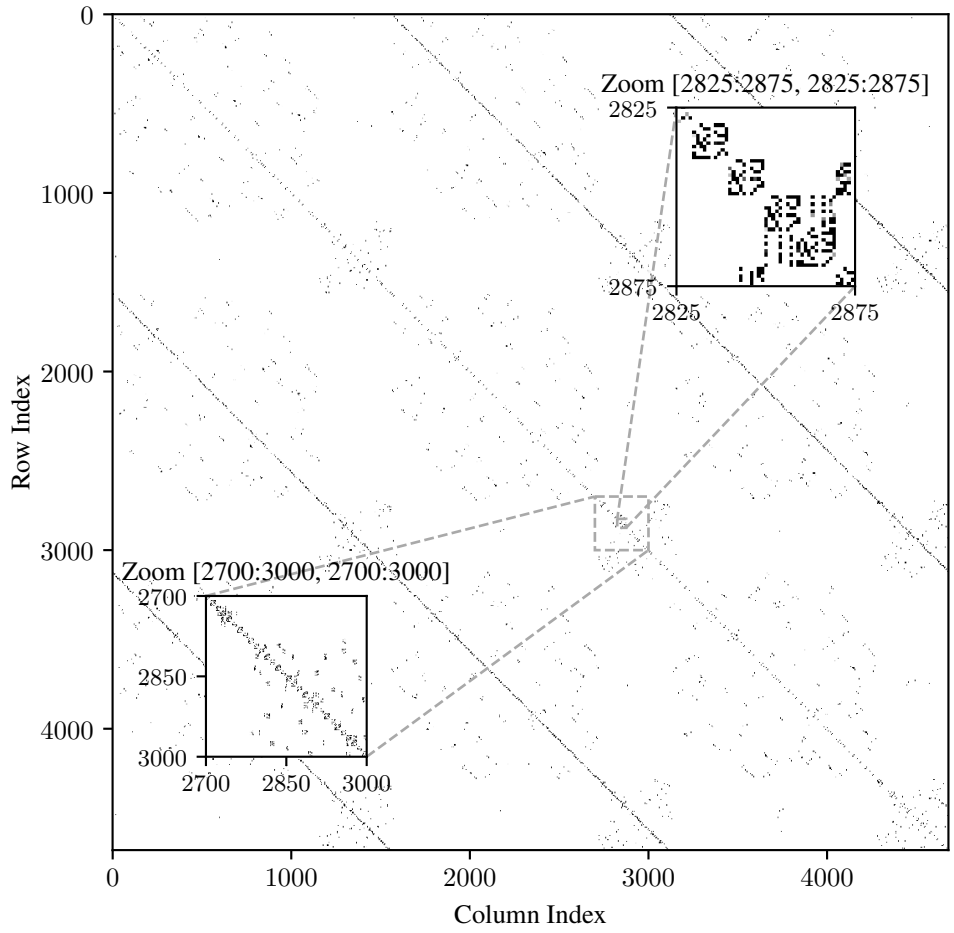

Figure 29 – Sparsity pattern of the system matrix L.

Figures 30 to 32 present comparative simulation results obtained using third-order elements for different time integration strategies applied to the two-region mesh problem. Each figure displays a spatial snapshot of the numerical electric field ($\boldsymbol{\mathcal{E}}_z^n$) alongside the relative error $(\boldsymbol{\mathcal{E}}_z^n - \boldsymbol{\mathcal{E}}_z^a)/E_0$, computed against the analytical solution $\boldsymbol{\mathcal{E}}_z^a$ (initial amplitude $E_0 = 1\,\text{V/m}$). The specific setups are as follows:

- Figure 30 shows the IMEX simulation, where the outer coarse mesh region was treated explicitly and the inner refined region implicitly. The time step Δt for this run was determined by the stability limit of the explicit (outer) region.
- Figure 31 depicts the fully explicit simulation. Since the explicit scheme was applied everywhere, its time step Δt was constrained by the stability limit of the more restrictive refined inner region, resulting in a significantly smaller Δt compared to the IMEX case.
- Figure 32 presents the fully implicit simulation. This simulation was intentionally run using the same larger time step Δt as employed in the IMEX simulation (i.e., the one based on the outer coarse region's explicit limit) to allow for a direct comparison of accuracy and computational cost under identical Δt conditions where possible.

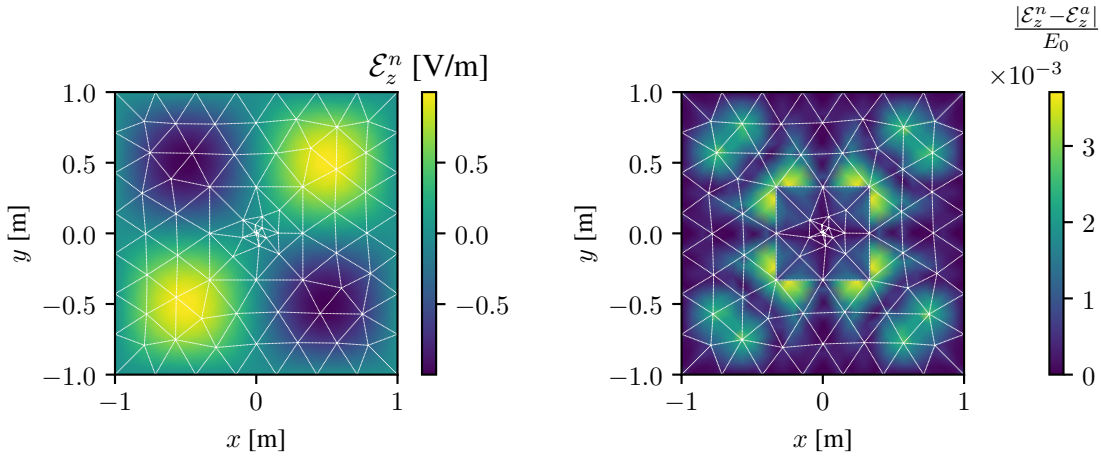

Figure 30 – Simulation results for the 2D cavity using the IMEX scheme with third-order elements at time $t = 3T_{11}/2$. Left: numerical electric field $\boldsymbol{\mathcal{E}}_z^n(\boldsymbol{x}, t)$. Right: relative error $(\boldsymbol{\mathcal{E}}_z^n - \boldsymbol{\mathcal{E}}_z^a)/E_0$ compared to the analytical solution, with $E_0 = 1\,\text{V/m}$.

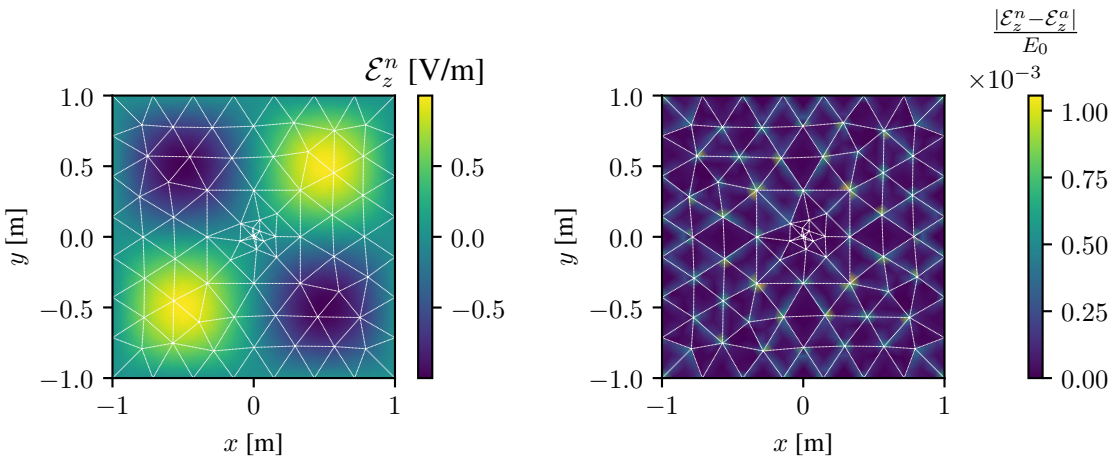

Figure 31 – Simulation results for the 2D cavity using the explicit scheme with third-order elements at time $t = 3T_{11}/2$. Left: numerical electric field $\boldsymbol{\mathcal{E}}_z^n(\boldsymbol{x}, t)$. Right: relative error $(\boldsymbol{\mathcal{E}}_z^n - \boldsymbol{\mathcal{E}}_z^a)/E_0$ compared to the analytical solution, with $E_0 = 1$ V/m.

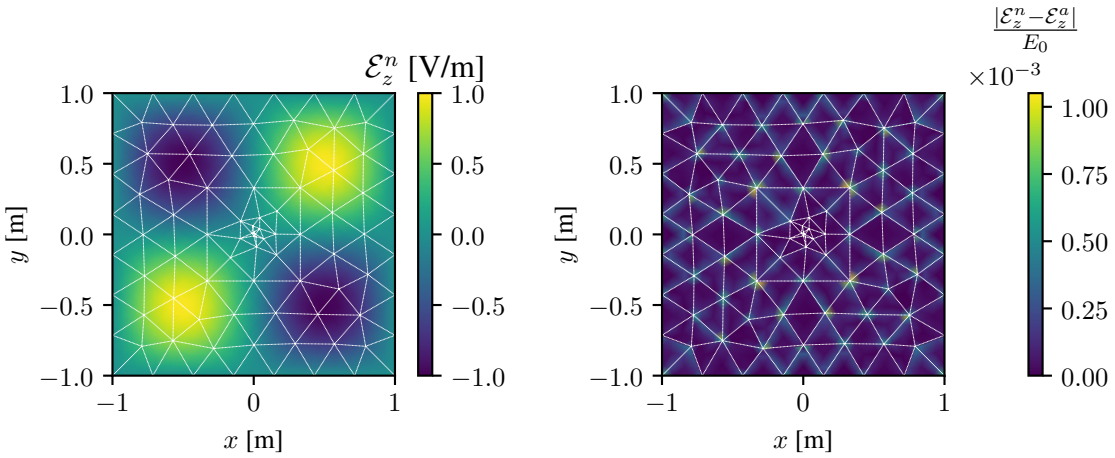

Figure 32 – Simulation results for the 2D cavity using the implicit scheme with third-order elements at time $t = 3T_{11}/2$. Left: numerical electric field $\boldsymbol{\mathcal{E}}_z^n(\boldsymbol{x}, t)$. Right: relative error $(\boldsymbol{\mathcal{E}}_z^n - \boldsymbol{\mathcal{E}}_z^a)/E_0$ compared to the analytical solution, with $E_0 = 1$ V/m.

A quantitative comparison of the performance for the IMEX, fully explicit, and fully implicit schemes, corresponding to the visual results in Figures 30 to 32, is presented in Table 9. This table lists the total simulation wall-clock time, the time step size Δt employed (normalized by the explicit method's stable time step, Δt_{exp}), and the final average relative error obtained with each approach using third-order elements.

Analyzing the results in Table 9 reveals distinct performance characteristics for each integration method when using third-order elements. The fully explicit scheme incurs the highest computational cost, requiring 58.73 s to complete the simulation. This is a direct consequence of its restrictive time step ($\Delta t = \Delta t_{exp}$), dictated by the stability limit imposed by the finest

Table 9 – Comparison of simulation time, relative time step, and average relative error for different integration schemes using third-order elements. The time step (Δt) for IMEX and Implicit methods is shown relative to the explicit method's time step (Δt_{exp})

Method	$\Delta t/\Delta t_{exp}$	Time (s)	Avg. Relative Error
IMEX	21.57	11.67	4.15×10^{-4}
Explicit	1.00	58.73	1.61×10^{-4}
Implicit	21.57	33.11	1.62×10^{-4}

elements in the mesh, thus necessitating a large number of time steps. Despite its computational expense, it achieves a relatively low average relative error of 1.61×10^{-4}.

Conversely, both the IMEX and fully implicit schemes could employ a significantly larger time step, approximately 21.6 times that of the explicit method ($\Delta t \approx 21.6 \times \Delta t_{exp}$). This larger Δt drastically reduces the required number of time steps. For the IMEX method, this time step is determined by the stability of the explicit part operating on the coarser outer mesh, while for the fully implicit method, it was chosen to match the IMEX scheme for comparison. Between these two, the IMEX method proves to be the fastest, completing the simulation in 11.67 s. Its efficiency stems from avoiding the need to solve a large global implicit system at each step; instead, it combines a smaller implicit solve for the refined inner region with computationally cheaper explicit updates for the outer region. The fully implicit method, requiring 33.11 s, is significantly faster than the explicit scheme due to the large time step but slower than IMEX because each step involves solving a computationally more expensive global linear system.

Regarding accuracy, the fully implicit scheme achieves the lowest average relative error (1.62×10^{-4}), performing nearly identically to the fully explicit method (1.61×10^{-4}) despite using a much larger time step. The IMEX scheme, while being the fastest, exhibits a higher average relative error of 4.15×10^{-4}. Although this error is still reasonably low, it is roughly 2.5 times higher than that of the implicit and explicit methods. This suggests that even though the inner region is treated implicitly, the explicit treatment of the coarse outer region with the large time step introduces additional discretization error that slightly degrades the overall accuracy compared to the fully implicit approach using the same time step.

These results highlight the inherent trade-offs between computational efficiency and accuracy. The IMEX method offers substantial speed benefits but at the cost of slightly reduced accuracy compared to the other methods. The fully implicit method provides accuracy comparable to the fully explicit method while being significantly faster due to the larger allowable time step, albeit slower than IMEX due to the per-step computational cost. The explicit method, while accurate, remains the slowest due to stability constraints. The choice of scheme therefore depends on the specific requirements of the simulation regarding acceptable error tolerance versus available computational resources.

7.4 Conclusion

This chapter provided a detailed exposition of an Implicit-Explicit (IMEX) time integration scheme specifically tailored for the DGTD method applied to complex electromagnetic problems. Emphasis was placed on the formulation required to handle frequency-dependent phenomena, outlining the necessary modifications to the standard DGTD system for incorporating dispersive material models (such as Debye or Lorentz) through the CCPR and dispersive uniaxial (PMLs) for accurate domain truncation. The core principle involved splitting the semi-discrete DGTD system into stiff terms, typically associated with implicit geometric features or fine mesh regions and auxiliary differential equations describing dispersion, and non-stiff terms suitable for explicit treatment.

While the framework presented is designed to accommodate these challenging dispersive effects, the numerical validation and comparative analysis within this chapter focused on a canonical benchmark problem: the evolution of the TM_{11} mode within a two-dimensional, vacuum-filled cavity bounded by PECs. This simpler case, possessing a known analytical solution, allowed for a clear assessment of the fundamental accuracy, stability, and computational efficiency characteristics of the IMEX approach relative to standard fully explicit and fully implicit schemes, particularly demonstrating the potential speed-ups enabled by IMEX in multi-scale scenarios, alongside its characteristic error behavior dominated by the explicit part.

Building upon the foundation and validation established here, future work will extend the application and analysis of this IMEX-DGTD framework to simulations involving doubly dispersive media, where both permittivity (ϵ) and permeability (μ) exhibit frequency dependence. This will enable a more comprehensive investigation into the performance, stability, and accuracy intrinsics of the developed scheme when confronted with the full complexity of such physically relevant electromagnetic interactions.

CHAPTER 8

Conclusion and Future Work

8.1 Summary of the Thesis

This thesis has addressed the challenging problem of accurately and efficiently simulating electromagnetic wave interactions with complex materials exhibiting frequency dispersion in open-domain scenarios utilizing the DGTD method. The primary motivation stems from the increasing need in fields such as nanophotonics, antenna design, metamaterial analysis, and scattering analysis to model realistic materials whose constitutive parameters (ϵ and potentially μ) vary significantly with frequency, often requiring simulation in unbounded regions. Traditional methods face limitations either in handling geometric complexity, modeling intricate material dispersion (particularly when both permittivity and permeability are frequency-dependent), or effectively truncating the computational domain, especially when dispersive media extend to the boundaries.

The core contribution of this work, detailed extensively throughout the thesis and particularly highlighted in Chapters 5 and 6 regarding the foundational aspects, is the development and validation of a novel DGTD formulation specifically designed to overcome these challenges. This formulation integrates several key advancements:

1. **General Dispersive Media Modeling:** It incorporates robust models for general dielectric dispersion based on the CCPR representation, often obtained via techniques like Vector Fitting. This allows for the accurate simulation of a wide range of realistic materials over broad frequency bands using a sum of auxiliary polarization terms ($\mathcal{P}_r$, and analogous magnetic terms). Furthermore, this framework was **extended to handle doubly dispersive media**, where both permittivity $\epsilon(\omega)$ and permeability $\mu(\omega)$ exhibit frequency dependence, incorporating corresponding auxiliary fields for the magnetic response.

2. **Dispersive Perfectly Matched Layer (PML):** A novel extension of the uniaxial PML was derived and implemented. Crucially, this PML is designed to directly match and absorb outgoing waves from general **(potentially doubly) dispersive media**, eliminating the common requirement for an intermediate buffer layer of free space or simple dielectric between the scatterer and the absorbing boundary. This was achieved by carefully deriving the necessary ADEs for the PML fields ($\boldsymbol{\mathcal{K}}$, $\boldsymbol{\mathcal{G}}$) and the coupling terms ($\boldsymbol{\mathcal{R}}_r$, and analogous magnetic terms) that arise from the interaction between the PML and the dispersive material models.

3. **Modular Implementation Framework:** A highly modular implementation strategy was proposed and utilized. By treating the standard Maxwell equations for simple media as a baseline, the effects of dielectric dispersion (via $\boldsymbol{\mathcal{P}}_r$), magnetic dispersion (via $\boldsymbol{\mathcal{Q}}_r$), and PML absorption (via $\boldsymbol{\mathcal{K}}$, $\boldsymbol{\mathcal{G}}$, $\boldsymbol{\mathcal{R}}_r$, etc.) are introduced as additive correction terms computed only in the relevant regions of the computational domain. This "plug-and-play" approach enhances code clarity, simplifies the handling of complex geometries with multiple material types, and promotes computational efficiency.

4. **Implicit-Explicit (IMEX) Time Integration:** Recognizing that the combination of multiple dispersion terms, particularly in the doubly dispersive case, can lead to stiffness in the system of ODEs, **an IMEX Runge-Kutta time integration scheme was proposed and investigated**. This scheme strategically treats potentially stiff terms (often related to the ADEs) implicitly while handling the main wave propagation terms explicitly, aiming for improved stability and potentially allowing larger time steps compared to purely explicit methods under certain conditions.

5. **Incident Field Incorporation:** The TF/SF technique was integrated naturally within the DGTD framework to introduce incident plane waves, enabling the straightforward simulation of scattering problems.

8.2 Key Findings and Validation

The effectiveness, accuracy, and stability of the proposed DGTD formulation, including the extensions for doubly dispersive media and the IMEX scheme, were rigorously validated through numerical experiments presented in the thesis.

- Canonical problems, such as the two-dimensional example in Chapter 5 involving a plane wave incident on a dispersive slab truncated by dispersive PMLs, demonstrated the formulation's ability to handle all constituent parts (free space, dielectric dispersion, PML, dispersive PML) correctly within a unified simulation. Analysis of the L_2 error against analytical solutions confirmed the expected high-order accuracy and convergence rates.

- **Validation was extended to doubly dispersive scenarios**, confirming that the formulation accurately captures the combined frequency-dependent effects of both permittivity and permeability.
- The complex three-dimensional simulation of plane wave scattering by a dispersive dielectric sphere (Silver) further showcased the method's capabilities in handling realistic geometries and material models obtained from fitting experimental data. Comparison with analytical solutions showed excellent agreement.
- Crucially, the examples validated the ability of the dispersive PML to effectively truncate the computational domain where singly or doubly dispersive materials are present, without spurious reflections or the need for artificial buffer zones.

These results collectively demonstrate that the developed DGTD method provides an accurate, flexible, stable, and robust tool for simulating electromagnetic wave phenomena in the presence of general, potentially doubly, dispersive materials within open regions.

8.3 Significance and Implications

This research contributes significantly to the field of computational electromagnetics by providing an enhanced DGTD toolset. The key implications include:

- **Broader Modeling Capabilities:** Enables more accurate simulations of devices and phenomena involving a wider class of materials, including those with both electric and magnetic dispersion (e.g., certain metamaterials, ferrites, composites).
- **Improved Stability for Complex Models:** The proposed IMEX scheme offers a pathway to robustly handle the potential numerical stiffness associated with complex, multi-pole, or doubly dispersive material models, potentially improving simulation reliability and efficiency.
- **Simplified Simulation Setup:** The ability to directly truncate dispersive domains simplifies meshing and setup, reducing user effort and potential errors.
- **Enhanced Efficiency:** The modular approach optimizes computations, and direct truncation can lead to smaller domains. The IMEX scheme might allow larger time steps in some stiff scenarios, further boosting efficiency.
- **Wide Applicability:** The method is well-suited for analyzing optical components, antennas with complex substrates/radomes, radar cross-sections of targets with advanced coatings, studies involving dispersive shielding or components, and the design of novel metamaterial structures.

8.4 Limitations and Future Work

While this thesis successfully demonstrates the proposed formulation, several avenues for future research and development remain:

- **Extension to Anisotropic Doubly Dispersive Media:** Extending the formulation, the dispersive PML, and potentially the IMEX strategies to handle materials that are simultaneously anisotropic and doubly dispersive remains a significant challenge but would unlock simulations of highly complex media.
- **Nonlinear Dispersion:** Incorporating nonlinear dispersive effects (e.g., Kerr effect, Raman scattering) within the doubly dispersive DGTD framework would be a valuable extension for studying high-intensity field interactions.
- **Optimization and Analysis of IMEX Schemes:** Further theoretical analysis and numerical investigation are needed to determine the optimal partitioning and implementation of IMEX schemes for various classes of dispersive problems and DGTD discretizations, aiming to maximize stability gains and efficiency. Comparing different IMEX families would also be beneficial.
- **Performance Optimization:** Continued work on computational performance, including advanced parallelization strategies (MPI/OpenMP, GPU acceleration) tailored to the modular ADE structure and the specific demands of implicit solves within IMEX, is crucial for large-scale applications.
- **Adaptive Techniques:** Implementing adaptive mesh refinement (h-adaptivity) and/or polynomial order adaptation (p-adaptivity), guided by error estimators sensitive to wave resolution, dispersion modeling accuracy, and PML performance, could optimize resource usage.
- **Hybrid Methods:** Exploring hybrid approaches combining the doubly dispersive DGTD method with other techniques could be advantageous for specific multi-scale or geometrically complex problems.
- **Application to Cutting-Edge Problems:** Applying the developed solver, including the doubly dispersive capabilities and IMEX scheme, to challenging real-world design problems (e.g., optimizing multi-functional metamaterials, analyzing ferrite devices) would provide further validation and demonstrate its practical utility.

8.5 Concluding Remarks

This thesis has presented significant advancements in the capabilities of the DGTD method for simulating electromagnetic interactions with complex, frequency-dependent materials. By developing a formulation that seamlessly integrates general dielectric, magnetic, and **doubly dispersive** media with a directly matching dispersive PML through a modular, ADE-based approach, and by **proposing a suitable IMEX time integration strategy** to handle potential stiffness, this work provides a powerful, accurate, flexible, and stable computational tool. The successful validation against analytical solutions underscores its reliability. The research opens up new possibilities for modeling and understanding intricate wave phenomena in a broader range of realistic materials and paves the way for future extensions and applications in diverse areas of science and engineering.

Bibliography

[1] Y.-O. Cha, A. A. Ihalage, and Y. Hao, "Antennas and propagation research from large-scale unstructured data with machine learning: A review and predictions," *IEEE Antennas and Propagation Magazine*, vol. 65, pp. 10–24, Oct. 2023. DOI: 10.1109/MAP.2023.3290385.

[2] C. A. Balanis, *Balanis' Advanced Engineering Electromagnetics*. Hoboken, New Jersey: John Wiley & Sons, third edition ed., 2024. DOI: 10.1002/9781394180042.

[3] M. J. Fakhimi and O. B. Akan, "Nanoantennas and nanoradars: The future of integrated sensing and communication at the nanoscale," *IEEE Transactions on Molecular, Biological, and Multi-Scale Communications*, vol. 10, pp. 493–516, Dec. 2024. DOI: 10.1109/TMBMC.2024.3434545.

[4] Y. Luo, H.-K. Huang, K. Sastry, P. Hu, X. Tong, J. Kuo, Y. Aborahama, S. Na, U. Villa, Mark. A. Anastasio, and L. V. Wang, "Full-wave image reconstruction in transcranial photoacoustic computed tomography using a finite element method," *IEEE Transactions on Medical Imaging*, vol. 44, pp. 645–655, Feb. 2025. DOI: 10.1109/TMI.2024.3456595.

[5] A. Taflove and S. C. Hagness, *Computational electrodynamics: the finite-difference time-domain method*. Artech House antennas and propagation library, Boston: Artech House, 3rd ed., 2005. ISBN: 978-158-053-8-3-2-9.

[6] J. S. Hesthaven and T. Warburton, *Nodal Discontinuous Galerkin Methods*, vol. 54 of *Texts in Applied Mathematics*. New York, NY: Springer New York, 2008. DOI: 10.1007/978-0-387-72067-8.

[7] R. Eymard, T. Gallouët, and R. Herbin, "Finite volume methods," in *Handbook of Numerical Analysis*, vol. 7, pp. 713–1018, Elsevier, 2000. DOI: 10.1016/S1570-8659(00)07005-8.

[8] J.-M. Jin, *The Finite Element Method in Electromagnetics*. Piscataway, NJ: IEEE Press, 3rd ed., 2014. ISBN: 978-111-857-1-3-6-1.

[9] C. Gabriel, S. Gabriel, and E. Corthout, "The dielectric properties of biological tissues: I. Literature survey," *Physics in Medicine and Biology*, vol. 41, pp. 2231–2249, Nov. 1996. DOI: 10.1088/0031-9155/41/11/001.

[10] S. A. Maier, *Plasmonics: Fundamentals and Applications*. New York, NY: Springer US, 2007. DOI: 10.1007/0-387-37825-1.

[11] J. D. Joannopoulos, ed., *Photonic Crystals: Molding the Flow of Light*. Princeton: Princeton University Press, 2nd ed ed., 2008. ISBN: 978-0-691-12456-8.

[12] T. J. Cui, D. Smith, and R. Liu, eds., *Metamaterials: Theory, Design, and Applications*. Boston, MA: Springer US, 2010. DOI: 10.1007/978-1-4419-0573-4.

[13] R. Luebbers, F. P. Hunsberger, K. S. Kunz, R. B. Standler, and M. Schneider, "A frequency-dependent finite-difference time-domain formulation for dispersive materials," *IEEE Transactions on Electromagnetic Compatibility*, vol. 32, pp. 222–227, Aug. 1990. DOI: 10.1109/15.57116.

[14] D. M. Sullivan, "Frequency-dependent FDTD methods using Z transforms," *IEEE Transactions on Antennas and Propagation*, vol. 40, pp. 1223–1230, Oct. 1992. DOI: 10.1109/8.182455.

[15] Q. Chen, M. Katsurai, and P. H. Aoyagi, "An FDTD formulation for dispersive media using a current density," *IEEE Transactions on Antennas and Propagation*, vol. 46, pp. 1739–1746, Nov. 1998. DOI: 10.1109/8.736632.

[16] J.-P. Berenger, "A perfectly matched layer for the absorption of electromagnetic waves," *Journal of Computational Physics*, vol. 114, no. 2, pp. 185–200, 1994. DOI: 10.1006/JCPH.1994.1159.

[17] L. D. Angulo, J. Alvarez, M. F. Pantoja, S. G. Garcia, and A. R. Bretones, "Discontinuous Galerkin time domain methods in computational electrodynamics: State of the art," *Forum for Electromagnetic Research Methods and Application Technologies*, vol. 10, pp. 1–24, Aug. 2015. Available from Internet. Accessed: 01 jan. 2025.

[18] S. Dosopoulos, J. D. Gardiner, and J.-F. Lee, "An MPI/GPU parallelization of an interior penalty discontinuous Galerkin time domain method for Maxwell's equations," *Radio Science*, vol. 46, p. 2011RS004689, June 2011. DOI: 10.1029/2011RS004689.

[19] Y. Shi, P. Wang, S. C. Zhu, S. P. Li, and Z. G. Ban, "An hp-adaptive scheme of discontinuous Galerkin time-domain method with fast error estimation," *IEEE Transactions on Microwave Theory and Techniques*, vol. 70, pp. 3776–3788, Aug. 2022. DOI: 10.1109/TMTT.2022.3179006.

[20] Z. G. Ban, Y. Shi, and P. Wang, "Advanced parallelism of DGTD method with local time stepping based on novel MPI + MPI unified parallel algorithm," *IEEE Transactions on Antennas and Propagation*, vol. 70, pp. 3916–3921, May 2022. DOI: 10.1109/TAP.2021.3137455.

[21] A. Kanevsky, M. H. Carpenter, D. Gottlieb, and J. S. Hesthaven, "Application of implicit–explicit high order Runge–Kutta methods to discontinuous-Galerkin schemes," *Journal of Computational Physics*, vol. 225, pp. 1753–1781, Aug. 2007. DOI: 10.1016/j.jcp.2007.02.021.

[22] T. Lu, P. Zhang, and W. Cai, "Discontinuous Galerkin methods for dispersive and lossy Maxwell's equations and PML boundary conditions," *Journal of Computational Physics*, vol. 200, pp. 549–580, Nov. 2004. DOI: 10.1016/J.JCP.2004.02.022.

[23] K. Niknam and J. Simpson, "A review of grid-based, time-domain modeling of electromagnetic wave propagation involving the ionosphere," *IEEE Journal on Multiscale and Multiphysics Computational Techniques*, vol. 6, pp. 214–228, 2021. DOI: 10.1109/JMMCT.2021.3136128.

[24] X. Qin, X. Wu, S. Wang, X. Zhao, Y. Zhou, and Q. Ren, "Perfectly matched layer for Cole–Cole dispersive media in DGTD method," *IEEE Journal on Multiscale and Multiphysics Computational Techniques*, vol. 9, pp. 320–329, 2024. DOI: 10.1109/JMMCT.2024.3462529.

[25] Q. Ren, H. Cao, and Q. H. Liu, "Novel efficient discontinuous Galerkin time- domain modeling of dispersive Chiral metamaterials via media homogenization," *IEEE Transactions on Microwave Theory and Techniques*, vol. 72, pp. 5218–5227, Sept. 2024. DOI: 10.1109/TMTT.2024.3367786.

[26] M. Han, R. W. Dutton, and S. Fan, "Model dispersive media in finite-difference time-domain method with complex-conjugate pole-residue pairs," *IEEE Microwave and Wireless Components Letters*, vol. 16, no. 3, pp. 119–121, 2006. DOI: 10.1109/LMWC.2006.869862.

[27] B. Gustavsen and A. Semlyen, "Rational approximation of frequency domain responses by vector fitting," *IEEE Transactions on Power Delivery*, vol. 14, pp. 1052–1061, July 1999. DOI: 10.1109/61.772353.

[28] F. L. Teixeira, Weng Cho Chew, M. Straka, M. L. Oristaglio, and T. Wang, "Finite-difference time-domain simulation of ground penetrating radar on dispersive, inhomogeneous, and conductive soils," *IEEE Transactions on Geoscience and Remote Sensing*, vol. 36, pp. 1928–1937, Nov. 1998. DOI: 10.1109/36.729364.

[29] T. V. L. Amorim, E. J. Silva, F. J. S. Moreira, and F. L. Teixeira, "Modular discontinuous galerkin time-domain method for general dispersive media with vector fitting," *IEEE*

Journal on Multiscale and Multiphysics Computational Techniques, vol. 10, pp. 179–186, 2025. DOI: 10.1109/JMMCT.2025.3542379.

[30] T. V. L. Amorim, E. J. Silva, F. J. S. Moreira, and F. L. Teixeira, "Modular DGTD implementation for doubly dispersive media with curvilinear elements," *IEEE Antennas and Wireless Propagation Letters*, vol. 24, no. 10, pp. 3644–3648, 2025. DOI: 10.1109/LAWP.2025.3599788.

[31] T. V. L. Amorim, E. J. Silva, and F. J. S. Moreira, "Discontinuous Galerkin time-domain method in computational electrodynamic scattering problems," in *Proceedings of the 20th Brazilian Symposium on Microwaves and Optoelectronics (SBMO 2022)*, (Natal, RN, Brazil), pp. 321–325, Nov. 2022. Available from Internet. Accessed: 01 jan. 2025.

[32] T. V. L. Amorim, E. J. Silva, F. J. S. Moreira, and F. L. Teixeira, "A plug-and-play DGTD implementation for general dispersive media," in *2024 IEEE International Symposium on Antennas and Propagation and INC/USNC-URSI Radio Science Meeting (AP-S/INC-USNC-URSI)*, pp. 2303–2304, 2024. DOI: 10.1109/AP-S/INC-USNC-URSI52054.2024.10686306.

[33] R. F. Harrington, *Time-Harmonic Electromagnetic Fields*. Wiley-IEEE Press, Sept. 2001. DOI: 10.1109/9780470546710.

[34] J. B. Schneider, *Understanding the Finite-Difference Time-Domain Method*. School of electrical engineering and computer science, Washington State University, 2025. Available from Internet. Accessed: 01 jan. 2025.

[35] T. Lu, W. Cai, and P. Zhang, "Discontinuous galerkin time-domain method for GPR simulation in dispersive media," *IEEE Transactions on Geoscience and Remote Sensing*, vol. 43, no. 1, pp. 72–80, 2005. DOI: 10.1109/TGRS.2004.838350.

[36] U. S. Inan and R. A. Marshall, *Numerical Electromagnetics: The FDTD Method*. Cambridge University Press, 1st ed., Apr. 2011. DOI: 10.1017/CBO9780511921353.

[37] M. H. Carpenter and C. A. Kennedy, "Fourth-order 2n-storage runge-kutta schemes," tech. rep., NASA Langley Research Center, 1994. Available from Internet. Accessed: 01 jan. 2025.

[38] E. Hairer and G. Wanner, *Solving Ordinary Differential Equations II*, vol. 14 of *Springer Series in Computational Mathematics*. Berlin, Heidelberg: Springer Berlin Heidelberg, 1996. DOI: 10.1007/978-3-642-05221-7.

[39] J. S. Hesthaven and T. Warburton, "Nodal high-order methods on unstructured grids: I. Time-domain solution of Maxwell's equations," *Journal of Computational Physics*, vol. 181, pp. 186–221, Sept. 2002. DOI: 10.1006/JCPH.2002.7118.

[40] K. Busch, M. König, and J. Niegemann, "Discontinuous Galerkin methods in nanophotonics," *Laser & Photonics Reviews*, vol. 5, pp. 773–809, Nov. 2011. DOI: 10.1002/LPOR.201000045.

[41] J. Alvarez, L. D. Angulo, M. F. Pantoja, A. R. Bretones, and S. G. Garcia, "Source and boundary implementation in vector and scalar DGTD," *IEEE Transactions on Antennas and Propagation*, vol. 58, pp. 1997–2003, June 2010. DOI: "10.1109/TAP.2010.2046857.

[42] P. Li and L. J. Jiang, "Uncertainty quantification for electromagnetic systems using ASGC and DGTD method," *IEEE Transactions on Electromagnetic Compatibility*, vol. 57, pp. 754–763, Aug. 2015. DOI: 10.1109/TEMC.2015.2403304.

[43] Ping Li, Yifei Shi, Li Jun Jiang, and H. Bagci, "DGTD analysis of electromagnetic scattering from penetrable conductive objects with IBC," *IEEE Transactions on Antennas and Propagation*, vol. 63, pp. 5686–5697, Dec. 2015. DOI: 10.1109/TAP.2015.2491969.

[44] S. Yan and J.-M. Jin, "A dynamic p-adaptive DGTD algorithm for electromagnetic and multiphysics simulations," *IEEE Transactions on Antennas and Propagation*, vol. 65, pp. 2446–2459, May 2017. DOI: 10.1109/TAP.2017.2676724.

[45] H. Bao, L. Kang, S. D. Campbell, and D. H. Werner, "PML implementation in a nonconforming mixed-element DGTD method for periodic structure analysis," *IEEE Transactions on Antennas and Propagation*, vol. 67, pp. 6979–6988, Nov. 2019. DOI: 10.1109/TAP.2019.2927663.

[46] H. H. Zhang, X. Y. Liu, Y. Liu, Z. C. Fan, and H. L. Du, "Thermal-mechanical-electromagnetic multiphysics simulation of satellite phased array antenna based on DGTD and FEM method," *IEEE Journal on Multiscale and Multiphysics Computational Techniques*, vol. 9, pp. 236–246, 2024. DOI: 10.1109/JMMCT.2024.3428517.

[47] W. Mai, S. D. Campbell, E. B. Whiting, L. Kang, P. L. Werner, Y. Chen, and D. H. Werner, "Prismatic discontinuous Galerkin time domain method with an integrated generalized dispersion model for efficient optical metasurface analysis," *Optical Materials Express*, vol. 10, p. 2542, Oct. 2020. DOI: 10.1364/OME.399414.

[48] Q. Ren, H. Bao, S. D. Campbell, L. J. Prokopeva, A. V. Kildishev, and D. H. Werner, "Continuous-discontinuous Galerkin time domain (CDGTD) method with generalized dispersive material (GDM) model for computational photonics," *Optics Express*, vol. 26, pp. 29005–29016, Oct. 2018. DOI: 10.1364/OE.26.029005.

[49] E. D. Palik, *Handbook of Optical Constants of Solids*, vol. 3. Academic Press, 1998. ISBN: 978-012-544-4-2-3-1.

[50] J.-M. Jin, *Theory and Computation of Electromagnetic Fields*. Wiley-IEEE Press, 2nd ed., Aug. 2015. ISBN: 978-111-910-8-0-4-7.

[51] B. Donderici and F. L. Teixeira, "Mixed finite-element time-domain method for transient Maxwell equations in doubly dispersive media," *IEEE Transactions on Microwave Theory and Techniques*, vol. 56, no. 1, pp. 113–120, 2008. DOI: 10.1109/TMTT.2007.912217.

[52] F. Chen, "A HIE-FDTD method for double-dispersive media," *IEEE Antennas and Wireless Propagation Letters*, vol. 23, no. 10, pp. 3023–3027, 2024. DOI: 10.1109/LAWP.2024.3418867.

[53] J. Lu, "An improved absorbing boundary condition for finite-element analysis," *IEEE Transactions on Antennas and Propagation*, vol. 72, no. 10, pp. 8109–8114, 2024. DOI: 10.1109/TAP.2024.3445121.

[54] Y.-H. Chen, B.-Y. Wu, C.-Z. Yan, Z.-H. Zhao, and X.-Q. Sheng, "A discontinuous galerkin integral equation method for multiscale surface-wire structures," *IEEE Transactions on Antennas and Propagation*, vol. 72, no. 10, pp. 7883–7892, 2024. DOI: 10.1109/TAP.2024.3445534.

[55] Y. Dong, M. Tang, P. Li, and J. Mao, "Transient electromagnetic-thermal simulation of dispersive media using DGTD method," *IEEE Transactions on Electromagnetic Compatibility*, vol. 61, no. 4, pp. 1305–1313, 2019. DOI: 10.1109/TEMC.2019.2911039.

[56] Q. Yang, B. Wei, L. Li, R. Li, and D. Ge, "An SO-DGTD method of modeling dispersive media," *Waves in Random and Complex Media*, vol. 31, no. 2, pp. 389–402, 2021. DOI: 10.1080/17455030.2019.1593550.

[57] X. Ji, W. Cai, and P. Zhang, "High-order DGTD methods for dispersive Maxwell's equations and modelling of silver nanowire coupling," *International Journal for Numerical Methods in Engineering*, vol. 69, no. 2, pp. 308–325, 2007. DOI: 10.1002/NME.1762.

[58] M. R. Zunoubi, J. Payne, and W. P. Roach, "CUDA implementation of TE^z-FDTD solution of maxwell's equations in dispersive media," *IEEE Antennas and Wireless Propagation Letters*, vol. 9, pp. 756–759, 2010. DOI: 10.1109/LAWP.2010.2060181.

[59] A. Akbarzadeh-Sharbaf and D. D. Giannacopoulos, "Finite-element time-domain solution of the vector wave equation in doubly dispersive media using Mö bius transformation technique," *IEEE Transactions on Antennas and Propagation*, vol. 61, no. 8, pp. 4158–4166, 2013. DOI: 10.1109/TAP.2013.2260716.

[60] J. Shibayama, K. Suzuki, T. Iwamoto, J. Yamauchi, and H. Nakano, "Dispersive contour-path FDTD algorithm for the Drude–Lorentz model," *IEEE Antennas and Wireless Propagation Letters*, vol. 19, pp. 1699–1703, Oct. 2020. DOI: 10.1109/LAWP.2020.3014344.

[61] S. D. Gedney, J. C. Young, T. C. Kramer, and J. A. Roden, "A discontinuous galerkin finite element time-domain method modeling of dispersive media," *IEEE Transactions on Antennas and Propagation*, vol. 60, pp. 1969–1977, Apr. 2012. DOI: 10.1109/TAP.2012.2186273.

[62] F. Chen, "A HIE-FDTD method for double-dispersive media," *IEEE Antennas and Wireless Propagation Letters*, vol. 23, pp. 3023–3027, Oct. 2024. DOI: 10.1109/LAWP.2024.3418867.

APPENDIX A

Mathematical Development

This appendix provides supplementary mathematical details relevant to the numerical methods employed. Specifically, it outlines the derivation for expressing Maxwell's equations in a conservation law form suitable for numerical schemes like the DGTD method, and details the formulation of the numerical flux used at element interfaces for a one-dimensional case.

A.1 Writing Maxwell's Equations in Conservation Form

The starting point is Maxwell's equations in a medium characterized by permittivity $\bar{\bar{\epsilon}}(\boldsymbol{x}, t)$ and permeability $\bar{\bar{\mu}}(\boldsymbol{x}, t)$, including electric current density source $\boldsymbol{\mathcal{J}}(\boldsymbol{x}, t)$ and magnetic current density source $\boldsymbol{\mathcal{M}}(\boldsymbol{x}, t)$:

$$\bar{\bar{\mu}}(\boldsymbol{x})\frac{\partial \boldsymbol{\mathcal{H}}(\boldsymbol{x}, t)}{\partial t} + \nabla \times \boldsymbol{\mathcal{E}}(\boldsymbol{x}, t) + \boldsymbol{\mathcal{M}}(\boldsymbol{x}, t) = 0, \tag{A.1}$$

$$\bar{\bar{\epsilon}}(\boldsymbol{x})\frac{\partial \boldsymbol{\mathcal{E}}(\boldsymbol{x}, t)}{\partial t} - \nabla \times \boldsymbol{\mathcal{H}}(\boldsymbol{x}, t) + \boldsymbol{\mathcal{J}}(\boldsymbol{x}, t) = 0. \tag{A.2}$$

For application within numerical methods based on conservation laws, it is advantageous to rewrite these two coupled first-order equations as a single system. This system can be expressed in a compact matrix-vector form as presented in Equation (A.3):

$$Q(\boldsymbol{x}) \cdot \frac{\partial \vec{q}(\boldsymbol{x}, t)}{\partial t} + \vec{\mathcal{K}}(\boldsymbol{x}, t) = \vec{\mathcal{S}}(\boldsymbol{x}, t), \tag{A.3}$$

where the constituent matrix Q and vectors $\vec{q}$, $\vec{\mathcal{K}}$, $\vec{\mathcal{S}}$ are defined as follows:

$$Q(\boldsymbol{x}) = \begin{bmatrix} \bar{\bar{\mu}}(\boldsymbol{x}) & \mathbf{0} \\ \mathbf{0} & \bar{\bar{\epsilon}}(\boldsymbol{x}) \end{bmatrix}, \qquad \vec{q}(\boldsymbol{x},t) = \begin{bmatrix} \boldsymbol{\mathcal{H}}(\boldsymbol{x},t) \\ \boldsymbol{\mathcal{E}}(\boldsymbol{x},t) \end{bmatrix},$$
$$\vec{\mathcal{K}}(\boldsymbol{x},t) = \begin{bmatrix} \nabla \times \boldsymbol{\mathcal{E}}(\boldsymbol{x},t) \\ -\nabla \times \boldsymbol{\mathcal{H}}(\boldsymbol{x},t) \end{bmatrix}, \qquad \vec{\mathcal{S}}(\boldsymbol{x},t) = \begin{bmatrix} -\boldsymbol{\mathcal{M}}(\boldsymbol{x},t) \\ -\boldsymbol{\mathcal{J}}(\boldsymbol{x},t) \end{bmatrix}.$$

Here, $\vec{q}(\boldsymbol{x},t)$ is the state vector containing the six field components, $Q(\boldsymbol{x},t)$ is the material property matrix (containing the permeability and permittivity tensors), $\vec{\mathcal{K}}(\boldsymbol{x},t)$ contains the spatial derivative terms (curls), and $\vec{\mathcal{S}}(\boldsymbol{x},t)$ is the source vector.

Expanding these terms into their Cartesian components reveals the detailed structure of the 6×6 matrix Q and the 6-component vectors $\vec{q}$, $\vec{\mathcal{K}}$, and $\vec{\mathcal{S}}$:

$$Q(\boldsymbol{x}) = \begin{bmatrix} \mu_{xx} & \mu_{xy} & \mu_{xz} & 0 & 0 & 0 \\ \mu_{yx} & \mu_{yy} & \mu_{yz} & 0 & 0 & 0 \\ \mu_{zx} & \mu_{zy} & \mu_{zz} & 0 & 0 & 0 \\ 0 & 0 & 0 & \epsilon_{xx} & \epsilon_{xy} & \epsilon_{xz} \\ 0 & 0 & 0 & \epsilon_{yx} & \epsilon_{yy} & \epsilon_{yz} \\ 0 & 0 & 0 & \epsilon_{zx} & \epsilon_{zy} & \epsilon_{zz} \end{bmatrix}, \qquad \vec{q}(\boldsymbol{x},t) = \begin{bmatrix} \mathcal{H}_x(\boldsymbol{x},t) \\ \mathcal{H}_y(\boldsymbol{x},t) \\ \mathcal{H}_z(\boldsymbol{x},t) \\ \mathcal{E}_x(\boldsymbol{x},t) \\ \mathcal{E}_y(\boldsymbol{x},t) \\ \mathcal{E}_z(\boldsymbol{x},t) \end{bmatrix},$$

$$\vec{\mathcal{K}}(\boldsymbol{x},t) = \frac{\partial}{\partial x}\begin{bmatrix} 0 \\ -\mathcal{E}_z \\ \mathcal{E}_y \\ 0 \\ \mathcal{H}_z \\ -\mathcal{H}_y \end{bmatrix} + \frac{\partial}{\partial y}\begin{bmatrix} \mathcal{E}_z \\ 0 \\ -\mathcal{E}_x \\ -\mathcal{H}_z \\ 0 \\ \mathcal{H}_x \end{bmatrix} + \frac{\partial}{\partial z}\begin{bmatrix} -\mathcal{E}_y \\ \mathcal{E}_x \\ 0 \\ \mathcal{H}_y \\ -\mathcal{H}_x \\ 0 \end{bmatrix},$$

$$\vec{\mathcal{S}}(\boldsymbol{x},t) = \begin{bmatrix} -\mathcal{M}_x(\boldsymbol{x},t) \\ -\mathcal{M}_y(\boldsymbol{x},t) \\ -\mathcal{M}_z(\boldsymbol{x},t) \\ -\mathcal{J}_x(\boldsymbol{x},t) \\ -\mathcal{J}_y(\boldsymbol{x},t) \\ -\mathcal{J}_z(\boldsymbol{x},t) \end{bmatrix}.$$

Focusing on the structure within the spatial derivative term $\vec{\mathcal{K}}(\boldsymbol{x},t)$, observe that each vector multiplied by a spatial derivative operator ($\partial/\partial x$, $\partial/\partial y$, $\partial/\partial z$) can be expressed using cross products involving the field vectors $\boldsymbol{\mathcal{E}}$, $\boldsymbol{\mathcal{H}}$ and the Cartesian unit vectors $\hat{\mathbf{x}}$, $\hat{\mathbf{y}}$, $\hat{\mathbf{z}}$. This allows rewriting $\vec{\mathcal{K}}(\boldsymbol{x},t)$ as:

$$\vec{\mathcal{K}}(\boldsymbol{x},t) = \frac{\partial}{\partial x}\begin{bmatrix} \hat{\mathbf{x}} \times \boldsymbol{\mathcal{E}}(\boldsymbol{x},t) \\ -\hat{\mathbf{x}} \times \boldsymbol{\mathcal{H}}(\boldsymbol{x},t) \end{bmatrix} + \frac{\partial}{\partial y}\begin{bmatrix} \hat{\mathbf{y}} \times \boldsymbol{\mathcal{E}}(\boldsymbol{x},t) \\ -\hat{\mathbf{y}} \times \boldsymbol{\mathcal{H}}(\boldsymbol{x},t) \end{bmatrix} + \frac{\partial}{\partial z}\begin{bmatrix} \hat{\mathbf{z}} \times \boldsymbol{\mathcal{E}}(\boldsymbol{x},t) \\ -\hat{\mathbf{z}} \times \boldsymbol{\mathcal{H}}(\boldsymbol{x},t) \end{bmatrix}. \tag{A.4}$$

To express this in the standard conservation law format $\partial_t \vec{u} + \nabla \cdot \mathbb{F} = \vec{S}$, define the flux vector function $\vec{\mathcal{F}}_i(\vec{q})$ associated with each Cartesian direction $i \in \{x, y, z\}$ as:

$$\vec{\mathcal{F}}_i(\vec{q}(\boldsymbol{x}, t)) = \begin{bmatrix} \mathbf{e}_i \times \boldsymbol{\mathcal{E}}(\boldsymbol{x}, t) \\ -\mathbf{e}_i \times \boldsymbol{\mathcal{H}}(\boldsymbol{x}, t) \end{bmatrix}, \tag{A.5}$$

where $\mathbf{e}_i$ denotes the i-th Cartesian unit vector (i.e., $\mathbf{e}_x = \hat{\mathbf{x}}$, etc.) [39]. Using this definition, the spatial term $\vec{\mathcal{K}}(\boldsymbol{x}, t)$ from Equation (A.4) becomes a sum of partial derivatives of these flux vectors:

$$\vec{\mathcal{K}}(\boldsymbol{x}, t) = \frac{\partial}{\partial x}\vec{\mathcal{F}}_x(\vec{q}(\boldsymbol{x}, t)) + \frac{\partial}{\partial y}\vec{\mathcal{F}}_y(\vec{q}(\boldsymbol{x}, t)) + \frac{\partial}{\partial z}\vec{\mathcal{F}}_z(\vec{q}(\boldsymbol{x}, t)). \tag{A.6}$$

This expression is precisely the definition of the divergence of a flux tensor $\vec{\boldsymbol{\mathcal{F}}}$ (represented as $\vec{\mathcal{F}}$ in the original text, let's use $\vec{\mathbb{F}}$ here to distinguish the tensor from the flux vectors $\vec{\mathcal{F}}_i$) whose columns are the flux vectors:

$$\vec{\boldsymbol{\mathcal{F}}}(\vec{q}(\boldsymbol{x}, t)) = \left[\vec{\mathcal{F}}_x(\vec{q}), \vec{\mathcal{F}}_y(\vec{q}), \vec{\mathcal{F}}_z(\vec{q})\right]. \tag{A.7}$$

Thus, the spatial term can be compactly written using the divergence operator:

$$\vec{\mathcal{K}}(\boldsymbol{x}, t) = \nabla \cdot \vec{\boldsymbol{\mathcal{F}}}(\vec{q}(\boldsymbol{x}, t)). \tag{A.8}$$

Substituting this divergence form of $\vec{\mathcal{K}}$ back into the system Equation (A.3) yields Maxwell's equations in the desired conservation form:

$$Q(\boldsymbol{x}) \cdot \frac{\partial \vec{q}(\boldsymbol{x}, t)}{\partial t} + \nabla \cdot \vec{\boldsymbol{\mathcal{F}}}(\vec{q}(\boldsymbol{x}, t)) = \vec{\mathcal{S}}(\boldsymbol{x}, t). \tag{A.9}$$

This form, $Q\partial_t \vec{q} + \nabla \cdot \vec{\boldsymbol{\mathcal{F}}}(\vec{q}) = \vec{\mathcal{S}}$, is the foundation for applying numerical methods designed for hyperbolic conservation laws, such as the FVM or the DGTD method.

A.2 Numerical Flux Derivation (1D Example)

Numerical methods like the DGTD method discretize the computational domain into elements. Across the interfaces between these elements, the numerical solution for the field vector $\vec{q}$ may be discontinuous. To ensure a unique and physically consistent transfer of information across these interfaces, a *numerical flux* function is required. This function approximates the physical flux based on the potentially different solution values on either side of the interface. Often, the numerical flux is derived by considering the solution to a local Riemann problem at the interface. This section details the derivation for a common upwind numerical flux for the simplified one-dimensional (1D) Maxwell's equations, assuming propagation along the x-axis and isotropic scalar material properties $\epsilon(x), \mu(x)$.

Consider the 1D Maxwell's equations written in the system form, simplified for 1D and assuming source-free conditions ($\vec{\mathcal{S}} = \vec{0}$) for clarity

$$Q(x)\frac{\partial \vec{q}(x, t)}{\partial t} + A\frac{\partial \vec{q}(x, t)}{\partial x} = \vec{0}, \tag{A.10}$$

where the material matrix $Q(x)$, the constant flux Jacobian matrix A, and the state vector $\vec{q}(x,t)$ are defined as

$$Q(x) = \begin{bmatrix} \epsilon(x) & 0 \\ 0 & \mu(x) \end{bmatrix}, \qquad A = \begin{bmatrix} 0 & 1 \\ 1 & 0 \end{bmatrix},$$
$$\vec{q}(x,t) = \begin{bmatrix} \mathcal{E}(x,t) \\ \mathcal{H}(x,t) \end{bmatrix}.$$

The physical flux vector associated with this system is $\vec{F}(\vec{q}) = A\vec{q} = [\mathcal{H}, \mathcal{E}]^T$. The characteristic wave propagation speeds of the system are given by the eigenvalues of the matrix $Q^{-1}A$. Calculating this product gives:

$$Q^{-1}A = \begin{bmatrix} 1/\epsilon(x) & 0 \\ 0 & 1/\mu(x) \end{bmatrix} \begin{bmatrix} 0 & 1 \\ 1 & 0 \end{bmatrix} = \begin{bmatrix} 0 & 1/\epsilon(x) \\ 1/\mu(x) & 0 \end{bmatrix}.$$

The eigenvalues λ satisfy the characteristic equation $\det(Q^{-1}A - \lambda I) = \lambda^2 - 1/(\epsilon(x)\mu(x)) = 0$. The solutions are $\lambda = \pm 1/\sqrt{\epsilon(x)\mu(x)} = \pm c(x)$, where $c(x)$ is the local speed of light. This confirms the existence of two characteristic waves propagating in opposite directions along the x-axis.

Now, consider an interface located at some position x_{int} between two computational elements. Let $\vec{q}^-$ and $\vec{q}^+$ denote the state vectors immediately to the left ($x = x_{int}^-$) and right ($x = x_{int}^+$) of this interface, representing the solution values from the adjacent elements. Within the context of methods like DGTD, the material properties are typically assumed to be constant within each element. Thus, ϵ^-, μ^- represent the constant permittivity and permeability in the element to the left of the interface, and ϵ^+, μ^+ represent the constant values in the element to the right. The numerical flux, denoted by $(\Pi\vec{q})^*$, represents the unique flux value used at the interface within the numerical scheme. It is determined by solving an approximate Riemann problem based on the states $\vec{q}^-$ and $\vec{q}^+$ and the material properties $\epsilon^\pm, \mu^\pm$. The Rankine-Hugoniot conditions, adapted for this system, relate the states across the characteristic waves emanating from the interface. These conditions involve an intermediate state $\vec{q}^*$ and the numerical flux $(\Pi\vec{q})^*$:

$$c^-Q^-(\vec{q}^* - \vec{q}^-) + (\Pi\vec{q})^* - (\Pi\vec{q})^- = \vec{0}, \tag{A.11}$$

$$c^+Q^+(\vec{q}^* - \vec{q}^+) + (\Pi\vec{q})^* - (\Pi\vec{q})^+ = \vec{0}. \tag{A.12}$$

In these equations, $Q^\pm$ are the material matrices evaluated using the constant values $\epsilon^\pm, \mu^\pm$ on the respective sides of the interface. The terms $c^\pm$ represent characteristic speeds associated with the waves propagating away from the interface into the left (-) and right (+) regions, calculated as $c^\pm = 1/\sqrt{\epsilon^\pm\mu^\pm}$. $(\Pi\vec{q})^\pm = A\vec{q}^\pm = [H^\pm, E^\pm]^T$ are the physical fluxes evaluated using the left and right states, and $(\Pi\vec{q})^* = [H^*, E^*]^T$ is the numerical flux vector sought.

Algebraic manipulation of Equations (A.11) and (A.12) to eliminate the intermediate state $\vec{q}^*$ yields an equation directly for the numerical flux $(\Pi\vec{q})^*$

$$\left(c^+Q^+ - c^-Q^-\right)(\Pi\vec{q})^* = c^+Q^+(\Pi\vec{q})^- - c^-Q^-(\Pi\vec{q})^+ + c^-c^+Q^-Q^+\left(\vec{q}^- - \vec{q}^+\right). \tag{A.13}$$

Expanding the matrices and vectors in this equation gives:

$$\left(c^+\begin{bmatrix}\epsilon^+ & 0\\ 0 & \mu^+\end{bmatrix} - c^-\begin{bmatrix}\epsilon^- & 0\\ 0 & \mu^-\end{bmatrix}\right)\begin{bmatrix}H^*\\ E^*\end{bmatrix} = c^+\begin{bmatrix}\epsilon^+ & 0\\ 0 & \mu^+\end{bmatrix}\begin{bmatrix}H^-\\ E^-\end{bmatrix} - c^-\begin{bmatrix}\epsilon^- & 0\\ 0 & \mu^-\end{bmatrix}\begin{bmatrix}H^+\\ E^+\end{bmatrix} + c^-c^+\begin{bmatrix}\epsilon^- & 0\\ 0 & \mu^-\end{bmatrix}\begin{bmatrix}\epsilon^+ & 0\\ 0 & \mu^+\end{bmatrix}\begin{bmatrix}E^- - E^+\\ H^- - H^+\end{bmatrix}. \tag{A.14}$$

To simplify this expression, the concepts of characteristic wave admittance $Y = \sqrt{\epsilon/\mu}$ and impedance $Z = \sqrt{\mu/\epsilon}$ are introduced. These are related to the material properties and wave speeds via $Y^\pm = c^\pm\epsilon^\pm$ and $Z^\pm = c^\pm\mu^\pm$, where $c^\pm = 1/\sqrt{\epsilon^\pm\mu^\pm}$ are the positive wave speeds. Interpreting the coefficients $c^\pm$ in Equation (A.13) such that the combination $(c^+Q^+ - c^-Q^-)$ appropriately reflects the wave interactions (potentially by defining c^- as the negative speed, $c^- = -1/\sqrt{\epsilon^-\mu^-}$), the equation can be rewritten in terms of admittance and impedance. This manipulation leads to the following form

$$\left(\begin{bmatrix}Y^+ & 0\\ 0 & Z^+\end{bmatrix} + \begin{bmatrix}Y^- & 0\\ 0 & Z^-\end{bmatrix}\right)\begin{bmatrix}H^*\\ E^*\end{bmatrix} = \begin{bmatrix}Y^+ & 0\\ 0 & Z^+\end{bmatrix}\begin{bmatrix}H^-\\ E^-\end{bmatrix} + \begin{bmatrix}Y^- & 0\\ 0 & Z^-\end{bmatrix}\begin{bmatrix}H^+\\ E^+\end{bmatrix} + \begin{bmatrix}Y^+Y^- & 0\\ 0 & Z^+Z^-\end{bmatrix}\begin{bmatrix}E^- - E^+\\ H^- - H^+\end{bmatrix}. \tag{A.15}$$

Introducing the jump operator $[\![u]\!] = u^- - u^+$, this system becomes

$$\begin{bmatrix}Y^+ + Y^- & 0\\ 0 & Z^+ + Z^-\end{bmatrix}\begin{bmatrix}H^*\\ E^*\end{bmatrix} = \begin{bmatrix}Y^+H^- + Y^-H^+\\ Z^+E^- + Z^-E^+\end{bmatrix} + \begin{bmatrix}Y^+Y^-[\![E]\!]\\ Z^+Z^-[\![H]\!]\end{bmatrix}. \tag{A.16}$$

This matrix equation elegantly decouples into two independent scalar equations for the components H^* and E^* of the numerical flux vector $(\Pi\vec{q})^*$

$$(Y^+ + Y^-)H^* = Y^+H^- + Y^-H^+ + Y^+Y^-[\![E]\!], \tag{A.17}$$

$$(Z^+ + Z^-)E^* = Z^+E^- + Z^-E^+ + Z^+Z^-[\![H]\!]. \tag{A.18}$$

These equations can be solved explicitly for H^* and E^*:

$$H^* = \frac{Y^+H^- + Y^-H^+ + Y^+Y^-[\![E]\!]}{Y^+ + Y^-}, \tag{A.19}$$

$$E^* = \frac{Z^+E^- + Z^-E^+ + Z^+Z^-[\![H]\!]}{Z^+ + Z^-}. \tag{A.20}$$

Further manipulation using the average operator defined as $\{\{u\}\} = (u^- + u^+)/2$ allows these expressions to be rewritten. For instance, defining $\{\{XY\}\} = (X^-Y^- + X^+Y^+)/2$, the numerical flux components can be expressed as

$$H^* = \frac{1}{2\{\{Z\}\}}\left(\{\{ZH\}\} + \frac{1}{2}[\![E]\!]\right), \tag{A.21}$$

$$E^* = \frac{1}{2\{\{Y\}\}} \left(\{\{YE\}\} + \frac{1}{2}[\![H]\!] \right). \tag{A.22}$$

These equations, in either the form of Equations (A.19) and (A.20) or Equations (A.21) and (A.22), define the components of the upwind numerical flux vector $(\Pi \vec{q})^* = [H^*, E^*]^T$. This flux is used at element interfaces in the DGTD or FVM discretization to ensure stability and accurately capture wave propagation across potentially discontinuous material properties or solutions.

APPENDIX B

Analytical Solutions

B.1 Eletromagnetic Scattering

This section presents the modal solutions for the canonical electromagnetic scattering problems in free-space involving a plane wave with TM or Transverse Electric (TE) polarization interacting with a PEC or dielectric cylinder and the electromagnetic scattering of a plane wave by a PEC or dielectric sphere.

The main objective here is to summary the equations of the incident, internal and scattered electromagnetic fields obtained from [50, 33].

B.1.1 Scattering of a Plane Wave by a Conducting Cylinder

Considering that a plane wave perpendicular to a cylinder can be broken down into a combination of a TM polarized wave, characterized by just a z component for its electric field, and a TE-polarized wave, characterized by only a z component for its magnetic field, it is sufficient to examine these two incident plane waves.

Considering that the electric field of a TM polarized incident plane wave,

$$\boldsymbol{E}^{inc}(x,y,z,\omega) = \hat{\boldsymbol{z}} E_z^{inc} = \hat{\boldsymbol{z}} E_0 e^{-jkx}, \tag{B.1}$$

can be rewritten in cylindrical components as

$$E_z^{inc}(\rho,\phi,z,\omega) = E_0 \sum_{n=-\infty}^{\infty} j^{-n} J_n(k_0\rho) e^{jn\phi}, \tag{B.2}$$

where E_0 is a constant, J_n is the nth order Bessel function and the propagation constant is $k_0 = \omega\sqrt{\epsilon_0\mu_0}$.

It can be shown that the scattered electric field by a PEC cylinder with radius a is given by

$$E_z^{scat}(\rho,\phi,z,\omega) = E_0 \sum_{n=-\infty}^{\infty} a_n H_n^{(2)}(k_0\rho)e^{jn\phi}, \tag{B.3}$$

where $H_n^{(2)}$ is the nth order Hankel function of the second kind and a_n is

$$a_n = -j^{-n}\frac{J_n(k_0a)}{H_n^{(2)}(k_0a)}. \tag{B.4}$$

The same analysis can be made to the TE polarization leading to magnetic fields like

$$H_z^{inc}(\rho,\phi,z,\omega) = H_0 \sum_{n=-\infty}^{\infty} j^{-n} J_n(k_0\rho)e^{jn\phi}, \tag{B.5}$$

$$H_z^{scat}(\rho,\phi,z,\omega) = H_0 \sum_{n=-\infty}^{\infty} b_n H_n^{(2)}(k_0\rho)e^{jn\phi}, \tag{B.6}$$

with b_n being

$$b_n = -j^{-n}\frac{J_n'(k_0a)}{H_n^{(2)\prime}(k_0a)}, \tag{B.7}$$

noting that ${J_n}'(z) = dJ_n(z)/dz$ and ${H_n}^{(2)\prime}(z) = dH_n^{(2)}(z)/dz$.

Figure 33 shows the total field solution ($E_z^{total} = E_z^{scat} + E_z^{inc}$) for a TM and TE polarized plane wave propagating in the $\hat{\boldsymbol{x}}$ direction and interacting with a PEC cylinder of radius $1\lambda_0$, where λ_0 represents the free-space wavelength, defined as $\lambda_0 = 2\pi/k_0$. Only the first 100 modes were considered ($n = 100$). The results obtained align with the existing literature [50].

B.1.2 Scattering of a Plane wave by a Dielectric Cylinder

The approach used to solve the problem of a plane wave scattered by a dielectric cylinder is comparable to the one discussed previously for the conducting cylinder. The scattered field can be expanded as demonstrated in the previous section, and the internal field, taking into account TM polarization and a cylinder with permittivity ϵ_d and permeability μ_d, can also be expanded as

$$E_z^{int}(\rho,\phi,z,\omega) = E_0 \sum_{n=-\infty}^{\infty} c_n J_n(k_d\rho)e^{jn\phi} \tag{B.8}$$

where $k_d = \omega\sqrt{\epsilon_d\mu_d}$ and the coefficients are

$$a_n = -j^{-n}\frac{\sqrt{\mu_r}J_n'(k_0a)J_n(k_da) - \sqrt{\epsilon_r}J_n(k_0a)J_n'(k_da)}{\sqrt{\mu_r}H_n^{(2)\prime}(k_0a)J_n(k_da) - \sqrt{\epsilon_r}H_n^{(2)}(k_0a)J_n'(k_da)}, \tag{B.9}$$

$$c_n = \frac{j^{-(n+1)}}{\pi k_0 a}\frac{2\sqrt{\mu_r}}{\sqrt{\mu_r}H_n^{(2)\prime}(k_0a)J_n(k_da) - \sqrt{\epsilon_r}H_n^{(2)}(k_0a)J_n'(k_da)}, \tag{B.10}$$

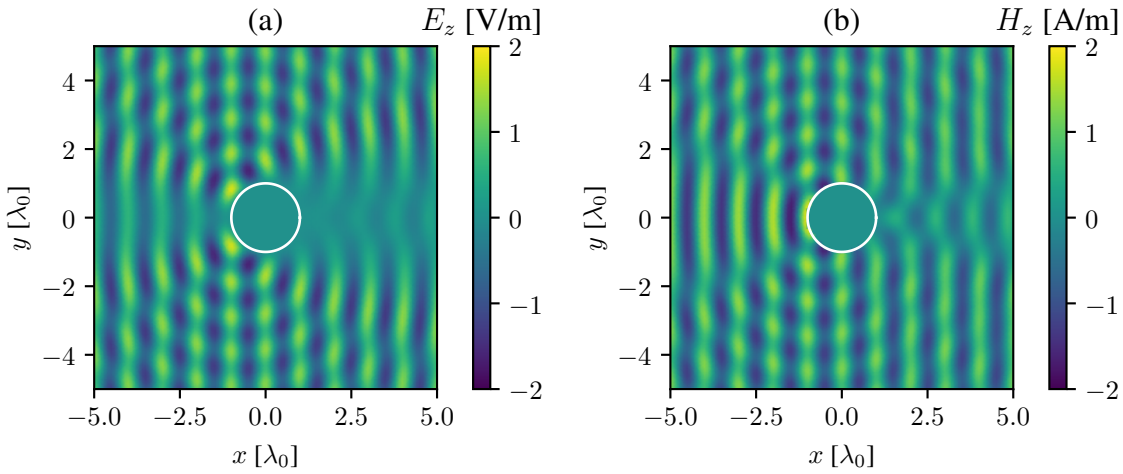

Figure 33 – Scattering of a plane wave by a conducting cylinder.
The analytical solution of the corresponding total electromagnetic fields are illustrated for the (a) TMz polarization and (b) TEz polarization on the $z = 0$ plane.

where $\epsilon_r = \epsilon_d/\epsilon_0$ and $\mu_r = \mu_d/\mu_0$.

For the TE polarization case, the magnetic field inside the cylinder can be expanded as

$$H_z^{int}(\rho, \phi, z, \omega) = H_0 \sum_{n=-\infty}^{\infty} d_n J_n(k_d \rho) e^{jn\phi} \tag{B.11}$$

leading to

$$b_n = -j^{-n} \frac{\sqrt{\epsilon_r} J_n'(ka) J_n(k_d a) - \sqrt{\mu_r} J_n(ka) J_n'(k_d a)}{\sqrt{\epsilon_r} H_n^{(2)\prime}(ka) J_n(k_d a) - \sqrt{\mu_r} H_n^{(2)}(ka) J_n'(k_d a)}, \tag{B.12}$$

$$d_n = \frac{j^{-(n+1)}}{\pi ka} \frac{2\sqrt{\epsilon_r}}{\sqrt{\epsilon_r} H_n^{(2)\prime}(ka) J_n(k_d a) - \sqrt{\mu_r} H_n^{(2)}(ka) J_n'(k_d a)}. \tag{B.13}$$

Figure 34 shows the total field solution for a TM and TE polarized plane wave propagating in the $\hat{\boldsymbol{x}}$ direction and interacting with a PEC cylinder of radius $1\lambda_0$ and relative permittivity $\epsilon_r = 4$. Only the first 100 modes were considered ($n = 100$). The results obtained align with the existing literature [50].

B.1.3 Scattering of a Plane Wave by a Conducing Sphere

Considering that the eletric field of an x-polarized incident plane wave,

$$\boldsymbol{E}^{inc} = \hat{\boldsymbol{x}} E_0 e^{-jk_0 z} = \hat{\boldsymbol{x}} E_0 e^{-jk_0 r \cos\theta}, \tag{B.14}$$

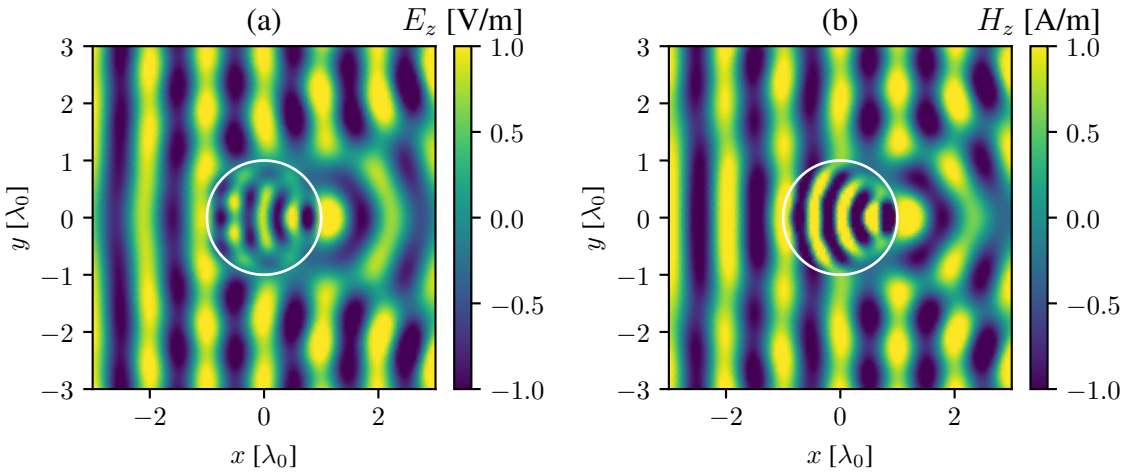

Figure 34 – Scattering of a plane wave by a dielectric cylinder.
The analytical solution of the corresponding total electromagnetic fields are illustrated for a (a) TMz polarization and (b) TEz polarization for a dielectric cylinder on the $z = 0$ plane.

can be rewritten in spherical components in terms of Riccati-Bessel functions ($\hat{J}_n(z) = zJ_n(z)$ and $\hat{H}_n^{(2)}(z) = zH_n^{(2)}(z)$) as

$$E_r^{inc} = E_0 \frac{\cos\phi}{j(k_0 r)^2} \sum_{n=0}^{\infty} j^{-n}(2n+1)\hat{J}_n(k_0 r)P_n^1(\cos\theta), \tag{B.15}$$

$$E_\theta^{inc} = E_0 \frac{\cos\theta\cos\phi}{k_0 r} \sum_{n=0}^{\infty} j^{-n}(2n+1)\hat{J}_n(k_0 r)P_n(\cos\theta), \tag{B.16}$$

$$E_\phi^{inc} = -E_0 \frac{\sin\phi}{k_0 r} \sum_{n=0}^{\infty} j^{-n}(2n+1)\hat{J}_n(k_0 r)P_n(\cos\theta), \tag{B.17}$$

where P_n^i is the nth order Legendre polynomial of degree i and $dP_n(\cos\theta)/d\theta = P_n^1(\cos\theta)$. The corresponding magnetic field components are

$$H_r^{inc} = H_0 \frac{\sin\phi}{j(k_0 r)^2} \sum_{n=0}^{\infty} j^{-n}(2n+1)\hat{J}_n(k_0 r)P_n^1(\cos\theta), \tag{B.18}$$

$$H_\theta^{inc} = H_0 \frac{\cos\theta\sin\phi}{k_0 r} \sum_{n=0}^{\infty} j^{-n}(2n+1)\hat{J}_n(k_0 r)P_n(\cos\theta), \tag{B.19}$$

$$H_\phi^{inc} = H_0 \frac{\cos\phi}{k_0 r} \sum_{n=0}^{\infty} j^{-n}(2n+1)\hat{J}_n(k_0 r)P_n(\cos\theta), \tag{B.20}$$

where $H_0 = E_0/\eta_0$ and $\eta_0 = \sqrt{\mu_0/\epsilon_0}$.

Considering a sphere with radius a, it can be shown that the fields inside the sphere are

zero and the spherical components of the scattered electric and magnetic fields are

$$E_r^{scat} = E_0 \frac{\cos\phi}{j(k_0 r)^2} \sum_{n=0}^{\infty} a_n n(n+1) \hat{H}_n^{(2)}(k_0 r) P_n^1(\cos\theta), \tag{B.21}$$

$$E_\theta^{scat} = -\frac{E_0 \cos\phi}{k_0 r} \sum_{n=1}^{\infty} \left[a_n j \hat{H}_n^{(2)\prime}(k_0 r) \frac{dP_n^1(\cos\theta)}{d\theta} + b_n \hat{H}_n^{(2)}(k_0 r) \frac{P_n^1(\cos\theta)}{\sin\theta} \right], \tag{B.22}$$

$$E_\phi^{scat} = \frac{E_0 \sin\phi}{k_0 r} \sum_{n=1} \left[a_n j \hat{H}_n^{(2)\prime}(k_0 r) \frac{P_n^1(\cos\theta)}{\sin\theta} + b_n \hat{H}_n^{(2)}(k_0 r) \frac{dP_n^1(\cos\theta)}{d\theta} \right], \tag{B.23}$$

$$H_r^{scat} = H_0 \frac{\sin\phi}{j(k_0 r)^2} \sum_{n=0}^{\infty} b_n n(n+1) \hat{H}_n^{(2)}(k_0 r) P_n^1(\cos\theta), \tag{B.24}$$

$$H_\theta^{scat} = -\frac{H_0 \sin\phi}{k_0 r} \sum_{n=1}^{\infty} \left[a_n \hat{H}_n^{(2)}(k_0 r) \frac{P_n^1(\cos\theta)}{\sin\theta} + b_n j \hat{H}_n^{(2)\prime}(k_0 r) \frac{dP_n^1(\cos\theta)}{d\theta} \right], \tag{B.25}$$

$$H_\phi^{scat} = -\frac{H_0 \cos\phi}{k_0 r} \sum_{n=1} \left[a_n \hat{H}_n^{(2)}(k_0 r) \frac{dP_n^1(\cos\theta)}{d\theta} + b_n j \hat{H}_n^{(2)\prime}(k_0 r) \frac{P_n^1(\cos\theta)}{\sin\theta} \right], \tag{B.26}$$

where

$$a_n = -j^{-n} \frac{2n+1}{n(n+1)} \frac{\hat{J}_n'(k_0 a)}{\hat{H}_n^{(2)\prime}(k_0 a)} \tag{B.27}$$

$$b_n = -j^{-n} \frac{2n+1}{n(n+1)} \frac{\hat{J}_n(k_0 a)}{\hat{H}_n^{(2)}(k_0 a)} \tag{B.28}$$

Figure 35 shows the normalized y component of the total magnetic field solution for a $\hat{\boldsymbol{x}}$ polarized plane wave propagating in the $\hat{\boldsymbol{z}}$ direction and interacting with a PEC sphere of radius $1\lambda_0$. Only the first 50 modes were considered ($n = 50$). The results obtained align with the existing literature [50].

B.1.4 Scattering of a Plane Wave by a Dielectric Sphere

The solution for solving the problem of plane-wave scattering by a dielectric sphere is similar to the approach that was previously discussed for the conducting sphere. The scattered fields are the same. Assuming that the dielectric sphere has a permittivy of ϵ_d and a permeability of μ_d. The fields inside the sphere can be expanded in terms of the TEr and TMr waves leading to the following equations

$$E_r^{int} = E_0 \frac{\cos\phi}{j(k_d r)^2} \sum_{n=0}^{\infty} c_n n(n+1) \hat{J}_n(k_d r) P_n^1(\cos\theta), \tag{B.29}$$

$$E_\theta^{int} = -\frac{E_0 \cos\phi}{k_d r} \sum_{n=1}^{\infty} \left[c_n j \hat{J}_n'(k_d r) \frac{dP_n^1(\cos\theta)}{d\theta} + d_n \hat{J}_n(k_d r) \frac{P_n^1(\cos\theta)}{\sin\theta} \right], \tag{B.30}$$

$$E_\phi^{int} = \frac{E_0 \sin\phi}{k_d r} \sum_{n=1}^{\infty} \left[c_n j \hat{J}_n'(k_d r) \frac{P_n^1(\cos\theta)}{\sin\theta} + d_n \hat{J}_n(k_d r) \frac{dP_n^1(\cos\theta)}{d\theta} \right], \tag{B.31}$$

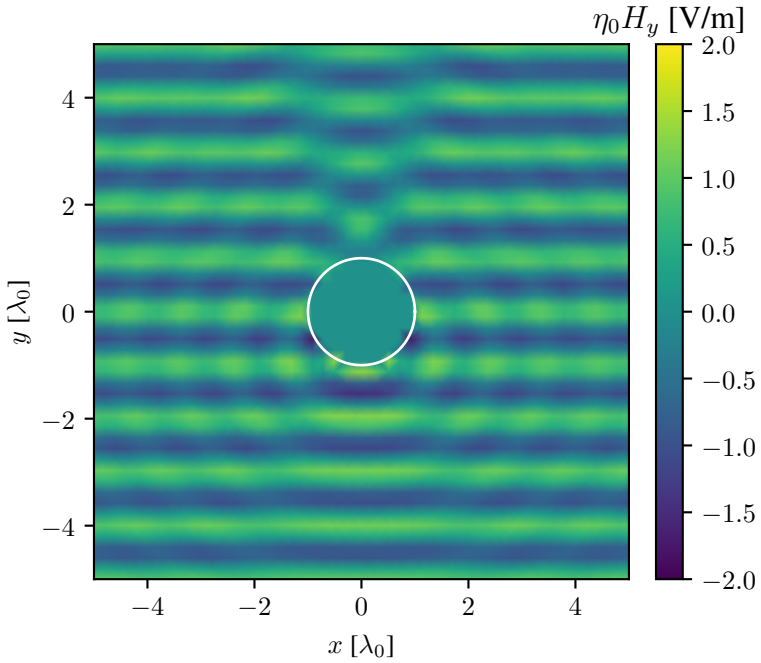

Figure 35 – Scattering of a plane wave by a conducting sphere.
The analytical solution of the normalized y component of the total magnetic field is illustrated for a PEC sphere on the $y = 0$ plane.

$$H_r^{int} = E_0 \frac{\sin\phi}{j\eta_d (k_d r)^2} \sum_{n=0}^{\infty} d_n n(n+1) \hat{J}_n(k_d r) P_n^1(\cos\theta), \tag{B.32}$$

$$H_\theta^{int} = -\frac{E_0 \sin\phi}{\eta_d k_d r} \sum_{n=1}^{\infty} \left[c_n \hat{J}_n(k_d r) \frac{P_n^1(\cos\theta)}{\sin\theta} + d_n j \hat{J}_n'(k_d r) \frac{dP_n^1(\cos\theta)}{d\theta} \right], \tag{B.33}$$

$$H_\phi^{int} = \frac{E_0 \cos\phi}{\eta_d k_d r} \sum_{n=1}^{\infty} \left[c_n \hat{J}_n(k_d r) \frac{dP_n^1(\cos\theta)}{d\theta} + d_n j \hat{J}_n'(k_d r) \frac{P_n^1(\cos\theta)}{\sin\theta} \right]. \tag{B.34}$$

The coefficients for both scattered and internal eletromagnetic fields are

$$a_n = j^{-n} \frac{2n+1}{n(n+1)} \frac{\sqrt{\epsilon_r} \hat{J}_n'(k_0 a) \hat{J}_n(k_d a) - \sqrt{\mu_r} \hat{J}_n(k_0 a) \hat{J}_n'(k_d a)}{\sqrt{\mu_r} \hat{H}_n^{(2)}(k_0 a) \hat{J}_n'(k_d a) - \sqrt{\epsilon_r} \hat{H}_n^{(2)\prime}(k_0 a) \hat{J}_n(k_d a)}, \tag{B.35}$$

$$b_n = j^{-n} \frac{2n+1}{n(n+1)} \frac{\sqrt{\mu} \hat{J}_n'(k_0 a) \hat{J}_n(k_d a) - \sqrt{\epsilon_r} \hat{J}_n(k_0 a) \hat{J}_n'(k_d a)}{\sqrt{\epsilon_r} \hat{H}_n^{(2)}(k_0 a) \hat{J}_n'(k_d a) - \sqrt{\epsilon_r} \hat{H}_n^{(2)\prime}(k_0 a) \hat{J}_n(k_d a)}, \tag{B.36}$$

$$c_n = j^{-n} \frac{2n+1}{n(n+1)} \frac{j\sqrt{\epsilon_r}\mu_r}{\sqrt{\mu_r} \hat{H}_n^{(2)}(k_0 a) \hat{J}_n'(k_d a) - \sqrt{\epsilon_r} \hat{H}_n^{(2)\prime}(k_0 a) \hat{J}_n(k_d a)}, \tag{B.37}$$

$$d_n = j^{-n} \frac{2n+1}{n(n+1)} \frac{j\sqrt{\epsilon_r}\mu_r}{\sqrt{\epsilon_r} \hat{H}_n^{(2)}(k_0 a) \hat{J}_n'(k_d a) - \sqrt{\epsilon_r} \hat{H}_n^{(2)\prime}(k_0 a) \hat{J}_n(k_d a)}. \tag{B.38}$$

Figure 36 shows the normalized y component of the total magnetic field solution for a $\hat{\boldsymbol{x}}$ polarized plane wave propagating in the $\hat{\boldsymbol{z}}$ direction and interacting with a dielectric sphere of radius $1\lambda_0$ and relative permittivity $\epsilon_r = 2.56$. Only the first 50 modes were considered ($n = 50$). The results obtained align with the existing literature [50].

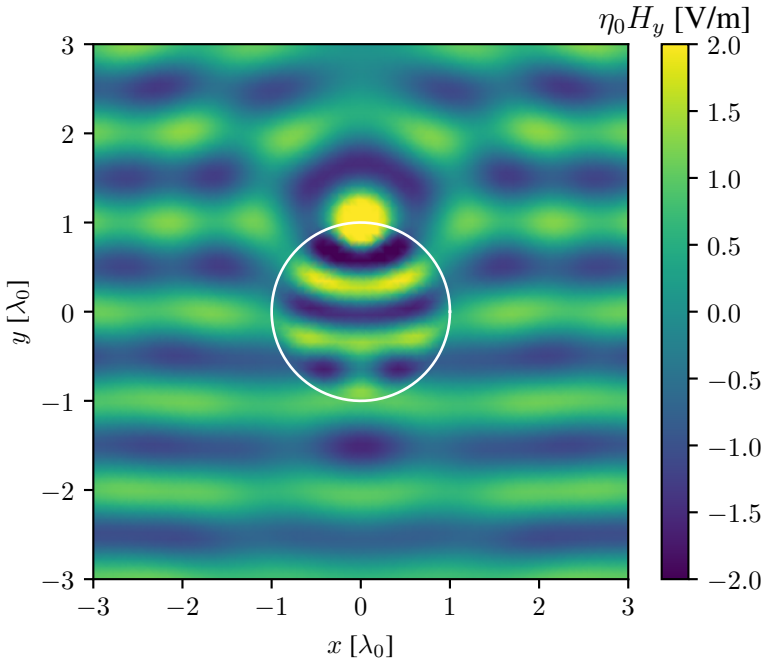

Figure 36 – Scattering of a plane wave by a dielectric sphere.
The analytical solution of the normalized y component of the total magnetic field is illustrated for a dielectric sphere on the $y = 0$ plane.

$$b_n = -j^{-n} \frac{\sqrt{\epsilon_r}\hat{J}_n'(ka)\hat{J}_n(k_d a) - \sqrt{\mu_r}\hat{J}_n(ka)\hat{J}_n'(k_d a)}{\sqrt{\epsilon_r}\hat{H}_n^{(2)\prime}(ka)\hat{J}_n(k_d a) - \sqrt{\mu_r}\hat{H}_n^{(2)}(ka)\hat{J}_n'(k_d a)}, \tag{B.39}$$

$$d_n = \frac{j^{-(n+1)}}{\pi ka} \frac{2\sqrt{\epsilon_r}}{\sqrt{\epsilon_r}\hat{H}_n^{(2)\prime}(ka)\hat{J}_n(k_d a) - \sqrt{\mu_r}\hat{H}_n^{(2)}(ka)\hat{J}_n'(k_d a)}. \tag{B.40}$$

$$b_n = -j^{-n} \frac{\hat{J}_n'(k_0 a)\hat{J}_n(k_d a) - \sqrt{\mu_r/\epsilon_r}\hat{J}_n(k_0 a)\hat{J}_n'(k_d a)}{\hat{H}_n^{(2)\prime}(k_0 a)\hat{J}_n(k_d a) - \sqrt{\mu_r/\epsilon_r}\hat{H}_n^{(2)}(k_0 a)\hat{J}_n'(k_d a)}, \tag{B.41}$$

$$d_n = \frac{j^{-(n+1)} 2/(\pi k_0 a)}{\hat{H}_n^{(2)\prime}(k_0 a)\hat{J}_n(k_d a) - \sqrt{\mu_r/\epsilon_r}\hat{H}_n^{(2)}(k_0 a)\hat{J}_n'(k_d a)}. \tag{B.42}$$

APPENDIX C

IMEX Runge-Kutta Coefficients

This appendix details the coefficients for the fourth-order Runge-Kutta schemes employed in the IMEX integration utilized in this work. The methodology utilizes a coupled approach, leveraging both an explicit and an implicit method. The explicit scheme provides efficient computation for portions of the system where stiffness is not a dominant concern, while the implicit scheme addresses stiffness-related stability issues where they arise. This combined approach allows balancing computational efficiency and numerical stability.

The explicit component is a six-stage, fourth-order Explicit RK method. Six stages are used to achieve fourth-order accuracy, offering a balance between accuracy and computational cost. The implicit component is a six-stage, fourth-order Explicit Singly Diagonally Implicit Runge-Kutta (ESDIRK) method. The "singly diagonally implicit" nature of this scheme simplifies the implicit solve compared to fully implicit methods, as it only requires the solution of a series of scalar equations rather than a full matrix inversion at each stage. The shared number of stages between the explicit and implicit schemes simplifies implementation and can facilitate switching between the two methods. Both schemes share the same abscissa (time points within a step) and weights, simplifying the coupling process crucial for IMEX methods.

The Butcher tableaux, a compact representation of the coefficients defining these RK schemes, are provided below. These tableaux define the stage values k_i and the final update for each time step. The values presented here are taken from [21].

Table 10 – Butcher Tableau for the Explicit RK46 Scheme (ERK part of the IMEX pair)

c_i	a_{i1}	a_{i2}	a_{i3}	a_{i4}	a_{i5}	a_{i6}
0	0	0	0	0	0	0
$\frac{1}{2}$	$\frac{1}{2}$	0	0	0	0	0
$\frac{83}{250}$	$\frac{13861}{62500}$	$\frac{6889}{62500}$	0	0	0	0
$\frac{31}{50}$	$-\frac{116923316275}{2393684061468}$	$-\frac{2731218467317}{15368042101831}$	$\frac{9408046702089}{11113171139209}$	0	0	0
$\frac{17}{20}$	$-\frac{451086348788}{2902428689909}$	$-\frac{2682348792572}{7519795681897}$	$\frac{12662868775082}{11960479115383}$	$\frac{3355817975965}{11060851509271}$	0	0
1	$\frac{647845179188}{3216320057751}$	$\frac{73281519250}{8382639484533}$	$\frac{552539513391}{34546683868233}$	$\frac{3354512671639}{8306763924573}$	$\frac{4040}{17871}$	0
	$\frac{82889}{524892}$	0	$\frac{15625}{83664}$	$\frac{69875}{102672}$	$-\frac{2260}{8211}$	$\frac{1}{4}$
	b_1	b_2	b_3	b_4	b_5	b_6

Table 11 – Butcher tableau for the implicit ESDIRK46 Scheme (Implicit part of the IMEX pair)

c_i	a_{i1}	a_{i2}	a_{i3}	a_{i4}	a_{i5}	a_{i6}
0	0	0	0	0	0	0
$\frac{1}{2}$	$\frac{1}{4}$	$\frac{1}{4}$	0	0	0	0
$\frac{83}{250}$	$\frac{8611}{62500}$	$-\frac{1743}{31250}$	$\frac{1}{4}$	0	0	0
$\frac{31}{50}$	$\frac{5012029}{34652500}$	$-\frac{654441}{2922500}$	$\frac{174375}{388108}$	$\frac{1}{4}$	0	0
$\frac{17}{20}$	$\frac{15267082809}{155376265600}$	$-\frac{71443401}{120774400}$	$\frac{730878875}{902184768}$	$\frac{2285395}{8070912}$	$\frac{1}{4}$	0
1	$\frac{82889}{524892}$	0	$\frac{15625}{83664}$	$\frac{69875}{102672}$	$-\frac{2260}{8211}$	$\frac{1}{4}$
	$\frac{82889}{524892}$	0	$\frac{15625}{83664}$	$\frac{69875}{102672}$	$-\frac{2260}{8211}$	$\frac{1}{4}$
	b_1	b_2	b_3	b_4	b_5	b_6